

© 2022

REED A. DAVIS

ALL RIGHTS RESERVED

INVESTIGATING THE EFFECTS OF AGING AND PROLONGED OPIOID USE ON
BONE HISTOMORPHOMETRY, QUALITY, AND BIOMECHANICS

A Dissertation

Presented to

The Graduate Faculty of The University of Akron

In Partial Fulfillment

of the Requirements for the Degree

Doctor of Philosophy

REED A. DAVIS

August, 2022

INVESTIGATING THE EFFECTS OF AGING AND PROLONGED OPIOID USE ON
BONE HISTOMORPHOMETRY, QUALITY, AND BIOMECHANICS

Reed A. Davis

Dissertation

Approved:

Accepted:

Advisor
Dr. Brian Bagatto

Program Director, Integrated Bioscience
Dr. Hazel Barton

Co-Advisor
Dr. Janna M. Andronowski

Dean of the College
Dr. Mitchell S. McKinney

Committee Member
Dr. Henry Astley

Interim Director, Graduate School
Dr. Marnie Saunders

Committee Member
Dr. David M.L. Cooper

Date

Committee Member
Dr. Christine Dengler-Crish

Committee Member
Dr. Nita Sahai

ABSTRACT

Opioids have become one of the most misused classes of prescribed medication. Synthetic opioids (e.g., fentanyl) have been responsible for most opioid overdose deaths since 2017. As this epidemic shows no signs of slowing, it is imperative to study the effects of opioids on various aspects of health including bone maintenance. Endogenous opioids (e.g., met-enkephalin) are involved in osteogenesis and bone remodeling. Exogenous opioids can interfere with bone maintenance directly through binding to osteoblasts, limiting bone formation, or indirectly through a cascade of effects limiting sex hormone production. To understand how opioids affect bone microarchitectural and biomechanical properties we first examine bone microstructure throughout the human lifespan to see natural changes occurring without the effects of opioids. Using both Synchrotron Radiation micro-Computed Tomography and confocal laser microscopy, we found bone and lacunar volume fractions to decrease with advancing age while pore diameter increased in the anterior midshaft femur. After finding how bone changes with age under normal circumstances, we sought to examine how prolonged opioid administration affected trabecular microstructure in a model organism (rabbit). We used μ CT to examine the proximal tibia by anatomical quadrant (e.g., anterior, posterior). We found that morphine animals had greater bone volume fraction and less trabecular separation than controls. Fentanyl animals had significantly thicker trabeculae and

increased trabecular spacing than controls. Detected differences by anatomical region followed the same overall pattern, suggesting biomechanical or anatomical variation rather than due to opioids. We finally examined overall bone strength in a non-weight bearing bone (rib) of the rabbit using uniaxial compression testing to determine how opioids affect overall mechanical competency. We found no difference in mechanical variables between opioid and control groups. Only rib span length was significantly greater in fentanyl animals compared to controls. Our stress-strain curves appeared remarkably similar to that of the standard curve derived from rocks. These results suggest that there is a complex response in bone to prolonged opioid administration and further work is necessary to elucidate such responses.

DEDICATION

I would like to thank my fellow graduate students and friends: Randi Depp, Evin Hessel, Kayla Calapa, Colleen Unsworth, Katie Duval, and Brady Knapik-Brown as well as Drs. Carrie Buo, Derek Jurestovsky, Jen Piechowski, Jessica Tingle, and Rachel Olson for their time spent troubleshooting and venting over meals or coffee. Hopefully, it was as helpful for you as it was for me.

I also wish to thank my parents Jean and Brad Davis and aunt and uncle Dr. Katherine Schultz and Bruce Moore for helping keep my head on straight; my friends Ryan and Bridget Anderson, Charbel and Emily Cherfan, and Elizabeth and Jason Chismar for reminding me to take a break occasionally to socialize and get some sun. Finally, to Alan Ellis for reminding me why I wanted to do all this in the first place. I would not have been able to complete this without the unyielding patience, support, and love from all of you.

ACKNOWLEDGEMENTS

Research detailed in this dissertation was completed with the collaborative effort of many people. I therefore wish to thank my advisory committee, Drs. Janna Andronowski, Brian Bagatto, Henry Astley, David Cooper, Christine Dengler-Crish, and Nita Sahai, for their tireless efforts in helping me achieve my endeavors.

I further wish to thank Dr. Mary E. Cole, Gina Tubo, Hope Zimmerman and Joshua Taylor for their assistance with methodology development, statistical analysis, and figure preparation throughout as part of larger projects. Thanks to Beth Dalzell (University of Toledo), Dr. Jeffrey Wenstrup (Northeast Ohio Medical University, NEOMED), the staff at the New York City Office of Chief Medical Examiner, and the selfless anatomical donors for access to cadaveric samples utilized in Chapter II.

Finally, I would like to thank the beamline scientists at Canadian Light Source for assistance with equipment setup and troubleshooting during SR μ CT imaging, Nancy Concepcion and Dr. Andrew Knoll (University of Akron, UA) for assistance with equipment setup and troubleshooting of the test frame and μ CT systems, Dr. Matthew Smith (NEOMED) for access to, and troubleshooting of, the confocal microscope, and Dr. Mike Marsh (Object Research Systems Inc.) for assistance in troubleshooting image analysis within Dragonfly. I further wish to thank Beth Kenaga (UA) for assistance with animal care. Work described here was funded, in part, by a National Institute of Justice grant awarded to Dr. Janna Andronowski (#2018-DU-BX-0188).

TABLE OF CONTENTS

	Page
LIST OF TABLES	xi
LIST OF FIGURES	xiii
LIST OF ABBREVIATIONS.....	xv
CHAPTER	
I. INTRODUCTION.....	1
Basic Bone Biology	2
Remodeling Theories	8
Bone Cell Signaling Axes.....	11
United States' Opioid Epidemic	14
Effects of Opioid Exposure on Bone	15
Organization of Dissertation.....	17
II. FEMORAL OSTEOCYTE LACUNO-CANALICULAR NETWORK AND VASCULAR PORE CHANGES ACROSS THE HUMAN LIFESPAN EXAMINED VIA SR μ CT AND CLSM	19
Introduction.....	19
Materials & Methods	21
SR μ CT Preparation and Imaging.....	22
SR μ CT Image Processing	23

CLSM Preparation and Imaging	25
CLSM Image Processing	26
Statistical Analysis.....	30
Results.....	31
SR μ CT	31
CLSM.....	41
Discussion.....	50
Vascular Pore Changes: SR μ CT.....	50
Age-Associated Lacunar Changes: SR μ CT and CLSM	51
Sex-Associated Lacunar Changes: SR μ CT and CLSM.....	51
Canalicular Changes: CLSM	52
Limitations and Future Directions	53
III. OPIOID-INDUCED TRABECULAR BONE CHANGES OF THE PROXIMAL TIBIA IN RABBITS VISUALIZED USING μCT	56
Introduction.....	56
Materials & Methods	59
Animals and Opioid Treatments	59
<i>Ex vivo</i> μ CT Imaging and Analysis	62
Statistical Analysis.....	66
Results.....	67
Rabbit Weight	67
Morphine & Saline.....	67
Fentanyl & Sham Patch	73

Discussion.....	78
Opioid Variation	78
Regional Variation.....	80
Limitations and Future Directions	82
IV. BIOMECHANICAL PROPERTIES OF RABBIT MIDDLE RIBS FOLLOWING PROLONGED OPIOID EXPOSURE	85
Introduction.....	85
Bone Material Properties	85
Opioid Effects on Bone Biomechanical Properties	87
Materials & Methods	89
Gross Geometry & Compression Testing.....	90
Data Analysis	93
Statistical Analysis.....	96
Results.....	97
Discussion.....	101
V. CONCLUSIONS.....	109
REFERENCES	113
APPENDICES	134
APPENDIX A. IMAGEJ MACRO FOR SR μ CT PORE EXTRACTION	135
APPENDIX B. IMAGEJ/CTANALYSER MACRO FOR CLSM LCN EXTRACTION	139
APPENDIX C. STEP-DOWN BONFERRONI CORRECTIONS	140
APPENDIX D. TRABECULAR ISOLATION TASKLIST IN CTANALYSER	142

APPENDIX E. IMAGEJ MACRO FOR MEDULLARY CAVITY QUADRANTS	145
APPENDIX F. MATLAB CODE FOR ANALYZING STRESS-STRAIN CURVE	147

LIST OF TABLES

Table		Page
1.	SR μ CT system experimental settings on BMIT-BM.	23
2.	Description of morphometric variables.	28
3.	Regression results for SR μ CT variables compared by chronological age and sex	33
4.	Factorial ANOVA results for SR μ CT variables compared by age group and sex.	34
5.	Tukey HSD post-hoc results for age group-significant SR μ CT variables.	35
6.	Regression results for CLSM variables compared by chronological age and sex.	42
7.	Factorial ANOVA results for CLSM variables compared by age group and sex.	43
8.	μ CT system settings applied to each scan.	63
9.	Description of morphometric variables.	65
10.	Two-Way ANOVA results for histomorphometric variables by drug group (morphine or saline) and anatomical region.	69
11.	Tukey HSD post-hoc results for region-significant μ CT variables in morphine and saline animals.	71
12.	Two-Way ANOVA results for histomorphometric variables by drug group (fentanyl or sham patch) and anatomical region.	73
13.	Tukey HSD post-hoc results for region-significant μ CT variables in fentanyl and sham patch animals.....	76
14.	Geometric properties gathered from bone area and rib measurements.	92
15.	Structural properties gathered from the stress-strain curve.	92

16.	One-Way ANOVA results for drug group (morphine vs. saline).	99
17.	One-Way ANOVA results for drug group (fentanyl vs. sham patch).	99

LIST OF FIGURES

Figure	Page
1. A schematic drawing of modelling drift.	3
2. A schematic drawing of a Basic Multicellular Unit (BMU).	5
3. RANK/OPG signaling axis.	12
4. Drug overdose deaths in the United States from 1999-2020.	15
5. Key output images from the femur of a 71-year-old female using the custom FIJI macro described in Appendix A.	24
6. Key output images from the isolation of lacunae and canaliculi in the intracortical envelope of the anterior femur of a 68-year-old male via CLSM in Dragonfly.	29
7. Regression analyses of SR μ CT pore histomorphometric variables.	36
8. Factorial ANOVA results of SR μ CT pore histomorphometric variables.	37
9. Regression analyses of SR μ CT lacunar histomorphometric variables.	38
10. Factorial ANOVA results of SR μ CT lacunar histomorphometric variables.	39
11. Representative 3D renders of SR μ CT pore and lacunar changes with age group.	40
12. Regression analyses of CLSM lacunar histomorphometric variables.	45
13. Factorial ANOVA results of CLSM lacunar histomorphometric variables.	46
14. Regression analyses of CLSM canalicular histomorphometric variables.	47
15. Factorial ANOVA results of CLSM canalicular histomorphometric variables. ...	48
16. Representative 3D renders of CLSM lacunar and canalicular changes with age group.	49

17.	Scout scan of a micro-computed tomography dataset of the proximal tibia.	63
18.	Representative 3D render of trabecular bone envelope in the proximal left tibia of a morphine group rabbit. Scale bar represents 5 mm.	64
19.	Superior view of the proximal tibia from a fentanyl group rabbit.	65
20.	Comparison of histomorphometric variables between morphine and saline animals.	68
21.	Comparison of histomorphometric variables by anatomical quadrant in morphine and saline animals.	72
22.	Comparison of histomorphometric variables between fentanyl and sham animals.	74
23.	Comparison of histomorphometric variables by anatomical quadrant in fentanyl and sham animals.	77
24.	Representative image showing certain geometric properties collected for each rib.	91
25.	Representative image of serial sections procured from each rib.	93
26.	Representative stress-strain curves showing the highly variable loading patterns seen in our sample.	95
27.	Representative stress-strain curve exhibiting post-peak behavior similar to the loading of rock.	96
28.	Comparison of geometric and biomechanical variables between morphine and saline animals.	98
29.	Comparison of geometric and biomechanical variables between fentanyl and sham animals.	100

LIST OF ABBREVIATIONS

ARF	Activation, Resorption, Formation
BMIT-BM	BioMedical Imaging and Therapy – Bend Magnet
BMU	Basic Multicellular Unit
BSU	Basic Structural Unit
CLS	Canadian Light Source
CLSM	Confocal Laser Scanning Microscopy
DOP	Delta (δ) Opioid Receptor
FITC	Fluorescein Isothiocyanate
HPA	Hypothalamus-Pituitary Axis
HPG	Hypothalamus-Gonadal Axis
KOP	Kappa (κ) Opioid Receptor
LCN	Lacuno-Canalicular Network
μCT	Micro-Computed Tomography
MES	Minimum Effective Strain
MOP	Mu (μ) Opioid Receptor
OGF	Opioid Growth Factor
OGFR	Opioid Growth Factor Receptor / Zeta (ζ) Opioid Receptor
OPG	Osteoprotegerin

OPIAD Opioid Induced Androgen Deficiency

RANK Receptor Activator of Nuclear factor Kappa-B

RANK-L Receptor Activator of Nuclear factor Kappa-B Ligand

ROI Region of Interest

SR μ CT Synchrotron Radiation-based μ CT

UARV University of Akron Research Vivarium

CHAPTER I

INTRODUCTION

The research described here examines the effects of prolonged opioid use on bone tissue and biomechanical properties to determine if and how opioids weaken bone. Opioid misuse has become an epidemic in the United States, leading to an average of 251 deaths per day in 2020, more than triple the 2010 rate¹. To accomplish these goals, we first examined cortical bone in a healthy state (i.e., without bone affecting conditions) throughout the human lifespan of both males and females to assess naturally occurring changes of bone microstructure. This provides a baseline from which to examine the effects of opioids in a model organism that renews bone similarly to that of humans (e.g., rabbits). Opioids may affect both overall bone strength and bone tissue microstructure. We utilized micro-Computed Tomography (μ CT) to examine, three-dimensionally, how trabecular bone microstructure differs between rabbit specimens treated with opioids or not. We finally examined how compression forces required to fracture a non-weight-bearing bone change in rabbits exposed to opioids. Through these experiments we hope to elucidate the effects of opioids on overall bone health to serve as foundational knowledge to 1) improve histological assessment techniques utilized in forensic anthropology, and 2) inform future biomedical investigations of the prolonged effects of opioid exposure on bone tissue.

Basic Bone Biology

Bone is a mechanosensitive tissue that continuously repairs itself throughout life. Bone serves numerous purposes including acting as a reservoir for calcium and phosphate, body support, and as sites for muscle attachment². Bone maintains its strength to withstand daily stresses through the related processes of modeling and remodeling³. Modeling serves to increase bone cross-sectional area and overall bone shape. Modeling can impact bone area and shape in numerous ways including drift and metaphyseal reduction. Drift causes bone to move its relative anatomical position to better withstand the mechanical forces of the growing individual⁴. To accomplish this in long bones (e.g., femur), bone tissue is deposited to both the medial endosteal and lateral periosteal envelopes while simultaneously being resorbed from the lateral endosteal and medial periosteal envelopes, resulting in a net drift of the bone laterally⁴ (Figure 1). The opposite can also occur, resulting in a net drift of the bone medially. Metaphyseal reduction is resorption of periosteal bone at the metaphysis until it reaches the diameter of the diaphysis, increasing diaphyseal length⁴. Metaphyseal reduction also requires expansion of the medullary cavity where endosteal and trabecular bone is resorbed in regions of the metaphysis undergoing reduction. Within the metaphysis, lamellar compaction can occur in porous spaces between trabeculae, converting cancellous bone into compact bone⁴. Modeling occurs predominately during adolescent growth; however, it is recruited after skeletal maturation to a limited degree and during fracture healing³. Alternatively, remodeling begins *in utero* and continues throughout life⁵. Remodeling serves multiple functions including mineral (e.g., calcium, phosphate) homeostasis, mechanical

adaptation of bone to changes in loading, and replacement of old or damaged bone tissue to ensure the survival of osteocytes, cells encased in bone that sense mechanical loading⁶

9.

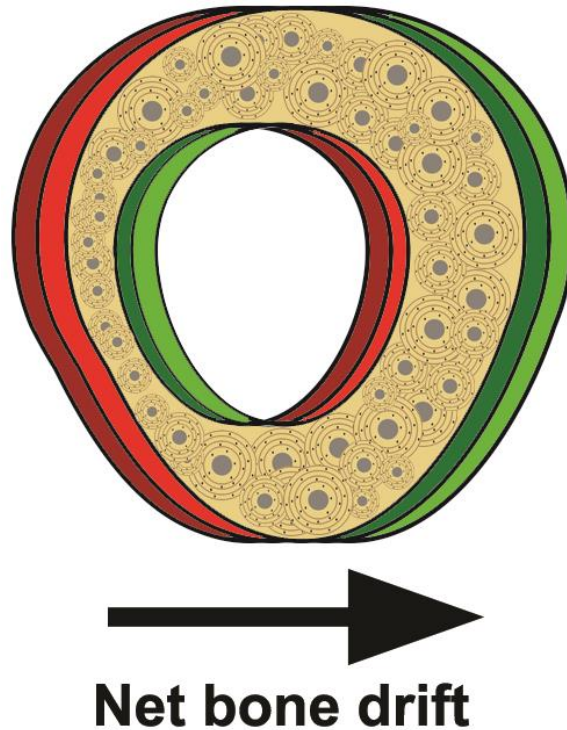


Figure 1. A schematic drawing or modeling unit. The bone (tan) is resorbed from the lateral endosteal and medial periosteal surfaces (red) and new bone is deposited on the medial endosteal and lateral periosteal surfaces (green), resulting in a net drift of bone laterally.

There are four primary cell types found within bone tissue that originate from hematopoietic and mesenchymal stem cells. Each serves a distinct purpose in overall bone health. Osteoclasts are multinucleated cells responsible for the removal of aged or damaged bone¹⁰. Osteoclasts achieve bone resorption through secreting acid which dissolves the mineral portion of bone. To remove the collagen fibers found in bone, osteoclasts produce collagenases⁶. Osteoblasts, conversely, are responsible for bone accretion. Mature osteoblasts are fated to one of three destinies: 1) most will reach their

limit depositing bone and undergo apoptosis^{6,11}, while others will either 2) reach an outer surface of bone tissue and transition into bone lining cells^{9,12,13}, or 3) are entombed in the bone matrix and become osteocytes^{9,11}. Bone lining cells are found covering inactive bone surfaces such as the outer surface and internal vascular canals (i.e., Haversian and Volkmann canals), preventing unregulated resorption of bone tissue and regulating ion transport through the interstitial fluid of bone and blood plasma¹⁴⁻¹⁷. Bone lining cells further interact with osteocytes to integrate mechanical signals into hormonal signals at the bone's surface and are thought to regulate signaling pathways involved in bone remodeling¹².

While osteoclasts and osteoblasts can function independently of each other, to influence growth and overall architecture of individual bones (bone modeling), they can also work together via remodeling to repair damage or increase local strength of bone tissue with increased use through increased mineralization¹⁸. This unique coupling of osteoclasts and osteoblasts during remodeling forms a Basic Multicellular Unit (BMU, Figure 2). Under normal conditions, a BMU will operate to balance bone resorption and formation such that there is limited net loss of bone tissue¹¹. A BMU follows the same steps, known as the ARF sequence, whenever remodeling occurs³ to create a Basic Structural Unit (BSU, secondary osteon). A secondary osteon differs from a primary osteon as a cement line is present in the secondary osteon, discussed below. The ARF sequence is named for three original steps of bone remodeling described by Harold Frost³: Activation, Resorption, Formation. The sequence has since been expanded to six phases including Activation, Resorption, Reversal, Formation, Mineralization, and

Quiescence^{19,20}. Knowledge of the ARF sequence is still being refined with current work suggesting a coupling of reversal and resorption, discussed below²⁰.

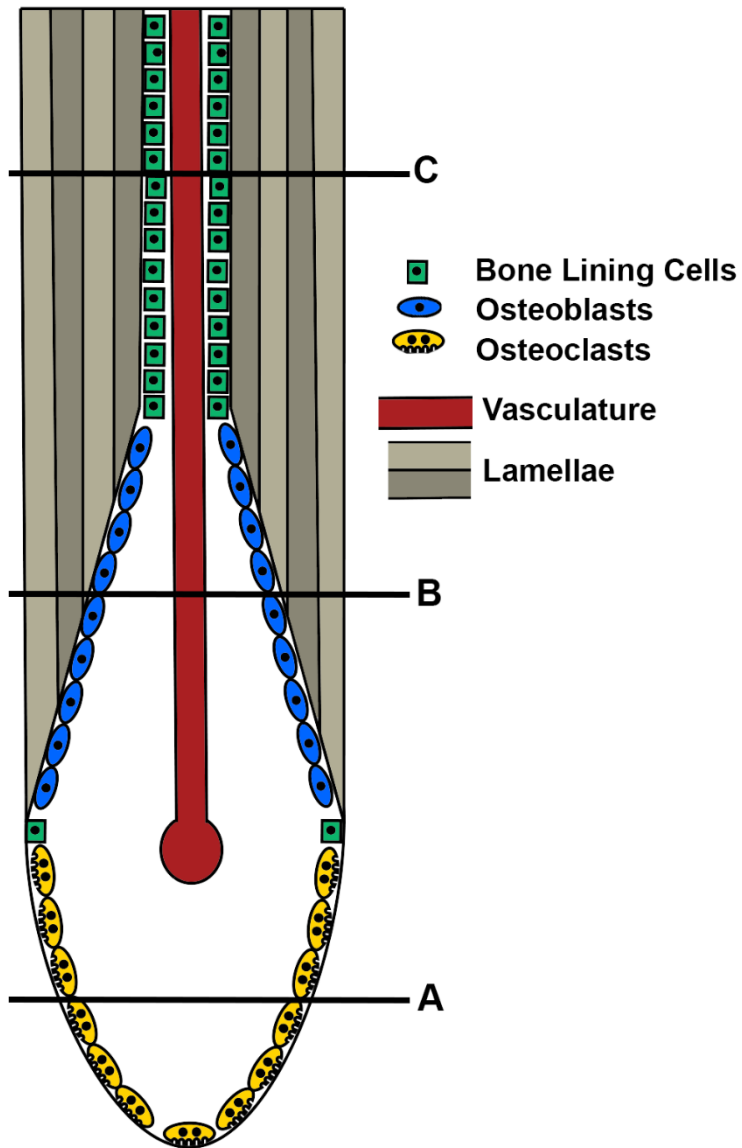


Figure 2. A schematic drawing of a Basic Multicellular Unit (BMU). The cutting cone of osteoclasts are resorbing bone, creating a resorptive bay (A) After resorption and reversal, osteoblasts deposit new osteoid in concentric lamellar rings (B). Formation is complete at C and the new osteon is functioning. The diameter of BMUs varies by species, therefore, no scale bar is included. Modified from Andronowski and Cole, 2021²¹.

Activation involves the systemic and local cellular signals that trigger bone remodeling. This includes recruiting preosteoclasts from hematopoietic stem cells and osteoblast precursor cells from mesenchymal stem cells in bone marrow and these cells traveling to the site of bone remodeling^{3,10,11}. Resorption follows activation and is identified by the initiation of osteoclast resorption of bone. This initial tunneling and resorption occurs on the surfaces of bone and is termed the cutting cone in a BMU^{3,22}. Recent studies^{23,24} have described different types of bone resorption cavities known as either pits or trenches. According to these studies, 90% of resorption begins as shallow, rounded pits resulting from stationary osteoclasts resorbing bone²³. These osteoclasts will transition to trench resorption, penetrating deeper into bone, in the presence of cathepsin K^{23,24}. Merrild and colleagues²⁴ further found osteoclasts from females resorb predominately through pit formation whereas males resorbed predominately through trench formation.

Following the resorption phase, other bone cells trail closely behind the cutting cone to begin the reversal phase of the ARF sequence^{6,9,13}. Recently, a new model of the reversal phase has emerged wherein osteoclasts recruit and comingle with local osteoprogenitor cells near the eroded bone surface, initiating the reversal phase²⁰. This new model somewhat blurs the line between reversal and resorption phases. The specific cells involved in the reversal phase are not currently known, but are believed to be either osteoprogenitor or bone-lining cells²⁰. These cells clear remaining bone debris from osteoclast resorption as well as smooth off the edges of the resorption canal. This gives osteoblasts a clean surface to begin depositing new bone. This is also where the reversal line, the thin outer boundary representing the zone of maximum resorption, characteristic

of a secondary osteon, is deposited^{6,13}. Following reversal, teams of osteoblasts begin depositing new osteoid, unmineralized bone tissue, in concentric rings, called lamellae, filling in the resorptive area carved by osteoclasts^{3,13}. The resorptive bay is mostly filled in during this formation phase, however, a central portion, termed the Haversian canal, is left open and is occupied by vasculature to supply the active BMU and resulting secondary osteon with nutrients^{11,18}. Osteoid deposited in the previous phase solidifies around the embedded collagen fibers during the mineralization phase¹⁹. Quiescence is the final phase of the ARF sequence and is defined by the disappearance of osteoclasts and transition of osteoblasts into either osteocytes or bone lining cells along the Haversian canal. This phase is when the mechanotransductive functions of bone cells begin in the newly formed BSU¹⁹. The ARF sequence, as just described, is specific to cortical bone remodeling. Trabecular bone remodeling follows the same sequence with some minor differences. Most notably, cortical resorption removes a roughly cylindrical packet of bone tissue (~200 μm diameter, in humans). Trabeculae are, generally, only 100-150 μm in diameter, leading to semi-circular cavities of bone being removed from the trabecular surface by osteoclasts and replaced by osteoblasts, resulting in a hemi-osteon²⁵.

Much of our knowledge of BMUs comes from 2D histomorphometric studies, which provides a limited view into BMU morphology and remodeling behavior²⁶. Remodeling that repairs damaged bone is referred to as targeted remodeling because the BMU is hypothesized to “seek out” damaged tissue^{8,10}. In targeted remodeling, while initially following the primary stress axis of the bone, the BMU is steered to damage in the bone through osteocyte signaling¹⁰. These signals are currently unknown, but are believed to be apoptotic signals from osteocytes¹⁰ and biochemical messengers including

nitric oxide, prostaglandin E2, and sclerostin moved through oscillating interstitial fluid flow^{15,27-30}. This, however, may not be the entire picture as certain species of teleost fish remodel bone, but osteocytes are not present in their bone tissue³¹. Once the BMU is clear of these biochemical signals, it is theorized to return to its original path along the primary stress axis¹⁰. Targeted remodeling, however, is thought to make up a relatively small portion (~30%)⁷ of all the remodeling events bone endures. More commonly, remodeling works to replace aging bone that is less mechanically sensitive or to maintain calcium-phosphate homeostasis in blood. Remodeling of this sort is termed non-targeted remodeling^{7,10,11}. During non-targeted remodeling BMU resorption is aligned with the primary stress axis of the particular bone¹⁰. For example, in the human femur, this axis is the superior-inferior axis. Disruptions in the processes of BMU remodeling are a hallmark of many chronic bone conditions such as osteoporosis¹¹. These disruptions can be triggered through numerous factors including opioid abuse³².

Remodeling Theories

There are multiple theoretical models of bone remodeling that have been presented in the literature. Notable examples include Roux's 1885 theory of dynamic interaction³³, Wolff's Law³⁴, and more recently, the Mechanostat theory³⁵ and Utah Paradigm³⁶. Wolff's Law contradicts Roux's theory, stating bone is genetically predetermined to manage loading and anything greater than this predetermined amount causes bone turnover to increase overall bone strength^{9,36}. Wolff's Law uses static math for bone loading which focuses on peak strain, meaning a certain amount of force applied to a bone will produce the same amount of remodeling regardless of how often the bone

is subjected to that force⁹. Wolff's Law, as it was posed originally, has since been discredited³⁷. A new theory, the Mechanostat proposed by Frost¹⁸, supplemented Wolff's Law, but posits the peak strain a bone is subjected to is less important than the number of loading events within a strain range³⁶.

The Mechanostat theory introduced the concept of strain ranges and their effects on bone modeling. These ranges are based on the average strain each region of bone endures³⁶. The physiologic range is where bone is being loaded adequately enough for osteocytes to effectively communicate through fluid flow oscillations from loading. Anything below the physiologic range indicates that bone is overbuilt for its needs and bone resorption will be employed to remove redundant structures. Average bone loading above the physiologic range means bone is being overused and is at risk of increased damage. In these cases, primary bone is rapidly deposited to increase the cross-sectional area of bone, and subsequently remodeled, to become stronger^{12,36}. Even further past the overuse range is the pathologic range. Bone in this range suffers from disease or trauma triggering repair (targeted) remodeling instead of maintenance (non-targeted) remodeling seen in the overuse range^{12,36}. Each of these ranges is defined by a minimum effective strain (MES) related to the type of bone renewal (i.e., remodeling, modeling, or repair) involved with each strain range. Remodeling (MESr) begins between 50-100 microstrain ($\mu\epsilon$), modeling (MESm) at 1000-1500 $\mu\epsilon$, and repair (MESp) begins at 3000 $\mu\epsilon$ ³⁸. These ranges can be altered by various factors including changes in blood concentrations of hormones (e.g., estrogen, parathyroid hormone) and pathologic states such as osteoporosis^{18,39}. Microscopic fatigue damage to bone (i.e., microdamage) can form from routine strain of bone within the physiologic range. Bone strain that occurs above the

repair (MESp) threshold may cause microdamage to coalesce into microcracks, leading to fractures³⁸.

The Mechanostat formed the basis for the Utah Paradigm, a collection of modern theories seeking to explain the process of bone tissue microstructural dynamics and the many complex pathways that control it. The Utah Paradigm began as a number of multidisciplinary hard tissue workshops at The University of Utah in 1995, combining multiple streams of evidence and bridging numerous subfields (e.g., medicine, orthopedic surgery, skeletal biology) which led to the development of the modern theory of skeletal physiology^{9,36,40}. The Utah Paradigm states that mechanical forces are the driving force of bone remodeling (the Mechanostat theory), but can be affected by non-mechanical influences including hormones, genetics, sex, and age^{9,40}.

A primary flaw of the Mechanostat theory is that it is based on loading strain. It does not account for remodeling in non-weight bearing bones, for example, such as those of the cranium. The Principle of Cellular Accommodation theory is applied as an addendum to the Mechanostat theory attempting to address how bones which are not routinely loaded are still able to remodel³⁹. The Principle of Cellular Accommodation theory suggests a strain range making up the loading curve seen in the Mechanostat can be adjusted based on region of the body. For example, the limb bones undergo more loading than the frontal bone as the limbs bear much of the body's weight in quadrupedal animals. In bipedal animals, the upper limbs do not normally bear body weight. Because of these varying strain ranges for weight-bearing and non-weight-bearing bones, underuse in the femur may be considered in the normal physiological range for a cranial bone. These ranges can be adjusted for individual bones and for disease states such as

osteoporosis³⁹. A further theory by Martin⁴¹, the Osteocyte Inhibitor Theory, suggests the cyclic fluid flow over osteocytes produced by loading, elicits a signal from the osteocytes to confirm normal functionality of the bone tissue. When microdamage is introduced, this signal is lost and BMUs are activated. Conversely, if bone is insufficiently loaded, this reduced cyclic fluid flow is not enough to meet the metabolic needs of the osteocytes, causing apoptosis and BMU activation. In both these situations, osteocytes prevent BMU activation under normal conditions through cell signaling. It is only once the lacuno-canalicular network is interrupted that bone remodeling is triggered. There is, however, limited evidence of Osteocyte Inhibitor Theory and this theory remains debated⁹.

Bone Cell Signaling Axes

Bone turnover is regulated through a complex system of signaling pathways of both local and systemic factors to regulate osteoclast and osteoblast function^{6,13,15}. These pathways serve important clinical roles in metabolic bone diseases (e.g., osteoporosis)⁴². The Wnt signaling pathway causes mesenchymal stem cells found in the bone marrow to commit to becoming osteoblasts through the actions of β -catenin^{6,13}. Sclerostin is produced by osteocytes and works as an antagonist to the Wnt pathway by preventing Wnt from binding to the Lrp5 receptor¹³, thereby preventing the maturation of osteoblasts. Regular mechanical loading of bones prevents buildup of sclerostin in interstitial fluid near osteoblasts due to cyclic fluid flow, promoting bone formation¹³. Osteoclasts mature through RANK-L/osteoprotegerin (OPG) signaling¹⁵. RANK-L is a ligand produced by osteoblasts which binds to RANK receptors found on the osteoclast surface, allowing immature osteoclasts to mature and triggering bone resorption^{13,15} (Figure 3). Osteoblasts further produce OPG, a decoy receptor for RANK-L that

competes with RANK for RANK-L. The binding of RANK-L to OPG limits the available RANK-L for RANK to bind with, inducing osteoclast apoptosis, thereby limiting bone resorption and the relative amounts of OPG and RANK-L produced functions to finely tune bone resorption in response to mechanical loading^{13,15}.

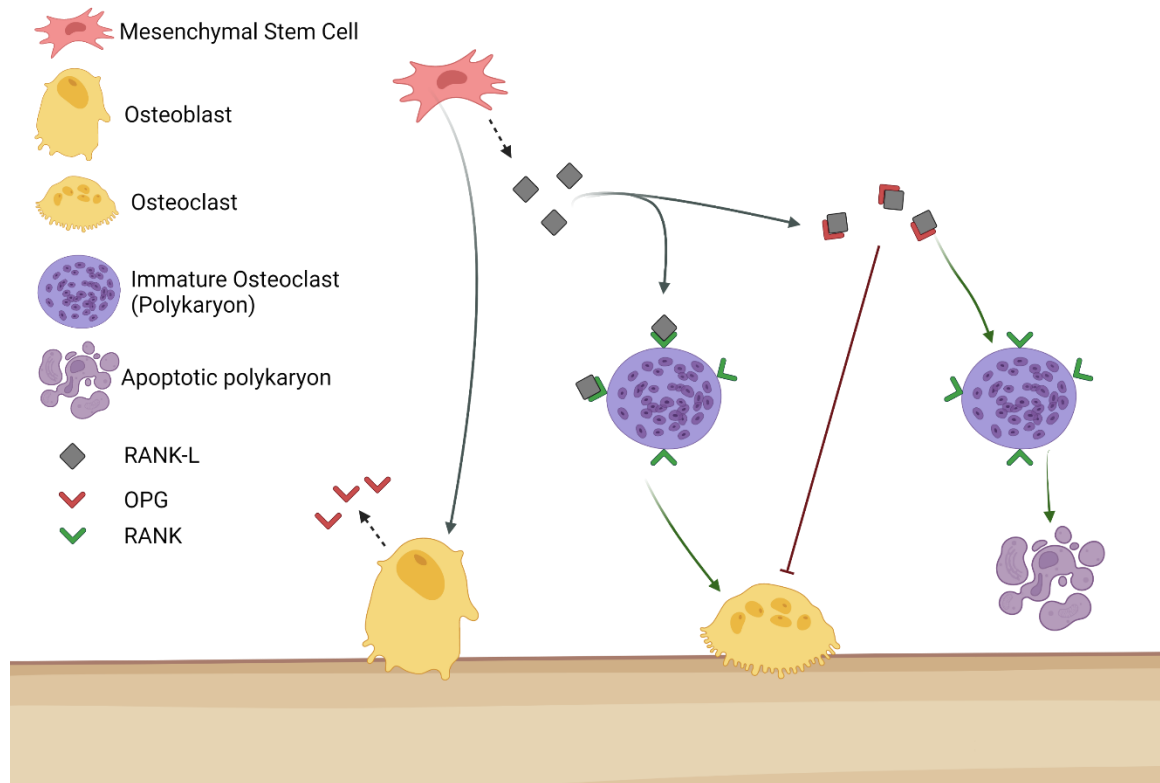


Figure 3. RANK/OPG signaling axis. Mesenchymal stem cells release RANK-L and mature into osteoblasts which secrete osteoprotegerin (OPG). RANK-L can bind to RANK on the surface of immature osteoclasts to trigger maturation into a functional osteoclast. Alternatively, RANK-L can bind to OPG to prevent maturation. In these cases, the immature osteoclast undergoes apoptosis. Created with BioRender.com

The previous discussion of biochemical components involved in bone modeling and remodeling focused on local factors influencing bone cells. Systemic hormones also play a critical role in bone maintenance. Estrogen serves numerous functions by directly binding to bone cells at the estrogen receptor-alpha ($ER\alpha$) on the surface of these cells.

Through estrogen binding, osteoblasts and osteocytes are more responsive to mechanical loading and osteoclasts are inhibited from bone resorption due to limited RANK production in osteoblasts³². Estrogen further limits cytokine release by T cells which are required for osteoclast differentiation^{32,43}. A decrease in estrogen concentrations leads to increased bone remodeling, with a preference for bone resorption due to higher rates of osteoblast apoptosis and RANK-L production⁶. The decline of serum estrogen during menopause in females can lead to osteoporosis⁶.

Parathyroid hormone (PTH) further helps control the metabolic functions of bone, having both anabolic and catabolic functions, depending on its concentration and duration of exposure (e.g., intermittent or constant). Under normal circumstances, PTH inhibits sclerostin secretion and osteoclast differentiation, limiting bone resorption^{44,45}. When there is increased PTH concentration, however, more RANK-L and less OPG is produced, leading to increased bone resorption⁴⁴. PTH is further required for bone to sense mechanical loading as is growth hormone, however the specific pathways have not yet been discerned^{9,39}. Calcitonin, alternatively, binds to receptors on the osteoclast cell surface, where it prevents the cytoskeletal reorganization of the osteoclasts which creates the ruffled margin of the osteoclast where bone resorption occurs and prevents the secretion of tartrate-resistant acid phosphatase by osteoclasts, the substance that actively dissolves the mineral portion of bone during resorption^{6,45}. Calcitonin further promotes the absorption of serum calcium into bone⁴⁵.

As stated previously, various pharmacologic agents can disrupt bone remodeling by affecting the various signaling pathways described above. Opioids are one such agent. Opioids are any exogenous drug which binds to opioid receptors to induce analgesia

along the periventricular areas of the midbrain, pons, and dorsal horns of the spinal cord^{46,47}, and can be blocked by an opioid antagonist such as naloxone (brand name: Narcan)⁴⁶. The experiments herein aim to elucidate the effects of opioids on overall bone health. A brief description of the current opioid epidemic is therefore warranted.

United States' Opioid Epidemic

The addictive nature of opioids makes them one of the most misused medication classes⁴⁸. Opioids are further linked to high rates of overdose deaths in the United States with fully synthetic opioids (e.g., fentanyl) comprising the majority of these deaths¹. While the rates of total opioid overdose deaths have been rising since 1999, semi-synthetic (e.g., hydrocodone; Brand name: Vicodin) and naturally-derived (e.g., morphine) opioid overdose rates have been dropping since 2017 while synthetic opioids are increasing rapidly¹ (Figure 4). As this epidemic shows no signs of slowing, it is imperative we learn about the various effects of opioids on the body and overall health, including bone health. By learning more about the effects of opioids on bone health, we can work to address common comorbidities of opioid use.

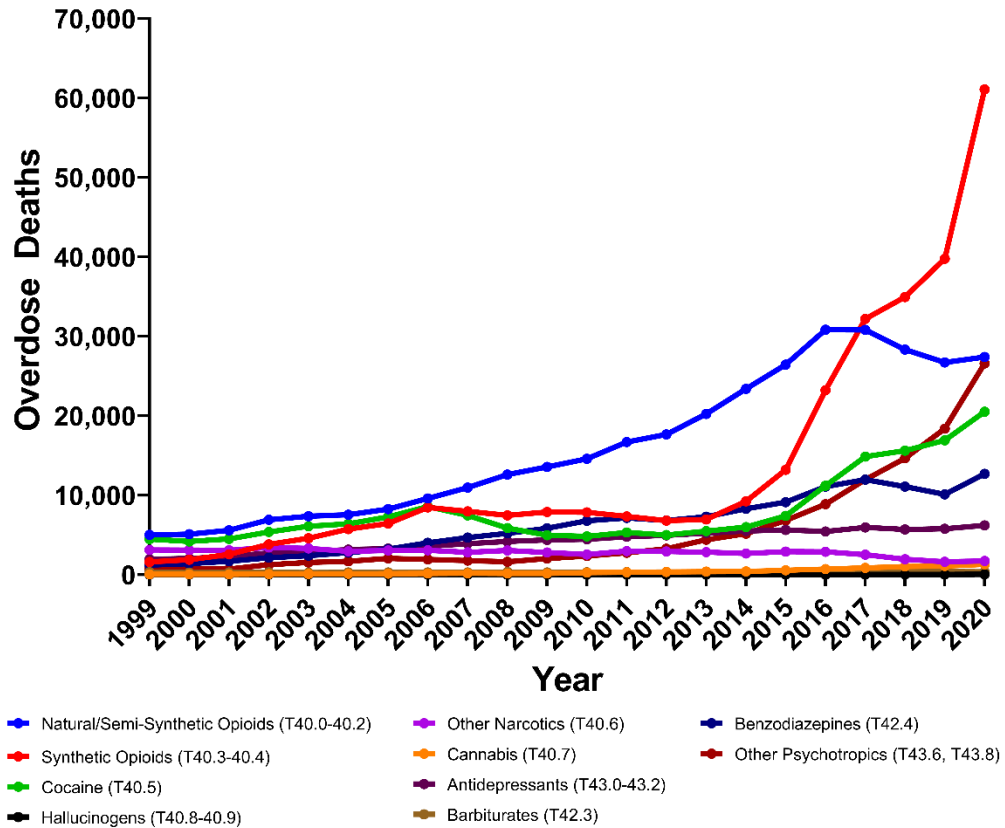


Figure 4. Drug overdose deaths in the United States from 1999-2020. Note the sharp rise in death rates due to synthetic opioids (including fentanyl) beginning in 2014. Legend indicates drug class and the International Classification of Diseases – 10th Revision (ICD-10) code(s) in parentheses. This figure was created using publicly available data from Centers of Disease Control and Prevention WONDER database³⁸.

Effects of Opioid Exposure on Bone

Endogenous opioids, such as proenkephalin, enkephalin, and met-enkephalin, all play roles in bone modeling and remodeling. Many of these opioids tend to be relegated to the perinatal period. Both proenkephalin and enkephalin play roles in bone development, growth, and remodeling but, after birth, proenkephalin becomes undetectable in the body³². Met-enkephalin, also known as Opioid Growth Factor (OGF), binds to Opioid Growth Factor Receptor (OGFR, alternatively known as zeta (ζ) opioid

receptor). The OGFR is a non-canonical opioid receptor and shares no structural homology with the other three opioid receptors (MOP, DOP, KOP)⁴⁹. Interactions between OGF and OGFR regulate osteogenesis and prevent bone growth by limiting p21 activation during osteoblast differentiation from mesenchymal stem cells^{49,50}. Opioid antagonists such as naltrexone or naloxone (brand name: Narcan) are more effective at binding to OGFR than other opioid receptors⁴⁹. Previous studies showed dosing with naltrexone increased bone formation in mice osteoblasts⁵⁰ and human bone marrow⁴⁹.

Beyond analgesia, opioids can cause various endocrine problems. Opioids bind to receptors along the hypothalamus-pituitary-adrenal/gonadal (HPA/HPG) axes and limit the production of androgen hormones, a condition known as Opioid-Induced Androgen Deficiency (OPIAD), and other related hormones^{32,51-53}. The prevalence of endocrine effects with prolonged opioid use is as high as 90% in patients using opioids for chronic pain management⁵². Estrogen concentration can be decreased resulting from hypogonadism from the HPG effects of prolonged opioid use⁴⁶. This can lead to opioid-induced osteoporosis^{32,53,54}. As mentioned above, estrogen is critical to bone maintenance through its effects on increasing mechanosensitivity of osteoblasts and osteocytes and limiting the differentiation of osteoclasts. A decrease of serum estrogen caused by opioid use may mimic type I osteoporosis (post-menopausal osteoporosis)⁶. Prolonged opioid use further decreases bone mineral density⁵⁵. The strain windows described by the Mechanostat theory naturally vary throughout the body and even within skeletal elements based on the amount of routine loading encountered by that bone. As bone cells are sensitive to estrogen, any deficiency may cause the body to deem what would otherwise be physiologic bone strain as underuse resulting in bone resorption^{12,32,43} as evidenced by

lower bone mineral density in opioid users^{32,55,56}. This may further cause inadequate maintenance of bone tissue for the loads it regularly encounters, thereby increasing fracture risk⁵⁷.

Organization of Dissertation

The goal of this dissertation is to elucidate the effects of opioids on overall bone health to improve histological assessment techniques utilized in forensic anthropology and inform future biomedical investigations of the prolonged effects of opioid exposure on bone tissue. As stated above, opioids can cause osteoporosis mimicking age-related osteoporosis. Therefore, examining the similarities between age-related and opioid-induced bone changes could prove beneficial. To these ends, we examined the effects of aging and opioid use on bone microarchitectural and biomechanical properties. Chapter II examined how the porous network in cortical bone changes throughout the human lifespan and differs between the sexes utilizing Synchrotron Radiation-based micro-Computed Tomography (SR μ CT) and Confocal Laser Scanning Microscopy (CLSM) collected over the span of three years (2018-2020) at Canadian Light Source (CLS; Saskatoon, SK, Canada), Northeast Ohio Medical University (NEOMED; Rootstown, OH, USA), and The University of Akron (Akron, OH, USA). Chapter III examined how trabecular bone in the proximal tibial epiphysis changes with opioid use through histomorphometry. This study is part of a larger study examining both cortical and trabecular bone changes in rabbit hindlimb bones following treatment with opioid analgesics for eight weeks. Chapter IV examined ribs from the same rabbits used in Chapter III using material testing equipment to determine if bones of animals dosed with

opioids fracture more readily or require less force than control animals. This chapter comprises the integrated component of this dissertation, a requirement of the Integrated Bioscience doctoral program at The University of Akron, discussed further in Chapter IV.

Each of the following chapters were completed in collaboration with other researchers and facilities. Chapter II was completed in collaboration with Drs. Janna M. Andronowski, Mary E. Cole, Christine Dengler-Crish, Matthew Smith, David M.L. Cooper, as well as graduate and undergraduate students in the Andronowski Lab including Randi Depp, Gina Tubo, and Joshua Taylor. It has been submitted as a peer-reviewed article to *The Anatomical Record*. Chapter III was completed in collaboration with Drs. Janna M. Andronowski and Mary E. Cole. This chapter will be submitted as part of a larger project examining the effects of opioids on cortical and trabecular bone envelopes of weight-bearing bones. It is currently in preparation as a peer-reviewed article for the journal *Micron*. Chapter IV was completed in collaboration with Drs. Janna M. Andronowski and Henry Astley, Hope Zimmerman, and instrumentation scientist for Akron Polymer Training Services (APTS), Nancy Concepcion. This chapter is being prepared for submission to the journal *Experimental Results*.

CHAPTER II

FEMORAL OSTEOCYTE LACUNO-CANALICULAR NETWORK AND
VASCULAR PORE CHANGES ACROSS THE HUMAN LIFESPAN EXAMINED
VIA SR μ CT AND CLSM

Introduction

Bone remodeling, described in Chapter I, is a coordinated process by which organized teams of bone cells remove old or damaged tissue throughout life to replace it with new packets of bone (basic structural unit, BSU)²⁵. During remodeling, osteoblasts that become embedded within the new bone tissue transition into osteocytes housed in small pores known as lacunae. Osteocytes comprise approximately 95% of all bone cells and work as mechanotransductive cells to monitor bone health⁵⁸. Osteocytes communicate with each other via cellular processes anchored in narrow channels, canaliculi, connecting their lacunae^{15,59}. Bone remodeling maintains structural integrity and cell signaling through the osteocyte lacuno-canalicular network (LCN)^{3,13}.

Osteocytes maintain the homeostasis of bone remodeling through multiple means including mechanical strain and biochemical signaling. Cyclic fluid flow from areas of high to low strain causes shear stress and deformation of the canalicular anchor proteins of the osteocyte, causing mechanically-gated calcium channels to open, allowing for extracellular calcium uptake^{13,15}. The osteocyte further releases nitric oxide which impedes osteoclast recruitment, preventing bone resorption⁶⁰. A lack of mechanical strain

from bone loading causes an accumulation of sclerostin, a Wnt inhibitor, limiting osteoblast maturation^{15,61}. Disruption of these homeostatic mechanisms is a common factor in age-related and pathologic bone loss and can be caused by sex steroid decline, and reduced bone loading resulting from decreased physical activity^{62,63}.

Declines in bone quality and quantity can result from changes in cortical porosity and the LCN resulting from dysregulated bone remodeling homeostasis. Studies focusing on various microstructural parameters of individual skeletal elements comprised predominantly of either cortical or cancellous bone have indicated decreases in lacunar density in humans with advancing age⁶⁴⁻⁷⁰ and fewer canaliculi associated with individual lacunae⁷¹. Many of these studies examined bone using 2D imaging techniques. With recent advancements in imaging, 3D assessment of a larger region of interest is possible which provides a more complete picture of changes in the tissue.

Standard laboratory micro-Computed Tomography (μ CT) can provide resolutions capable of imaging large cortical pores such as Haversian canals and resorptive areas in 3D, but, until recently, common laboratory models lacked adequate resolution for the much smaller lacunar spaces⁷². Synchrotron radiation-based μ CT (SR μ CT) is the preferred imaging method for non-destructive examination of lacunae^{26,72,73}, but some systems similarly lack the resolution required for imaging canaliculi. To capture a complete picture of bone microstructure, we propose coupling SR μ CT imaging with supplemental confocal laser scanning microscopy (CLSM) to visualize age-associated changes in the LCN of the human femoral diaphysis. CLSM has proven an effective method for lacuno-canalicular imaging⁷⁴. Previous studies have used these imaging modalities to examine bone, but either did not account for sex differences⁶⁷, age

differences⁷⁵, or 2D imaging was utilized⁶⁴ which may underestimate lacunar morphometry owing to the nature of taking a single cross-section.

Our objective is thus to examine the anterior femoral diaphysis utilizing two 3D imaging techniques (SR μ CT and CLSM) to determine how both vascular pores and the LCN differ between sexes and across the lifespan. The anterior femur was selected for this study as it is a common site of analysis for forensic age-at-death estimation²¹. We specifically hypothesize pore size, connectivity, and percent porosity will increase with advancing age. We further hypothesize that percent lacunar volume, network connectivity, lacunar diameter, and canalicular diameter will decrease with advancing age. We anticipate that this change will be exacerbated in females owing to the menopausal shift in serum estrogen concentration⁵⁹, a critical hormone involved in bone maintenance⁶.

Materials & Methods

Embalmed left femoral diaphysis sections were procured from modern cadaveric donors from Northeast Ohio medical school dissecting rooms. Unembalmed forensic samples were collected from U.S. medical examiners' offices. Informed consent for each donor was gathered from the donor themselves or their next-of-kin. Our sample included 14 males and 11 females ($n = 25$) aged 19 to 101 years at death (mean = 55.32). Cause of death, age, and sex were available for each individual and no donor had any known bone-affecting conditions nor treatments. The University of Akron Institutional Review Board for the Protection of Human Subjects (IRB) deemed these specimens exempt from full review as they were gathered from deceased individuals.

Specimens were soaked in a protease solution heated to 45°C for three hours and macerated following standard protocol⁷⁶. Remaining soft tissue was removed with dental tools and the medullary cavity was cleared of marrow using a handheld water flosser (e.g., WaterPik). Macerated specimens were soaked in 70% ethanol at 4°C for 24 hours to remove lipids. Specimens were then air-dried at ambient temperature for 24 hours.

SR μ CT Preparation and Imaging

We prepared bone cores for SR μ CT imaging using a geological technique adapted for bone⁷⁷. A 5 mm transverse section was cut using a Buehler IsoMet 1000 precision saw (Buehler, Lake Bluff, IL) fitted with a diamond-tipped blade. Transverse sections were mounted to an aluminum tin with thermal epoxy and mounted to a mill-drill press. A 2 mm inner diameter hollow coring bit was used to procure samples from the anterior aspect of the femoral section while avoiding endosteal, periosteal, or trabecularized regions of the cortical bone. Core samples were stored in microcentrifuge tubes at ambient temperature until imaging on the BioMedical Imaging and Therapy-Bend Magnet (BMIT-BM) beamline at the Canadian Light Source (CLS) national synchrotron facility⁷⁸.

Experiments on the BMIT-BM utilized a white beam microscope with a 5x objective lens with scan parameters shown in Table 1. At the time of our experiments, prior to the implementation of continuous electron injections, the X-ray storage ring peaked at 250 mA after electron injection. The current decayed over a 12-hour period until the next injection of electrons. X-ray exposure was previously manually adjusted during experiments to account for the variable current and maintain 20% saturation of the

detector. Core samples were mounted to a brass peg with cyanoacrylate and centered on a goniometer to ensure the samples remained centered in the field of view (FOV) and did not shift during imaging.

Table 1. SR μ CT system experimental settings on BMIT-BM.

Pixel size	1.44 μ m
Sample-detector distance	5 cm
Total specimen rotation	180°
Flat and darkfield projections	20 of each
Exposure time	30-35 ms (depending on current)
Filters used	2 mm Aluminum
Total number of projections	2500

SR μ CT Image Processing

Datasets, comprised of 2500 projections spanning 3.084 mm in height, were reconstructed with Ufo-kit⁷⁹, a Linux-based proprietary software utilized at CLS. A 1.2 mm region of interest (ROI) was isolated from the center of the FOV using FIJI⁸⁰ with care to avoid the edges of the sample as well as any deep ring artifacts (dark grooves in Figure 5A). As for the specific location of the ROI in the dataset, the center of the FOV was selected as it is the focal point of the X- ray beam and, therefore, has the clearest data, limiting potential artifacts. Datasets were binarized and lacunae were isolated from Haversian and resorptive pore spaces with a FIJI⁸⁰ macro developed by Dr. Mary E. Cole, described in Appendix A. Briefly, reconstructed images had a threshold applied to them and were despeckled to remove noise. Large vascular pores were filled in to remove noise from soft tissue remnants and isolated from lacunae (Figure 5C, D). Morphometric variables were collected using CTAnalyser v. 1.18.4.0 (Bruker microCT, Kontich, Belgium). Vascular pore variables included % Pore Volume, Pore Surface : Volume

ratio, Pore Diameter, and Pore Separation. Lacunar variables included % Lacunar Volume, Lacunar Surface : Volume ratio, Lacunar Diameter, Lacunar Separation, and Lacunar Density. A description of these variables can be seen in Table 2.

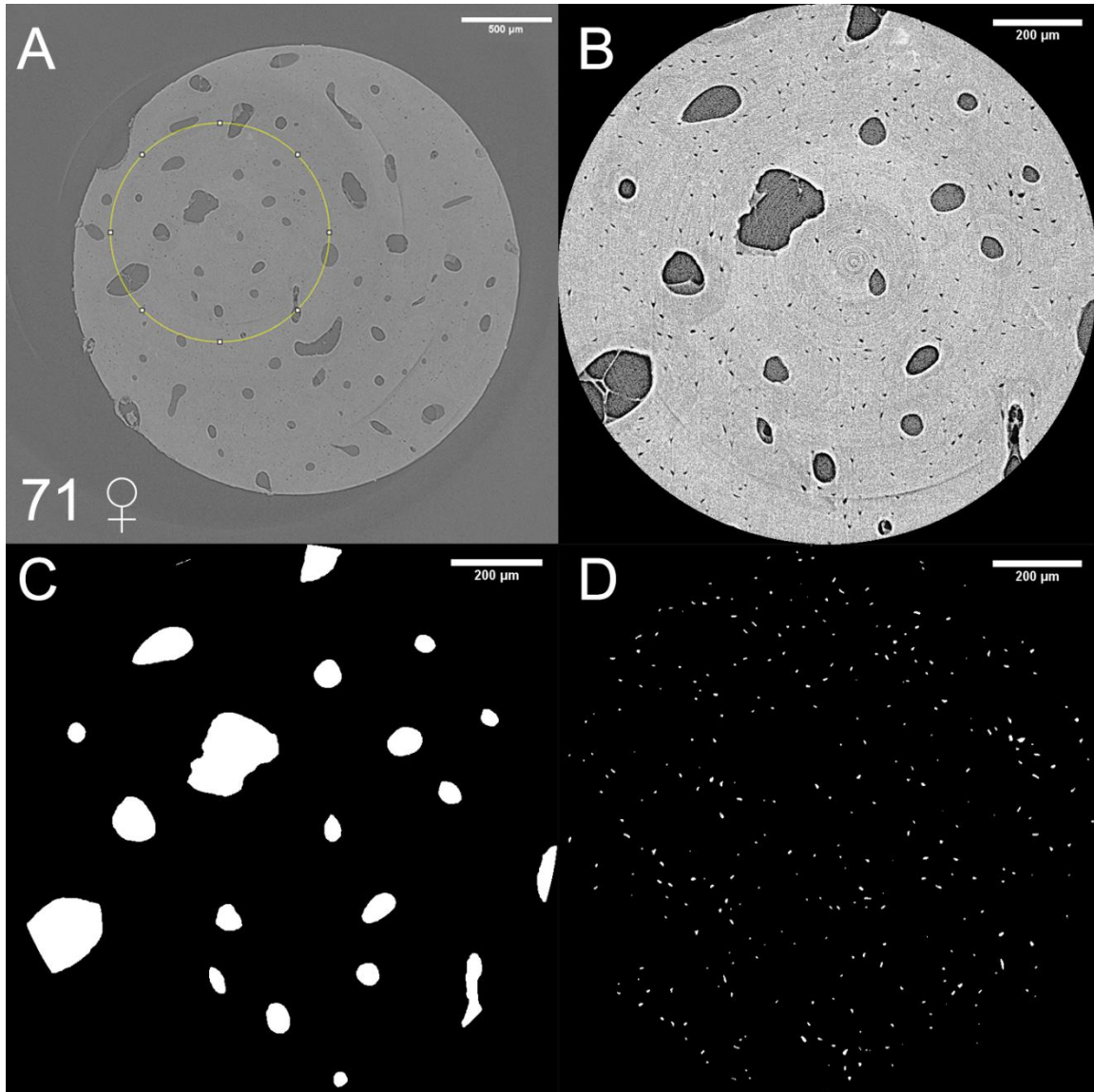


Figure 5. Key output images from the femur of a 71-year-old female using the custom FIJI macro described in Appendix A. An ROI (yellow ring) was selected (A), pores and lacunar spaces were selected within the ROI (B) and segmented by applying a threshold to isolate pores (C) from lacunae (D).

CLSM Preparation and Imaging

A 1 mm transverse cross-section was cut from each femoral diaphysis block adjacent to the section collected for SR μ CT imaging. The thin sections were ground to ~75 μ m thickness and polished using an EcoMet 30 grinder/polisher (Buehler). MasterPrep polishing fluid was used in combination with a polishing disk to remove striations introduced from grinding which would limit visibility of histologic structures during imaging. Samples were subsequently rinsed in an ultrasonicator filled with distilled water and dried between two microscope slides, to prevent warping, at ambient temperature before staining.

In an aluminum tin, we submerged dried specimens in 1% fluorescein isothiocyanate (FITC) solution (Sigma-Aldrich, St. Louis, MO) similar to previous studies⁷⁴. The tin was sealed and placed on a rotator set to low speed for four hours to allow for dye penetration. These procedures were performed in a dark room to prevent quenching of the fluorescent dye. After four hours, excess stain was removed by rinsing the specimen in three 20-minute washes of 100% ethanol. Specimens were then air-dried at ambient temperature between two microscope slides and mounted on glass slides with ProLong Glass medium (Fisher Scientific, Hampton, NH). Prepared slides were transferred to a light-blocking container and maintained at -20°C until imaging.

We imaged the anterior region of each prepared slide with a 63x objective lens applied with immersion oil (Immersion Oil 518F, Zeiss, Jena, Germany) on an inverted Leica TCS SPE confocal laser scanning microscope equipped with a motorized Z-Galvo stage (Leica Microsystems, Wetzlar, Germany). We used a 488 nm laser set to 32.5% intensity and a spectral window of 485-585 nm. The pinhole was 1 AU and zoom was set to 1.5x.

Three adjacent image stacks of the intracortical region, each measuring 116.4 x 116.4 x 29.99 μm , were acquired in 0.3 μm depth increments at a scanning speed of 400 Hz. This totaled 101 individual images per stack each at a resolution of 1024 sq. pixels. A number of specimens included in this study were procured from forensic cases and exhibited diagenetic alterations. As a result, certain regions became oversaturated with FITC at the periosteal and endosteal margins which prevented us from discerning microarchitectural features in these regions. We, therefore, excluded the endosteal and periosteal bone envelopes from analysis.

CLSM Image Processing

Each dataset was loaded in Leica Application Suite X (LAS X, Leica Microsystems) where gain and smart-offset were optimized to minimize noise. Each dataset had a total volume of $4.06 \times 10^5 \mu\text{m}^3$. The three individual datasets for each specimen were stitched using the Pairwise Stitching function of FIJI⁸⁰ and cropped to removed excess stain from the image perimeter. Stitched images were loaded in Dragonfly v4.1 (Object Research Systems, Montréal, Canada) and resampled at 0.3 $\mu\text{m}/\text{pixel}$ in each plane to produce cubic voxels from the original rectangular voxels. The LCN was auto-segmented in each 2D image, following resampling, using a custom macro in FIJI⁸⁰. This macro is detailed in Appendix B. Datasets were imported to Dragonfly for analysis following processing.

Large vascular pores (i.e., resorptive areas, Haversian canals) and microcracks were manually removed from the 3D renders in Dragonfly. Using a 3D erosion function, canalicular connections to lacunae were severed to isolate lacunae. A multi-ROI function

isolated each lacuna into its own ROI. To undo the erosion function and return the lacunae to their original morphologies, distance mapping and dilation functions were performed on the lacunar multi-ROI. Using a Boolean operation, the lacunar multi-ROI was subtracted from the original dataset to create a canalicular ROI (Figure 6).

Morphometric variables were collected using CTAnalyser similarly to the SR μ CT variables mentioned above. These variables included: % Lacunar Volume, Lacunar Surface : Volume ratio, Lacunar Diameter, Lacunar Separation, Lacunar Density, % Canalicular Volume, Canalicular Surface : Volume ratio, Canalicular Diameter, Canalicular Separation, Canalicular Connectivity Density, and Canalicular Density.

Descriptions of these variables can be found in Table 2. The CLSM image processing workflow and the following statistical analyses were performed by Joshua Taylor as part of the Tiered Mentoring Program at The University of Akron.

To calculate lacunar porosity, we divided Lacunar Volume from Tissue Volume. CTAnalyser calculates Lacunar Separation by placing numerous spheres between lacunae and reporting the average diameter of the spheres (sphere-fitting model). These calculations were completed using an ROI mask that had vascular pores removed as lacunae cannot exist in these pores. To calculate object density, we divided the number of objects in question (pores, lacunae, or canaliculi) from Tissue Volume with the other two associated object groups removed. As bone tissue is replaced throughout life, the age of bone tissue will vary from the age of the individual donor. For this reason, “chronological age” is used throughout to refer to the age of the donor.

Table 2. Description of morphometric variables.

Variable Name	Abbr.	Description
% Pore Volume	% Po.V	Pore Volume / Tissue Volume
Pore Surface : Volume	Po.S/Po.V	Pore Surface / Pore Volume
Pore Diameter	Po.Dm	Diameter of largest sphere fit within a canal
Pore Separation	Po.Sp	Diameter of largest sphere fit between canals
% Lacunar Volume	% Lc.V	Lacunar Volume / Tissue Volume
Lacunar Surface : Volume	Lc.S/Lc.V	Lacunar Surface / Lacunar Volume
Lacunar Diameter	Lc.Dm	Diameter of largest sphere fit within lacunae
Lacunar Separation	Lc.Sp	Diameter of largest sphere fit between lacunae
Lacunar Density	Lc.Dn.	Number of lacunae per unit volume
% Canalicular Volume	% Cn.V	Canalicular Volume / Tissue Volume
Canalicular Surface : Volume	Cn.S/Cn.V	Canalicular Surface / Canalicular Volume
Canalicular Diameter	Cn.Dm	Diameter of largest sphere fit within a canaliculus
Canalicular Separation	Cn.Sp	Diameter of largest sphere fit between canaliculi
Canalicular Connectivity Density	Cn.CoDn	Number of connections between canaliculi per unit volume
Canalicular Density	Cn.Dn	Number of canaliculi per unit volume

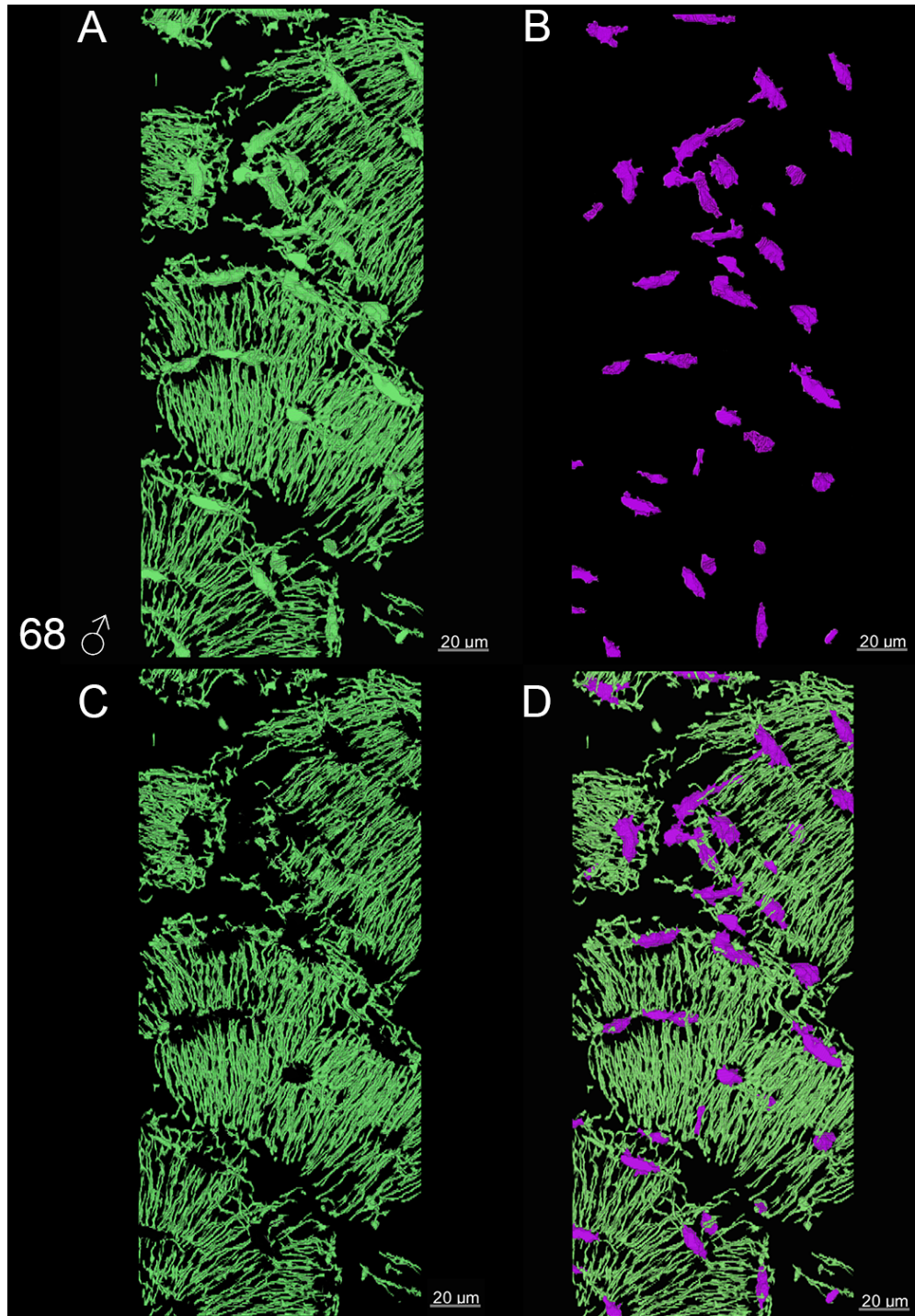


Figure 6. Key output images from the isolation of lacunae and canaliculi in the intracortical envelope of the anterior femur of a 68-year-old male via CLSM in Dragonfly. The initial 3D render (A) is eroded to sever connections between lacunae and canaliculi and a size-based multi-ROI is applied to isolate lacunae (B) and canaliculi (C). The combined multi-ROIs can be viewed in panel D.

Statistical Analysis

All data were analyzed using SPSS v26.0 (IBM, Armonk, NY). Linear regression was used to test relationships between morphometric variables and predictor variables (i.e., age, sex) and the interaction of age and sex quantitatively⁸¹⁻⁸³. Prior to analysis, variables were inspected for multi-collinearity. Residuals from these analyses were examined for normality and variance assumptions as recommended by various biostatistical texts^{81,84-87}. Any variable that violated assumptions were log₁₀-transformed and re-analyzed. If log₁₀ transformation of dependent variables did not correct assumption violations, we performed a bootstrapped^{88,89} regression analysis created from 1000 replicates. A summary of variables that required transformation or bootstrapped analysis can be found in Tables 3-4 (SRμCT) and 6-7 (CLSM). Since the age variable encompassed a broad span of 19-101 years and was not normally distributed due to small sample size, we created a categorical variable for age for use in alternative analyses. Age data were categorized into three evenly distributed groups based on broad life stages including: Young (19 – 44 years; mean age = 28.25 years; $n = 8$; F = 3, M = 5), Middle-Age (45 – 65 years; mean age = 56.38 years; $n = 8$; F = 3, M = 5), and Older (66+ years; mean age = 78.44 years; $n = 9$; F = 5, M = 4). Previous studies have used similar age categories for coding continuous age variables that have uneven distributions and wide variability^{64,67,71,90-93}. Three groups were chosen instead of two due to an uneven distribution of female donors towards the Older category, potentially artificially increasing age-related change while potentially limiting observed sex-related differences. More groups were not included as they would have fewer than three individuals of each sex, preventing statistical analysis. Age group and sex variables served as independent

variables in factorial analyses of variance (ANOVAs) with each relevant morphometric measure serving as a dependent variable. Step-down Bonferroni corrections (Appendix C) were performed to account for multiple comparisons and Tukey HSD post-hoc tests were used to identify specific age group differences to determine during which general stage of life changes in bone porosity occurs.

Results

SR μ CT

Regressions for vascular canal variables revealed that neither sex nor the interaction between sex and age was a significant predictor for any variable. Chronological age, however, was a significant predictor for Pore Surface : Volume. See Table 3 and Figure 7 for regression statistics including percent of variance explained for each variable. Significant differences between age groups was detected via factorial ANOVA for Pore Surface : Volume ($F[2,22] = 14.826, p < 0.001$) and Pore Diameter ($F[2,22] = 14.564, p < 0.001$). For both variables where age group was significant, effect size was classified as “large” with omega squared values of 0.513 and 0.495, respectively. Observed power exceeded 98% for both variables (Table 4). Tukey HSD post-hoc analyses between young, middle-age, and older age groups indicated young individuals displayed significantly greater Pore Surface : Volume ($p < 0.001$) and significantly decreased Pore Diameter ($p < 0.001$) than older individuals (Figure 8, Table 5).

Regressions further revealed neither sex nor the interaction between sex and age were significant predictors for any lacunar morphometric variable (Table 4, Figure 9).

Chronological age was a significant predictor for % Lacunar Volume. Factorial ANOVAs indicated no significant difference between age groups for any lacunar variable (Table 4, Figure 10). Representative 3D renders of vascular pore and lacunar differences between age groups can be seen in Figure 11.

Table 3. Regression results for SR μ CT variables compared by chronological age and sex⁸¹⁻⁸³. Bonferroni-corrected $\alpha = 0.001$.

Morphometric Variable (Data Transformation)	Fixed Factor	F	p-value	ω^2	Effect Size*	Observed Power
% Pore Volume (Log ₁₀)	Overall	6.080	0.004	0.379	-	91.90%
	Sex	0.554	0.465	-0.011	-	11.00%
	Age	16.376	0.001	0.382	-	97.10%
	Age*Sex	0.500	0.487	-0.012	-	10.60%
Pore Surface : Volume (No Transformation)	Overall	7.897	0.001	0.453	Large	97.20%
	Sex	0.284	0.600	-0.016	-	8.00%
	Age	22.659	<0.001	0.474	Large	99.50%
	Age*Sex	0.520	0.479	-0.010	-	10.60%
Pore Diameter (Bootstrap)	Overall	3.110	0.048	0.202	-	63.90%
	Sex	0.885	0.358	-0.004	-	14.60%
	Age	8.846	0.007	0.250	-	80.90%
	Age*Sex	1.169	0.292	0.005	-	17.80%
Pore Separation (Log ₁₀)	Overall	2.038	0.139	0.111	-	44.80%
	Sex	0.018	0.895	-0.035	-	5.20%
	Age	3.080	0.094	0.074	-	38.80%
	Age*Sex	0.075	0.778	-0.033	-	5.80%
Pore Connectivity Density (Bootstrap)	Overall	1.406	0.269	0.046	-	31.80%
	Sex	1.234	0.279	0.009	-	18.50%
	Age	2.347	0.140	0.051	-	31.00%
	Age*Sex	0.485	0.494	-0.020	-	10.20%
Pore Density (Log ₁₀)	Overall	5.210	0.008	0.336	-	86.90%
	Sex	1.478	0.238	0.013	-	21.30%
	Age	12.758	0.002	0.312	-	92.60%
	Age*Sex	0.418	0.525	-0.015	-	9.50%
% Lacunar Volume (No Transformation)	Overall	10.270	<0.001	0.527	Large	99.40%
	Sex	0.000	0.986	-0.019	-	5.00%
	Age	27.431	<0.001	0.500	Large	99.90%
	Age*Sex	0.004	0.949	-0.019	-	5.00%
Lacunar Surface : Volume (No Transformation)	Overall	3.693	0.028	0.244	-	72.20%
	Sex	0.293	0.594	-0.021	-	8.10%
	Age	9.493	0.006	0.257	-	83.60%
	Age*Sex	0.190	0.668	-0.024	-	7.00%
Lacunar Diameter (No Transformation)	Overall	4.577	0.013	0.300	-	81.80%
	Sex	0.221	0.643	-0.022	-	7.30%
	Age	11.025	0.003	0.281	-	88.60%
	Age*Sex	0.069	0.796	-0.026	-	5.70%

Table 3 (Continued)

Lacunar Separation (No Transformation)	Overall	6.730	0.002	0.407	-	94.40%
	Sex	0.596	0.449	-0.010	-	11.40%
	Age	16.704	0.001	0.372	-	97.30%
	Age*Sex	0.439	0.515	-0.013	-	9.70%
Lacunar Density (Log ₁₀)	Overall	0.509	0.680	-0.063	-	13.60%
	Sex	1.098	0.307	0.005	-	17.00%
	Age	0.238	0.631	-0.038	-	7.50%
	Age*Sex	0.921	0.348	-0.003	-	15.00%

*Effect size is determined from Cohen's⁹⁴ f modified for ω^2 as Small Effect > 0.0099, Medium Effect > 0.0599, and Large Effect > 0.1499.

Table 4. Factorial ANOVA results for SR μ CT variables compared by age group and sex. Bonferroni-corrected $\alpha = 0.001$.

Morphometric Variable (Data Transformation)	Fixed Factor	F	<i>p</i>-value	ω^2	Effect Size*	Observed Power
% Pore Volume (Log ₁₀)	Overall	4.385	0.008	0.404	-	90.00%
	Sex	0.623	0.440	-0.009	-	11.70%
	Age Group	9.126	0.002	0.388	-	95.00%
	AgeGrp*Sex	1.478	0.253	0.023	-	27.60%
Pore Surface : Volume (No Transformation)	Overall	6.772	<0.001	0.536	Large	98.60%
	Sex	0.105	0.750	-0.017	-	6.10%
	Age Group	14.826	<0.001	0.513	Large	99.70%
	AgeGrp*Sex	3.038	0.072	0.076	-	51.90%
Pore Diameter (Log ₁₀)	Overall	6.960	<0.001	0.544	Large	98.80%
	Sex	0.090	0.767	-0.017	-	5.90%
	Age Group	14.564	<0.001	0.495	Large	99.60%
	AgeGrp*Sex	3.629	0.046	0.096	-	59.80%
Pore Separation (No Transformation)	Overall	1.037	0.425	0.007	-	28.80%
	Sex	0.918	0.350	-0.003	-	14.90%
	Age Group	1.666	0.215	0.053	-	30.70%
	AgeGrp*Sex	0.066	0.937	-0.074	-	5.90%
Pore Connectivity Density (Bootstrap)	Overall	0.896	0.504	-0.021	-	25.10%
	Sex	0.902	0.354	-0.004	-	14.70%
	Age Group	1.609	0.226	0.050	-	29.70%
	AgeGrp*Sex	0.668	0.524	-0.027	-	14.60%
Pore Density (No Transformation)	Overall	3.050	0.035	0.291	-	74.80%
	Sex	1.644	0.215	0.018	-	23.00%
	Age Group	6.517	0.007	0.313	-	85.50%
	AgeGrp*Sex	1.436	0.263	0.025	-	23.00%

Table 4 (Continued)

% Lacunar Volume (No Transformation)	Overall	3.878	0.014	0.365	-	85.60%
	Sex	0.325	0.575	-0.017	-	8.40%
	Age Group	8.955	0.002	0.404	-	94.70%
	AgeGrp*Sex	0.381	0.688	-0.031	-	10.20%
Lacunar Surface : Volume (No Transformation)	Overall	1.744	0.173	0.129	-	47.50%
	Sex	0.703	0.412	-0.010	-	12.50%
	Age Group	3.621	0.047	0.183	-	59.70%
	AgeGrp*Sex	0.420	0.663	-0.040	-	10.80%
Lacunar Diameter (No Transformation)	Overall	2.490	0.068	0.230	-	64.70%
	Sex	1.239	0.280	0.007	-	18.50%
	Age Group	5.081	0.017	0.252	-	75.30%
	AgeGrp*Sex	0.228	0.798	-0.048	-	8.10%
Lacunar Separation (No Transformation)	Overall	2.688	0.053	0.252	-	68.50%
	Sex	0.006	0.940	-0.030	-	5.10%
	Age Group	4.608	0.023	0.216	-	70.90%
	AgeGrp*Sex	1.759	0.199	0.045	-	32.20%
Lacunar Density (No Transformation)	Overall	2.239	0.092	0.199	-	59.30%
	Sex	0.186	0.671	-0.026	-	6.90%
	Age Group	0.031	0.969	-0.062	-	5.40%
	AgeGrp*Sex	5.349	0.014	0.279	-	77.60%

*Effect size is determined from Cohen's⁹⁴ f modified for ω^2 as Small Effect > 0.0099, Medium Effect > 0.0599, and Large Effect > 0.1499.

Table 5. Tukey HSD post-hoc results for age group-significant SR μ CT variables. Bonferroni-corrected $\alpha = 0.001$

Morphometric Variable	Age Groups	<i>p</i>-value
Pore Surface : Volume	Young – Middle Aged	<i>0.018</i>
	Young – Older	<<i>0.001</i>
	Middle Aged – Older	0.111
Pore Diameter	Young – Middle Aged	<i>0.019</i>
	Young – Older	<<i>0.001</i>
	Middle Aged – Older	0.109

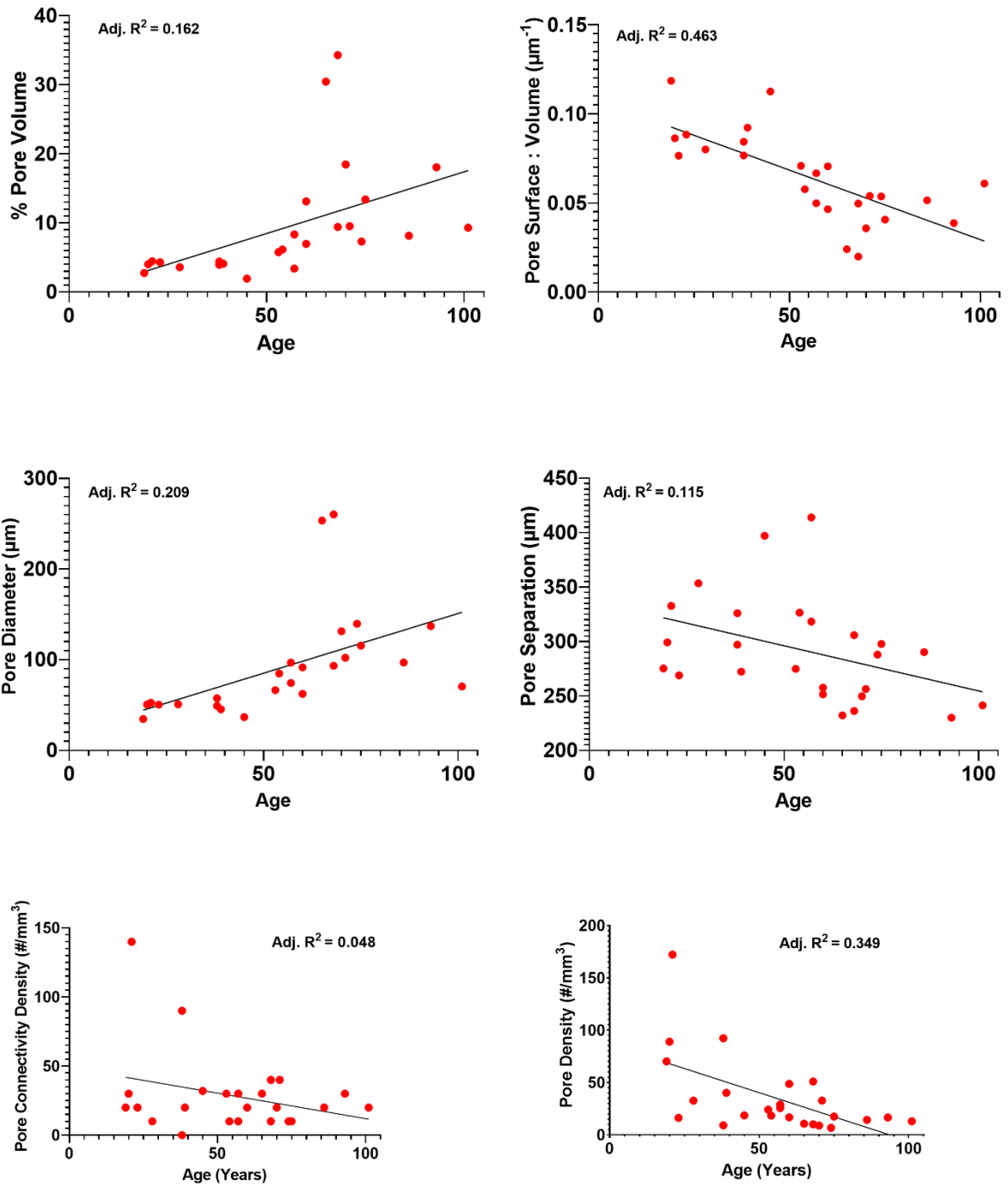


Figure 7. Regression analyses of SR μ CT pore histomorphometric variables. Adjusted R^2 is indicated at the top of each graph.

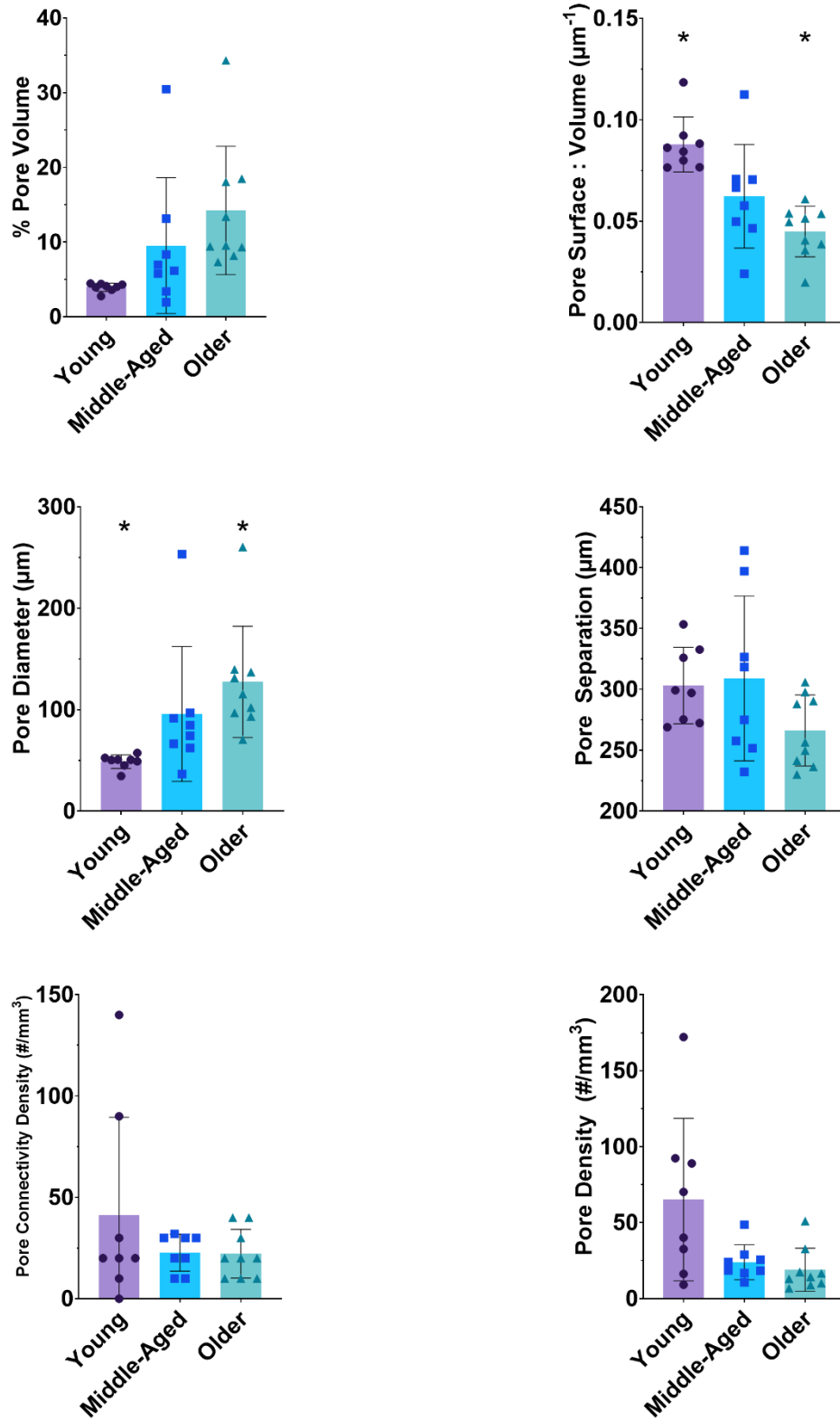


Figure 8. Factorial ANOVA results of SR μ CT pore histomorphometric variables. * and # indicate statistical significance ($p < 0.05$) between the age groups that share a symbol.

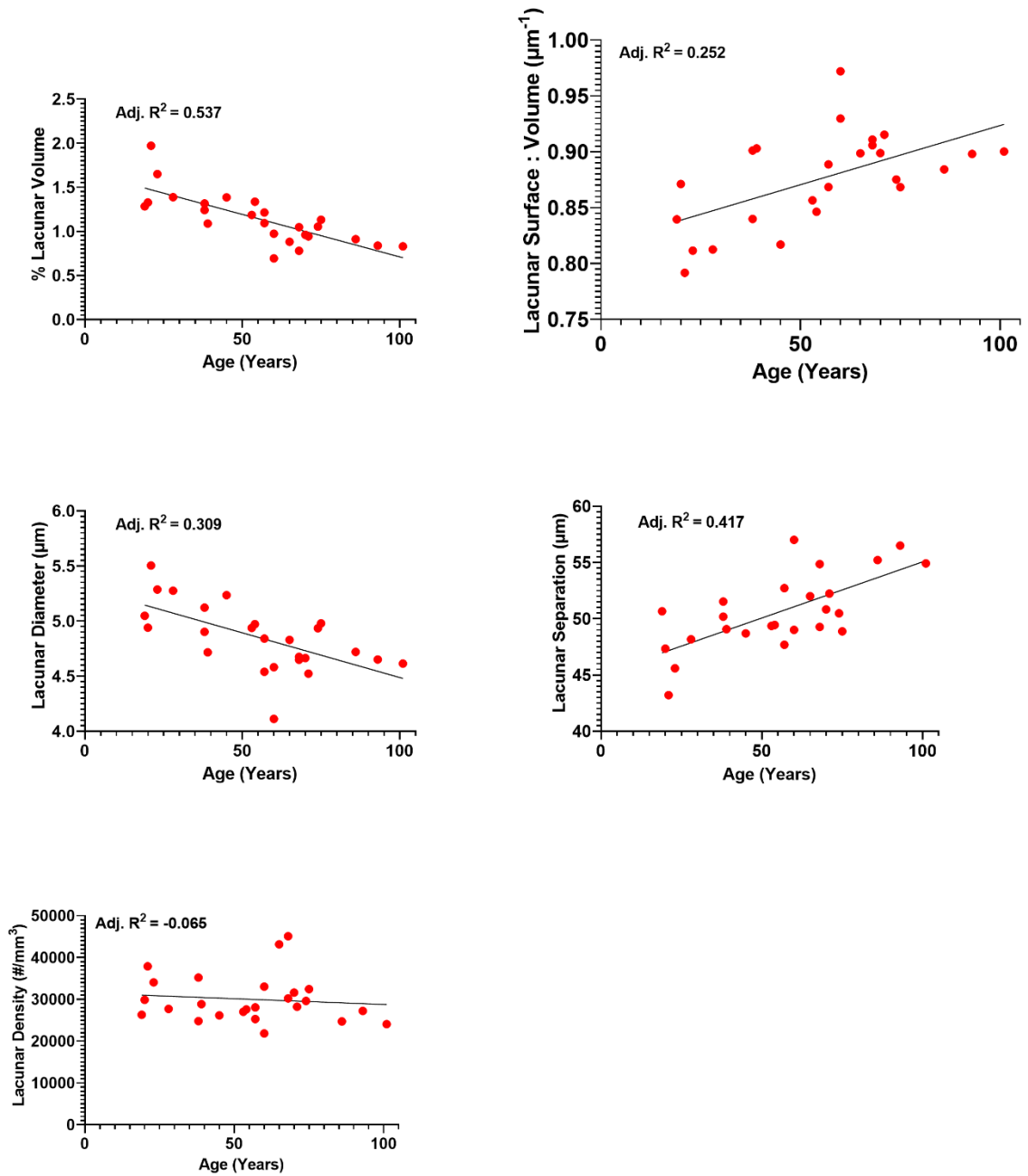


Figure 9. Regression analyses of SR μ CT lacunar histomorphometric variables. Adjusted R^2 is indicated at the top of each graph.

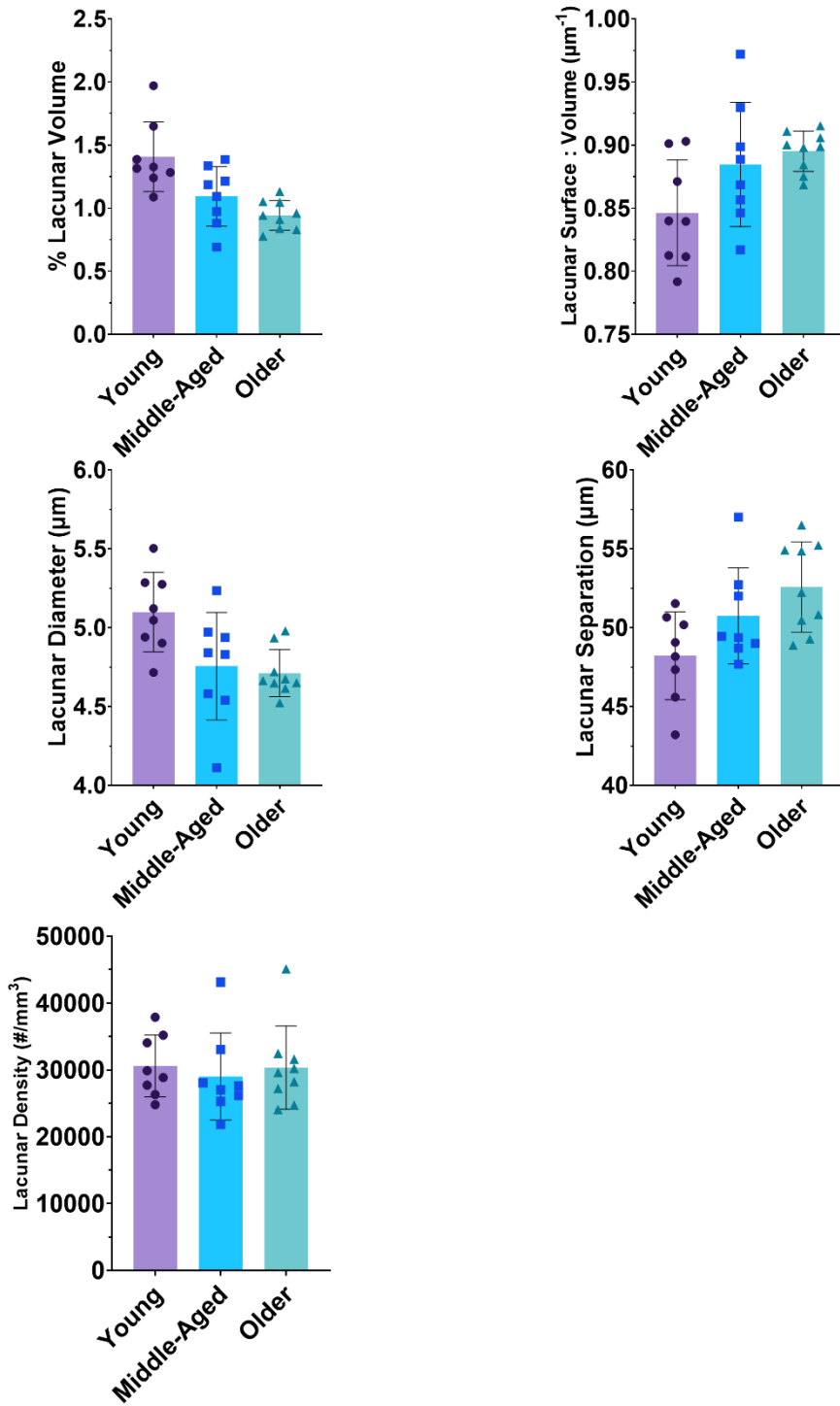


Figure 10. Factorial ANOVA results of SR μ CT lacunar histomorphometric variables.

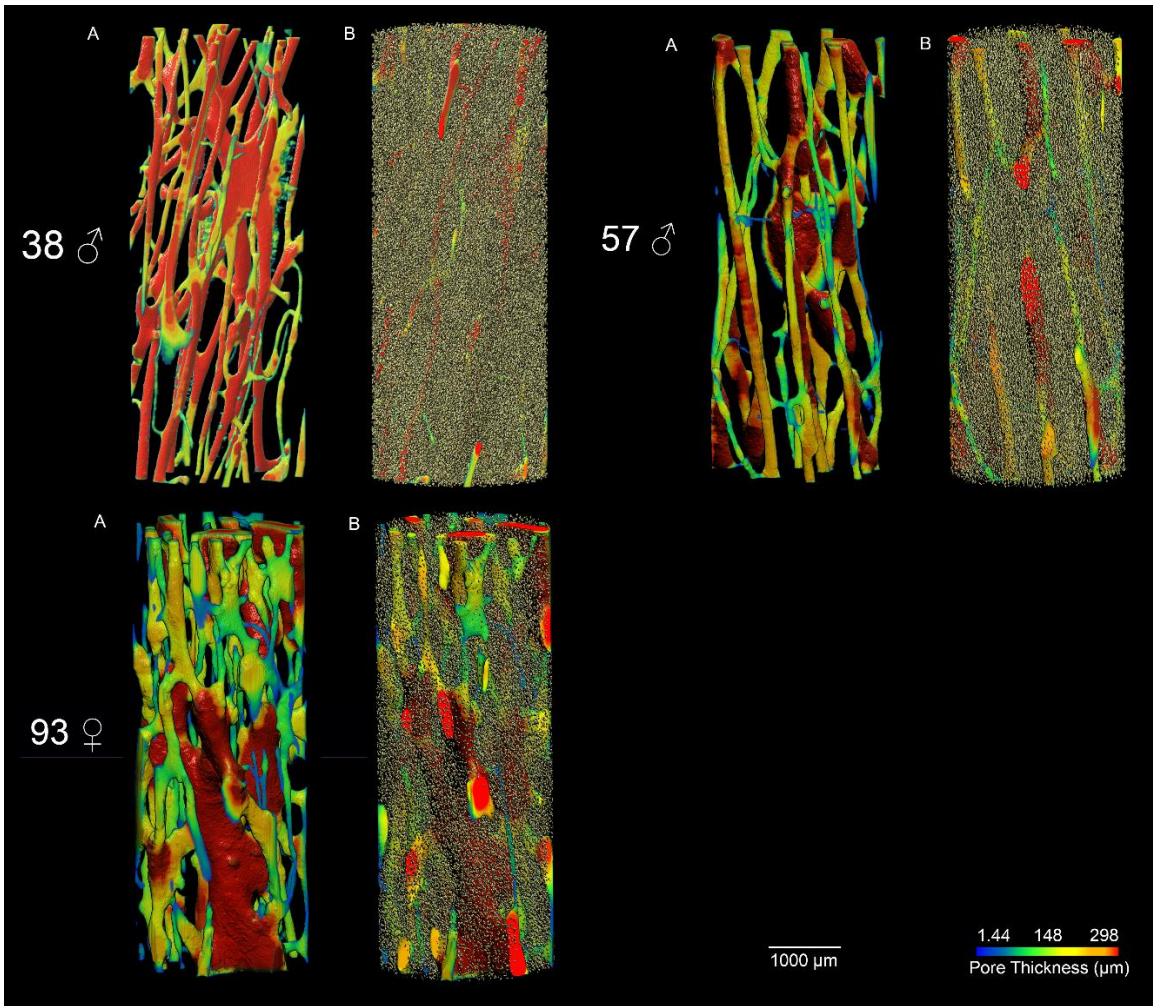


Figure 11. Representative 3D renders of SR μ CT pore and lacunar changes with age group. Panel A shows only vascular canals for each individual. Panel B includes osteocyte lacunae superimposed on vascular canals for each individual. Color scale bar is applied only to pore network, not lacunae.

CLSM

Regression analyses revealed neither chronological age, sex, nor the interaction between age and sex were significant predictors for any lacunar variable (Table 6, Figure 12). Factorial ANOVAs also revealed no significant differences in any lacunar variable for age group, sex, nor the interaction between age and sex (Table 7, Figure 13).

Regression analyses of canalicular variables further revealed no significant differences for chronological age, sex, or the interaction between age and sex (Table 6, Figure 14). Factorial ANOVAs indicated no significant differences in any canalicular variable for age, sex or the interaction between age and sex (Table 7, Figure 15). Representative 3D renders of lacunar and canalicular differences between age groups can be seen in Figure 16.

Table 6. Regression results for CLSM variables compared by chronological age and sex⁸¹⁻⁸³.

Morphometric Variable (Data Transformation)	Fixed Factor	F	p-value	ω^2	Observed Power
% Lacunar Volume (Log ₁₀)	Overall	2.270	0.110	0.015	49.30%
	Sex	0.354	0.558	-0.025	8.80%
	Age	2.434	0.134	0.057	31.90%
	Age*Sex	0.18	0.676	-0.032	6.90%
Lacunar Surface : Volume (No Transformation)	Overall	0.628	0.605	-0.046	15.90%
	Sex	0.096	0.759	-0.038	6.00%
	Age	1.489	0.236	-0.020	21.40%
	Age*Sex	0.000	0.988	-0.042	5.00%
Lacunar Diameter (No Transformation)	Overall	0.857	0.479	-0.018	20.40%
	Sex	1.005	0.328	0.000	16.00%
	Age	0.475	0.498	-0.021	10.10%
	Age*Sex	0.252	0.624	-0.031	7.60%
Lacunar Separation (Bootstrap)	Overall	1.494	0.245	0.056	33.60%
	Sex	0.060	0.808	-0.035	5.60%
	Age	0.066	0.799	-0.035	5.70%
	Age*Sex	0.231	0.636	-0.029	7.40%
Lacunar Density (No Transformation)	Overall	9.779	0.003	0.401	93.90%
	Sex	5.094	0.035	0.098	57.70%
	Age	12.880	0.002	0.285	92.80%
	Age*Sex	3.375	0.080	0.057	41.80%
% Canalicular Volume (Bootstrap)	Overall	5.017	0.009	0.325	85.50%
	Sex	3.848	0.063	0.077	46.50%
	Age	11.759	0.003	0.290	90.50%
	Age*Sex	3.501	0.075	0.068	43.10%
Canalicular Surface : Volume (No Transformation)	Overall	2.034	0.140	0.110	44.70%
	Sex	0.113	0.740	-0.032	6.20%
	Age	4.635	0.043	0.129	53.70%
	Age*Sex	1.000	0.329	0.000	15.90%
Canalicular Diameter (No Transformation)	Overall	1.907	0.159	0.098	42.10%
	Sex	0.088	0.770	-0.033	5.90%
	Age	1.776	0.197	0.028	24.60%
	Age*Sex	0.330	0.572	-0.024	8.50%
Canalicular Separation (Bootstrap)	Overall	4.428	0.015	0.291	80.40%
	Sex	3.462	0.077	0.070	42.70%
	Age	4.130	0.055	0.089	49.20%
	Age*Sex	1.096	0.307	0.003	17.00%
Canalicular Connectivity Density (No Transformation)	Overall	5.679	0.005	0.360	89.80%
	Sex	7.703	0.011	0.172	75.40%
	Age	11.110	0.003	0.259	88.80%
	Age*Sex	7.498	0.012	0.166	74.30%

Table 6 (Continued)

Canalicular Density (No Transformation)	Overall	9.077	0.007	0.146	52.20%
	Sex	0.161	0.692	-0.029	6.70%
	Age	0.589	0.451	-0.014	11.30%
	Age*Sex	0.197	0.662	-0.027	7.10%

Table 7. Factorial ANOVA results for CLSM variables compared by age group and sex.

Morphometric Variable (Data Transformation)	Fixed Factor	F	p-value	ω^2	Observed Power
% Lacunar Volume (Log ₁₀)	Overall	1.220	0.338	0.042	33.70%
	Sex	0.453	0.509	-0.023	9.80%
	Age Group	1.420	0.266	0.035	26.70%
	Age Group*Sex	0.136	0.874	-0.072	6.80%
Lacunar Surface : Volume (No Transformation)	Overall	0.503	0.770	-0.110	15.20%
	Sex	0.358	0.557	-0.029	8.80%
	Age Group	0.467	0.634	-0.047	11.50%
	Age Group*Sex	0.819	0.456	-0.016	16.90%
Lacunar Diameter (Bootstrap)	Overall	0.804	0.561	-0.041	22.70%
	Sex	1.830	0.192	0.035	25.00%
	Age Group	0.261	0.773	-0.062	8.50%
	Age Group*Sex	0.964	0.399	-0.003	19.20%
Lacunar Separation (Bootstrap)	Overall	1.314	0.300	0.059	36.20%
	Sex	3.399	0.081	0.090	41.70%
	Age Group	0.735	0.492	-0.020	15.60%
	Age Group*Sex	0.274	0.763	-0.055	8.70%
Lacunar Density (No Transformation)	Overall	2.157	0.102	0.188	57.50%
	Sex	3.327	0.084	0.076	41.00%
	Age Group	2.684	0.094	0.109	46.70%
	Age Group*Sex	0.538	0.592	-0.030	12.60%
% Canalicular Volume (Log ₁₀)	Overall	1.644	0.197	0.114	45.00%
	Sex	1.020	0.325	0.001	16.00%
	Age Group	1.943	0.171	0.068	35.20%
	Age Group*Sex	0.762	0.481	-0.017	16.00%
Canalicular Surface : Volume (Bootstrap)	Overall	1.629	0.200	0.112	44.60%
	Sex	1.912	0.098	0.032	25.90%
	Age Group	2.629	0.183	0.116	45.90%
	Age Group*Sex	0.792	0.467	-0.015	16.50%
Canalicular Diameter (Bootstrap)	Overall	1.517	0.231	0.094	41.70%
	Sex	4.508	0.047	0.127	52.20%
	Age Group	1.324	0.289	0.024	25.10%
	Age Group*Sex	0.603	0.557	-0.029	16.50%

Table 7 (Continued)

Canalicular Separation (No Transformation)	Overall	1.947	0.133	0.159	52.60%
	Sex	6.414	0.020	0.182	67.10%
	Age Group	0.598	0.560	-0.027	13.50%
	Age Group*Sex	0.500	0.05	-0.034	12.00%
Canalicular Connectivity Density (Bootstrap)	Overall	1.487	0.240	0.089	40.90%
	Sex	1.218	0.284	0.008	18.20%
	Age Group	1.343	0.285	0.025	25.40%
	Age Group*Sex	1.261	0.306	0.019	24.00%
Canalicular Density (No Transformation)	Overall	1.582	0.213	0.104	43.40%
	Sex	4.872	0.040	0.139	55.40%
	Age Group	0.783	0.471	-0.016	16.30%
	Age Group*Sex	0.100	0.905	-0.064	6.30%

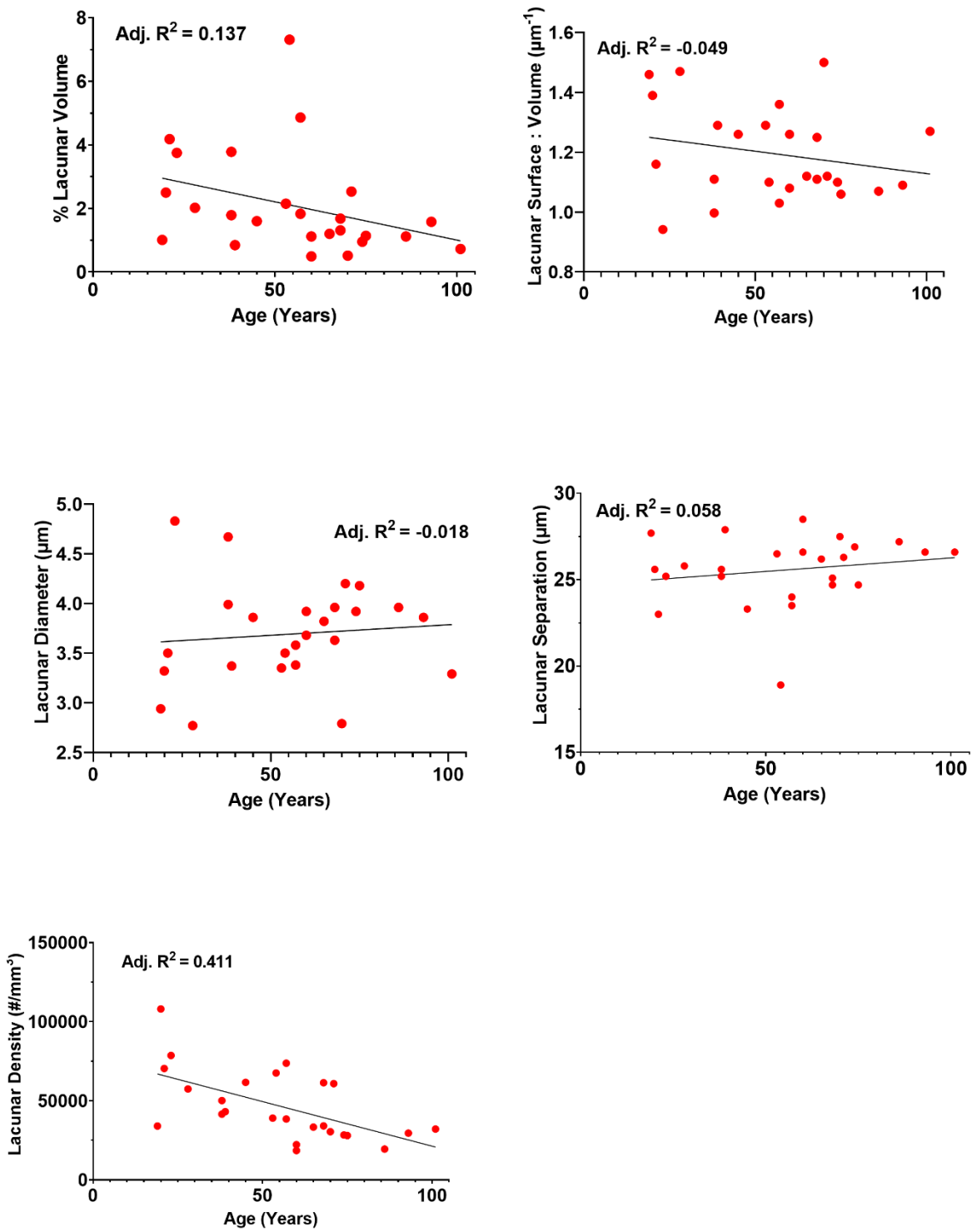


Figure 12. Regression analyses of CLSM lacunar histomorphometric variables. Adjusted R^2 is indicated at the top of each graph.

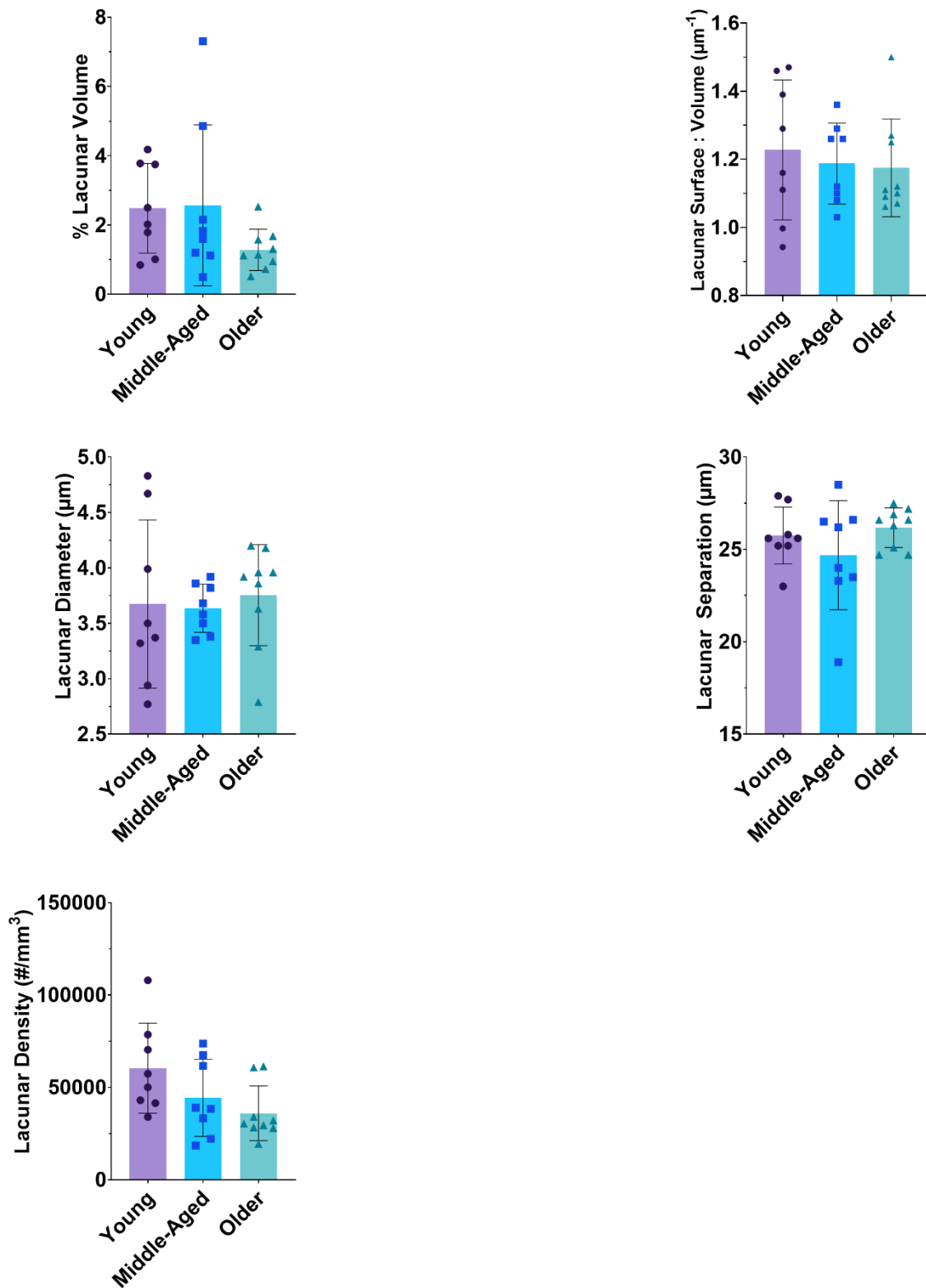


Figure 13. Factorial ANOVA results of CLSM lacunar histomorphometric variables.

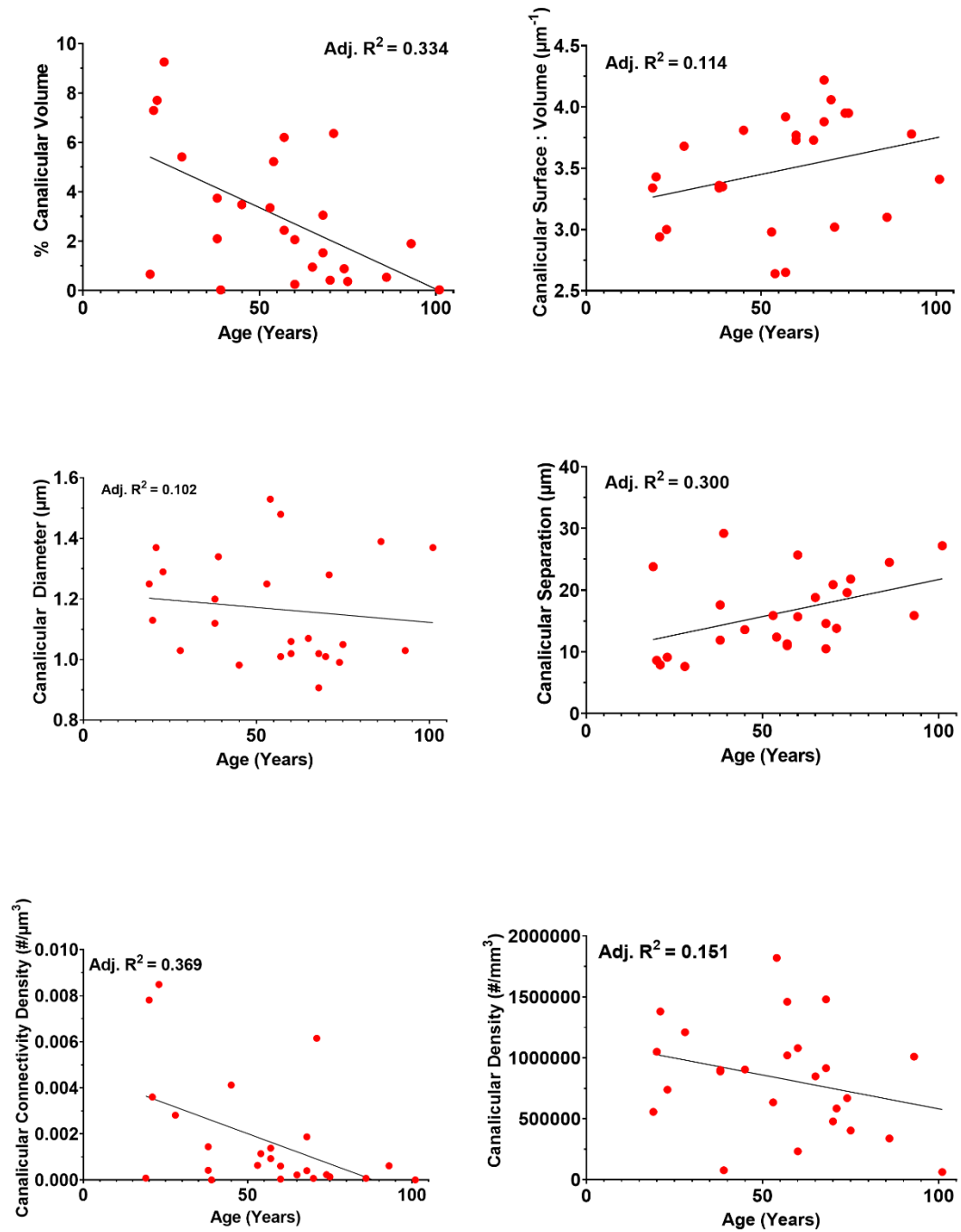


Figure 14. Regression analyses of CLSM canalicular histomorphometric variables. Adjusted R^2 is indicated at the top of each graph.

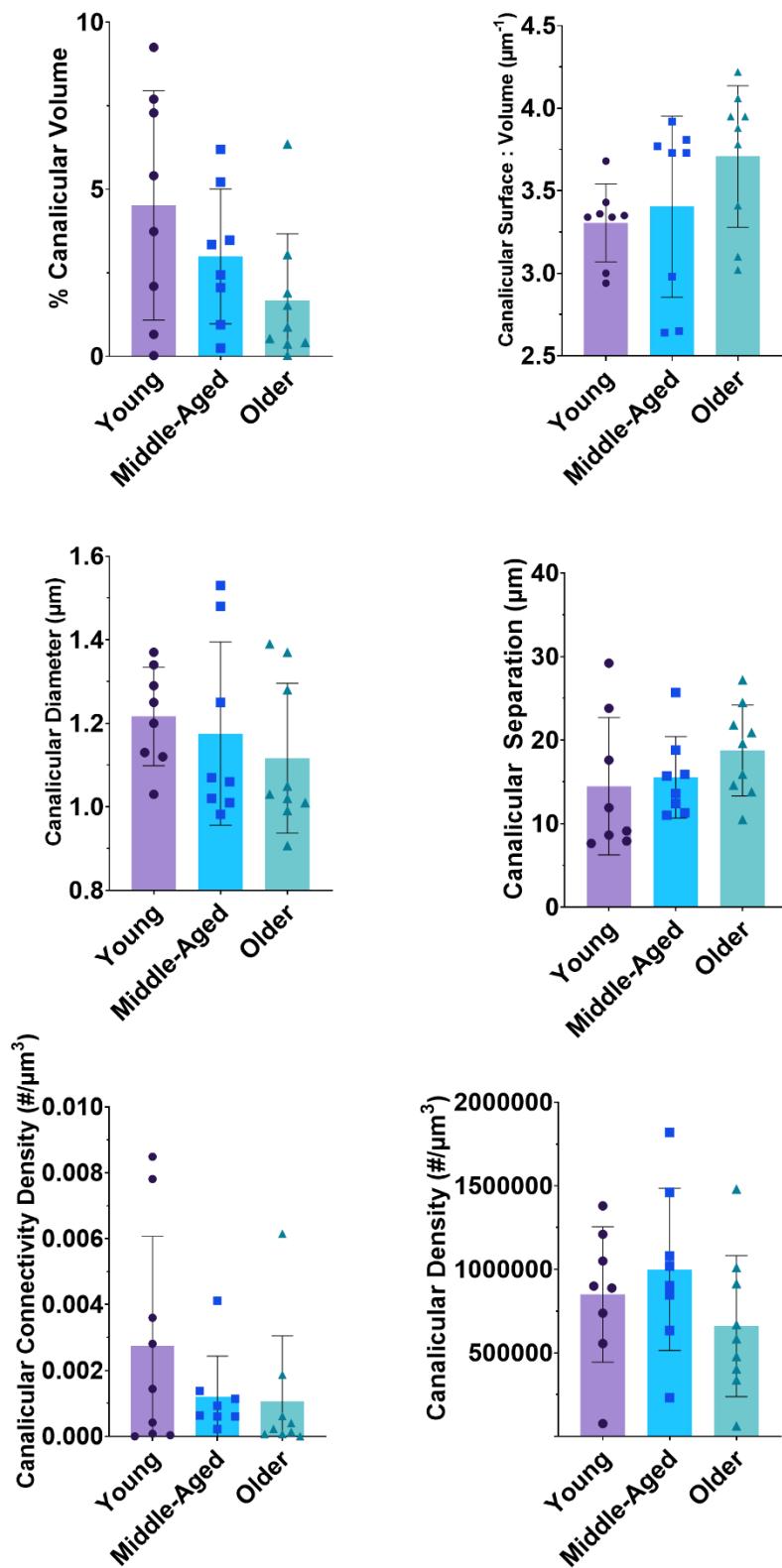


Figure 15. Factorial ANOVA results of CLSM canaliculi histomorphometric variables.

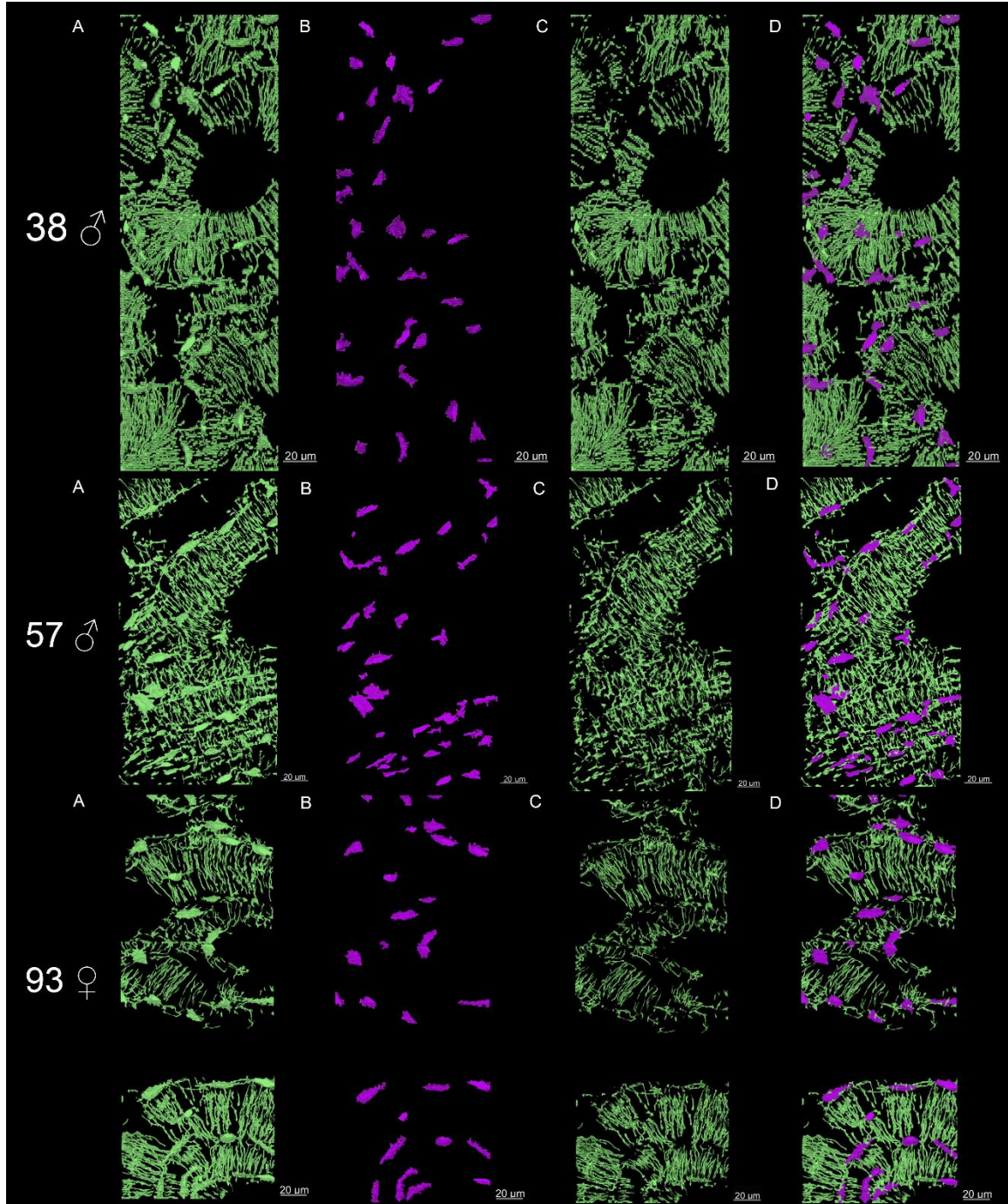


Figure 16. Representative 3D renders of CLSM lacunar and canaliculi changes with age group. Panel A shows imported CLSM dataset for each individual. The remaining panels for each individual indicate isolated lacunae (B), isolated canaliculi (C) and combined multi-ROI of lacunae and canaliculi (D). Scale bar is 20 μm.

Discussion

Vascular Pore Changes: SR μ CT

The SR μ CT results indicated decreasing Pore Surface : Volume, but increasing Pore Diameter with advancing age, suggesting an expansion and convergence of pores, resulting in fewer, larger pores, with advancing age. No significant age-associated change was found, however, in Pore Separation nor Pore Connectivity Density, which may be due to the small ROI limiting the observable region for pore interconnection/divergence. Previous studies have found similar results^{91-93,95}, suggesting pore size and number increase until age 50-60. A histological study of the anterior femoral midshaft by Bousson and colleagues⁹¹ determined both Pore Number and Volume increased until age 60 where Pore Number then decreased while Pore Volume continued to increase. Another histological study⁹³ found Pore Density increased with age, but declined after age 50. Studies utilizing 3D imaging have corroborated these findings in the anterior midshaft femur. Cooper and colleagues⁹² found chronological age to be associated with increased vascular porosity, diameter, connectivity, and decreased separation.

Sex was found to be non-significant for all examined variables. This differs from previous studies which found increased porosity and diameter in females relative to males^{91,92,96}. Bousson and colleagues⁹¹ found much of this variability to occur in the endosteal region of females which had fewer and larger pores relative to the other bone envelopes. We did not examine the endosteal region in this study, however, due to diagenetic changes and resulting oversaturation of stain.

Age-Associated Lacunar Changes: SR μ CT and CLSM

Our results from SR μ CT showed decreased lacunar volume fraction with advancing age, however this change was lost when dividing our sample in age groups. These seemingly contradictory findings between regression and ANOVA analyses are likely the result of too broad an age range in each age group, preventing us from capturing this decline with three age groups, similar to work by Carter and colleagues⁶⁷, where Lacunar Density declined significantly with advancing age, but this change was lost when separating their sample into two age groups (< 50, 50+ years old). Our CLSM results indicated no significant changes in any lacunar variable with age.

Age-associated changes in lacunar volume and diameter have been shown in SR μ CT studies of the proximal femur in females⁶⁷ and in the iliac crest⁹⁷. Previous 2D histological studies support these findings in the midshaft femur in both age group^{64,98} and chronological age^{66,70,99}. These changes in lacunar diameter and size are thought to be adaptations to changes in mechanosensitivity²⁸. Previous work suggests lacunar shrinkage occurs through hypermineralization of the extracellular space between the lacunar wall and osteocyte itself as a response to decreased strain with advancing age⁶⁷.

Sex-Associated Lacunar Changes: SR μ CT and CLSM

Neither our SR μ CT results nor our CLSM results revealed any significant changes in lacunar variables with sex. Previous 2D histological studies of the midshaft femur also report no significant changes in Lacunar Density between sexes^{66,70,98}. An SR μ CT study on the iliac crest further supports these findings, reporting no difference between sexes in 3D Lacunar Density nor Lacunar Volume⁶⁵. Estrogen deficiency has

been shown to induce osteocyte apoptosis in human¹⁰⁰ and murine models^{101,102} and in both cortical^{101,102} and trabecular^{100,102} bone. A previous histological study¹⁰³ of the iliac crest found Lacunar Density to decrease as early as the second decade of life, well before the effects of menopause and there was greater decline in density further from the periosteal surface. These lacunae would be closer to the neutral axis of the bone and, therefore, likely undergo less mechanical strain from loading than lacunae at the periphery¹⁰⁴.

Canalicular Changes: CLSM

Our regression analysis indicated neither age, sex, nor the interaction between age and sex were significant predictors of any canalicular variable. This is in contrast with previous work^{64,71,105}. These studies found decreased canalicular connectivity between young and older age groups^{64,71}. While our trends suggest our sample may be in agreement with previous work, we may have failed to see significance because our age categories are too broad, limiting our capacity to capture changes. Ashique and colleagues⁶⁴ divided their entirely female sample into age groups, however their young group spanned only three years (20-23) whereas their older group spanned 16 years (70-86). This uneven age range in groups may have inflated differences between young and older individuals. Milovanovic and colleagues⁷¹ had samples of 20-40 and 70-95 years old of unspecified sex. We therefore account for 30-50 years that were previously omitted and account for differences in sex.

Our ANOVA analysis, did not indicate any significant changes in canaliculi with age, however our data trend toward decreasing canalicular volume with advancing age. This trend appears qualitatively in the representative images shown in Figure 16.

Limitations and Future Directions

While our observed age-associated changes in 3D vascular canal morphometry were consistent with previous 2D histological^{91,93} and 3D μ CT studies⁹² of the midshaft femur, we found no significant changes between sexes. This may be due to multiple methodological factors. Our sample size ($n = 25$) was limited relative to the 79, 96, 163, or 168 donors used in previous studies^{91–93,96}. We further separated our sample into broad age categories based on broad life stages rather than decades⁹¹. Separating our sample by decade of life was not feasible as the limited sample size would have created decade groups with < 3 individuals, preventing statistical analysis. As stated above, it is possible the division of our sample into age groups may limit our ability to capture subtle age-related differences. Hunter and Agnew⁶⁶ used a similar sample size ($n = 30$) and found increased porosity with advancing age, but no significant differences resulting from sex. Future work employing a comparable SR μ CT method should determine whether these patterns can be replicated with a larger sample size.

Variation in our results from previous studies may stem from the amount of bone tissue analyzed. Our SR μ CT protocol utilized a small FOV (1.2 mm diameter) compared to previous μ CT (3 mm diameter)⁹², anatomical region radiograph⁹¹, or whole cross-section histology⁹³. While a smaller FOV may be less representative of overall morphometric differences, the majority of sex-related differences in midshaft femur

porosity are found in the anterior quadrant⁹⁶, the sampling site utilized for the current study. A smaller FOV was justified as each SR μ CT dataset comprised ~50 GB of data before reconstruction and 3D analysis of the entire reconstructed sample was not computationally feasible in a reasonable amount of time. The higher resolution of SR μ CT more accurately captures the finer details of pore morphometry. For example, vascular pore systems that bifurcate in 3D may appear as separate canals in 2D cross-section^{106,107}. A μ CT resolution study¹⁰⁸ found an increased voxel size (i.e., decreased resolution) from 5 to 10 μ m resulted in increased Pore Separation, Diameter, % Porosity and decreased Pore Surface : Volume, and Pore Number. It is possible that vascular pore morphometry, especially small pores, are better resolved at our smaller SR μ CT voxel size (1.44 μ m). Future work should apply our SR μ CT settings to other anatomical quadrants and other regions of the femur to determine if FOV or resolution is the source of deviation from previous histological and μ CT studies.

Differences in significance of Lacunar Volume between our CLSM and SR μ CT analyses may be the result of imaging limitations between each method. CLSM sections were taken adjacent to the section for SR μ CT imaging. Our SR μ CT results allowed us to visualize between 45,000 and 111,000 individual lacunae per sample compared to 14 to 112 using CLSM. This ~3 orders of magnitude difference likely means that SR μ CT provides a more complete picture of lacunar changes throughout life. Our CLSM data was further collected using anisotropic voxels (116.4 x 116.4 x 29.99 μ m). While we re-sampled each dataset to produce isotropic voxels (0.3 μ m) portions of each dataset with partial volumes could be distorted during resampling, resulting in distorted data during morphometric analysis. Our CLSM results may further be under-representative due to the

limitations of FITC specimen penetration and oversaturation of the periosteal and endosteal margins. This may be a contributing factor as to why we did not find significant changes with sex. Future work should ensure imaging of all three bone envelopes (periosteal, intracortical, endosteal) can be performed for a more representative sample as well as examining multiple sections throughout the femoral diaphysis to determine if LCN and pore morphometry vary intraskeletally. Future work might also examine these variables in non-weight-bearing bones (e.g., ribs) to determine how bearing weight may affect these results.

CHAPTER III

OPIOID-INDUCED TRABECULAR BONE CHANGES OF THE PROXIMAL TIBIA IN RABBITS VISUALIZED USING μ CT

Introduction

In 2020, 251 Americans died daily from a drug overdose. Opioids comprised 74.76%, of these deaths and fully synthetic opioids (e.g., fentanyl) were the most common opioid of abuse¹. Opioid misuse further costs an estimated \$78.5 billion per year in healthcare, criminal justice, and treatment costs¹⁰⁹. In the most recent survey, the five states with the highest incidence of opioid overdose deaths were West Virginia, Maryland, New Hampshire, Ohio, and Massachusetts¹¹⁰. This crisis shows no signs of slowing with opioid overdose deaths increasing more than 325% since 2010¹. Because of the increasing prevalence of opioid misuse, it is of utmost importance to examine the effects of prolonged opioid use on various aspects of health, including bone microstructure.

Opioids, and other pharmacologic agents including antidepressants and anticonvulsants, can dysregulate bone remodeling³². Briefly, remodeling is the mechanism through which organized groups of cells known as Basic Multicellular Units (BMUs) repair damage or replace aged packets of bone, known as Basic Structural Units (BSUs, secondary osteons), throughout life. Remodeling is organized into the six-phase ARF sequence and includes activation of osteoclasts, bone resorption by osteoclasts,

reversal from bone removal to bone formation, active bone formation by osteoblasts, mineralization of osteoid, and quiescence where the resulting BSU functions in mechanotransduction¹⁹. For thorough details regarding the remodeling process, see Chapter I.

Opioids accelerate bone loss directly through binding to opioid receptors on osteoblasts, limiting bone formation^{32,53,54}. While the specific mechanism by which opioids limit osteoblast function is not confirmed, one suspected mechanism is through opioids binding to the μ opioid receptor (MOP), initiating an inhibitory G protein cascade to stimulate release of potassium, inhibit calcium uptake, and inhibiting adenylyl cyclase resulting in decreased cyclic adenosine monophosphate (cAMP) production in the osteoblast and limiting osteocalcin secretion⁵³. This is similar to the opioid mechanism of action in neurons to produce analgesia⁴⁶. Opioids can also act indirectly along the hypothalamus-pituitary-gonadal/adrenal (HPG/HPA) axes to decrease serum levels of sex hormones (e.g., estrogen, testosterone, estradiol) and regulating hormones (e.g., gonadotropin-releasing hormone, luteinizing hormone, etc.)^{43,52,53}. Prolonged opioid use can further cause hypogonadism which affects up to 90% of patients on chronic opioid therapy and limits the therapeutic effects of opioid analgesics⁵². The direct binding of opioids to osteoblasts and hypogonadism mimic the effects of osteoporosis in individuals who use opioids^{54,111}. Opioids with increased MOP affinity have a more pronounced effect on the HPG axis⁵⁴. Estrogen serves many critical functions in bone maintenance including inhibiting osteoclast differentiation, regulating calcium metabolism in the intestine, kidney and parathyroid glands, and enhancing osteoblast and osteocyte responses to mechanical forces^{32,43}.

Opioid binding to osteoblasts causes inhibition of osteocalcin secretion, but no change in alkaline phosphatase, key hormones for bone formation^{53,111,112}. Disruption of bone remodeling through hormone dysregulation coupled with decreased bone mineral density increase the risk of fracture in individuals with prolonged opioid use^{51,57}. Previous studies^{54,55,57} suggest this increased fracture risk may be caused by central nervous system effects of opioids such as difficulty with balance and postural changes during the gait cycle.

Pedrazzoni and colleagues⁵⁶ have suggested that trabecular bone may be more susceptible to opioid-induced bone mineral density changes because remodeling is more active in trabecular bone than in cortical bone owing to increased surface to volume ratio^{6,73}. In cortical remodeling, the BMU removes a roughly cylindrical packet of bone and then deposits new bone in its place producing a secondary osteon. Trabecular remodeling, however, removes a semi-circular packet of bone from the trabecular surface and deposits new bone, producing a hemi-osteon^{9,19}. A previous study¹¹³ examined the effects of opioids in over 200 women and found decreased trabecular bone quality in opioid users as measured through bone mineral density obtained through quantitative ultrasound. More recent studies have further found fewer trabeculae and increased trabecular separation in the lumbar vertebrae of rabbits following spinal fusion and subsequent treatment with transdermal fentanyl patches¹¹⁴ and thinner trabeculae in rats treated with either morphine or fentanyl⁴³.

To better understand the effects of opioid use on bone quality, we must limit confounding factors by studying animals that remodel bone similarly to humans in a controlled setting. Previous studies examining bone remodeling have utilized common

murine models (i.e., rats and mice) which do not spontaneously remodel cortical bone¹¹⁵. Other studies¹¹⁶⁻¹¹⁸ have utilized larger animal models such as rabbits, sheep, pigs, and goats which better resemble human cortical bone remodeling¹¹⁹ due to the presence of secondary osteons. The work presented here is part of a larger project examining the effects of opioids on both cortical and trabecular bone remodeling processes. For this reason, we required the use of an animal with cortical remodeling similar to humans. Rabbits were selected as they are the smallest commonly used laboratory animal that met this requirement. To examine the effects of opioids on bone remodeling in a representative animal model, we examined the proximal epiphysis of the left tibiae of 21 rabbits using micro-Computed Tomography (μ CT) and compared common histomorphometric variables between experimental opioid and control groups. Here, we tested whether 1) opioid use results in a decrease in bone volume, and 2) opioid use causes trabeculae to thin compared to controls. We hypothesized that decreased bone volume and thinner trabeculae will be present in the opioid groups compared to controls.

Materials & Methods

Animals and Opioid Treatments

Twenty-one skeletally mature (6-month-old) male New Zealand White rabbits (*Oryctolagus cuniculus*) weighing between 2.3 and 3.0 kg (mean = 2.62 kg) were sourced from Covance Inc. (Denver, PA). Rabbits were housed in The University of Akron Research Vivarium (UARV) for the duration of the experiment (10 weeks) and split into two experimental groups (fentanyl, $n = 7$; morphine, $n = 7$) and two control groups (saline, $n = 3$; patch, $n = 4$). A power analysis was completed prior to experiments to

determine group sizes with seven animals providing the ability to detect a minimum 10% change between controls and experimental groups. These group sizes provided a balance between anticipated effect size and specific research logistics (e.g., availability of animal housing). These group sizes are further consistent with previous studies examining induced osteoporosis in cortical¹²⁰ and trabecular^{121,122} bone in rabbits. Attending veterinarians recommended the use of transdermal fentanyl patches in lieu of injectable fentanyl due to health and safety concerns. This required the separation of our controls into saline injection and transdermal sham patch sub-groups to limit any observable differences caused by drug administration route. All animal procedures were performed in accordance with the Animal Welfare Act¹²³ and approved by The University of Akron Animal Care and Use Committee (IACUC #: 18-11-12 ARC).

Rabbits were housed separately in stainless steel batteries with perforated plastic floors to allow interaction between the animals. Rabbits were fed 150 g/day of Harlan Teklad Global High Fiber Rabbit Diet (Envigo, Madison, WI) and had access to water *ad libitum* via cage bottles. Enrichment food (e.g., spinach, papaya tablets) were provided daily. Enrichment toys (e.g., jingle balls, rattles) were left in each rabbit battery and changed weekly. Thrice weekly, all rabbits were placed in individual pens for 45 minutes to exercise and stretch. The exercise pens were made of metal caging wire coated in plastic to allow for interaction between rabbits. The housing room in the UARV was kept on a 12/12-hour light/dark cycle, with a local radio station playing during daylight hours for enrichment, and maintained at 16-21°C, and 30-70% humidity. Temperature and humidity were monitored using a Room Alert 12E system (AVTECH Software Inc., Warren, RI) installed in the room.

Experimental treatments began after a two-week acclimation period in the UARV and continued for eight weeks. Rabbits were weighed weekly and weight-based drug doses were adjusted accordingly. Morphine rabbits were administered 3 mg/kg/day of morphine sulfate via subcutaneous injection in the interscapular region. Saline control animals were administered 3 mg/kg/day of 0.9% NaCl saline. Fentanyl rabbits received one 25 µg/hour slow-release transdermal fentanyl patch (Henry Schein Inc., Melville, NY) every three days. Patches were placed in the interscapular region after shaving the fur and securing the patch with transparent film dressing (3M, St. Paul, MN) to ensure patch adhesion and adequate drug delivery. To further prevent the rabbits from chewing and ingesting the patches, the animals were placed in mesh telemetry jackets (Lomir Biomedical, Malone, NY). Patch control rabbits were treated with a topical 2% isopropyl myristate aqueous solution, a skin softening agent found in the fentanyl patches, on the interscapular region before application of the transparent film dressing and mesh jacket. This dilution was determined through previous safety assessments of such topical solutions¹²⁴. Opioid doses were based on previous studies^{114,125} and clinical recommendations for rabbit analgesia from UARV consulting veterinarians. After eight weeks of treatments, the animals were sacrificed via intraperitoneal injection of 125 mg/kg of pentobarbital sodium (Fatal-Plus, VorTech Pharmaceuticals, Dearborn MI). A bilateral thoracotomy was performed as a secondary means of euthanasia. Animals were immediately dissected following euthanasia to excise the left tibia. Adhering soft tissues were removed with dental tools. The tibiae were individually wrapped in 0.9% NaCl saline-soaked gauze and kept frozen at -20°C until imaging.

Ex vivo μ CT Imaging and Analysis

Three-dimensional (3D) imaging of rabbit proximal tibia (Figure 17) was accomplished using a SkyScan 1172 μ CT system (Bruker, Kontich, Belgium) housed at The University of Akron's National Polymer Innovation Center. Clay markers were placed on the anterior and medial aspects of the tibia for anatomical orientation of the μ CT datasets during reconstruction. The proximal epiphysis of each specimen was mounted to a brass peg using dental wax and secured with parafilm to prevent movement.

Settings for μ CT imaging were modified from a previous study of rabbit tibiae¹²⁶ and are included in Table 8. Datasets, comprised of 973 projections spanning a height of 13.71 mm, were reconstructed using NRecon v1.6.10.2 (Bruker), correcting for ring artifacts and beam hardening. We simultaneously isolated the tibia from fibula and trabecular bone from the outer cortical shell in CTAnalyser v.1.18.4.0 (Bruker) using a modified macro based on the manufacturer's instructions (Bruker Method Note MCT-124)¹²⁷. A brief explanation of the specific settings used to isolate the trabecular envelope is detailed in Appendix D. A 3D render of one such isolated trabecular envelope can be seen in Figure 18. Datasets were further separated into anatomical quadrants (anterior, posterior, medial, lateral) based on the ROI centroid using FIJI⁸⁰ (Appendix E) to determine if regional differences in histomorphometry exist (Figure 19). Histomorphometric data of the trabecular bone were acquired using CTAnalyser and included % Bone Volume, Bone Surface : Volume ratio, Trabecular Thickness, Trabecular Separation, and Trabecular Number. Descriptions of these variables can be found in Table 9.

Table 8. μ CT system settings applied to each scan.

Source voltage	74 kV
Source current	133 μ A
Pixel size	10.98 μ m
Rotation step	0.20°
Total specimen rotation	180°
Frame averaging	4 frames
Filters used	0.5 mm Aluminum
Ring artifact correction	10
Beam hardening correction	30%
Total number of projections	973



Figure 17. Scout scan of a micro-computed tomography dataset of the proximal tibia. Proximal end is superior. Dental wax securing the tibia to the mounting peg can be seen in light grey (radiolucent) throughout the top of the image. Scale bar is 2000 μ m.

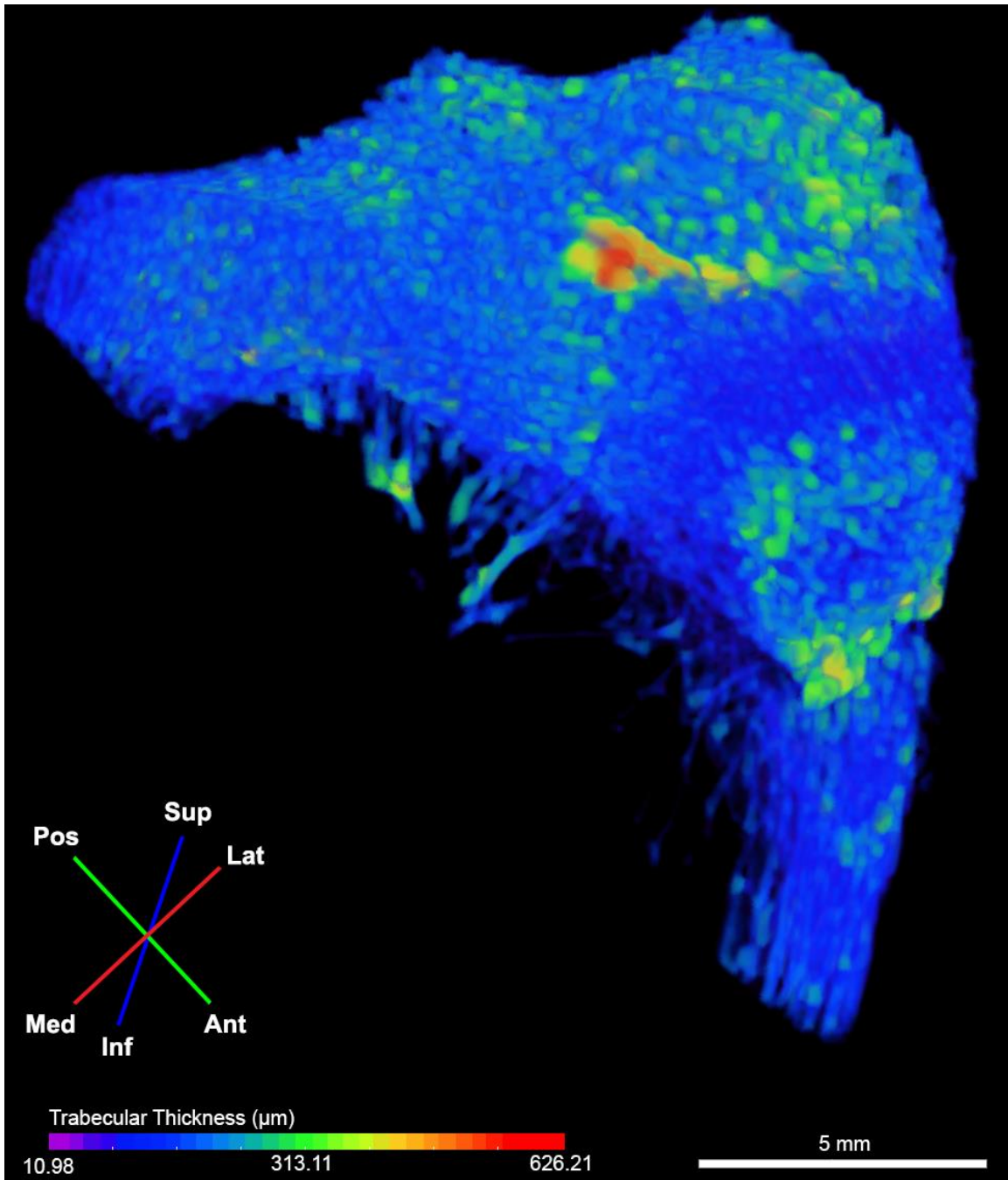


Figure 18. Representative 3D render of trabecular bone envelope in the proximal left tibia of a morphine group rabbit. Scale bar represents 5 mm.

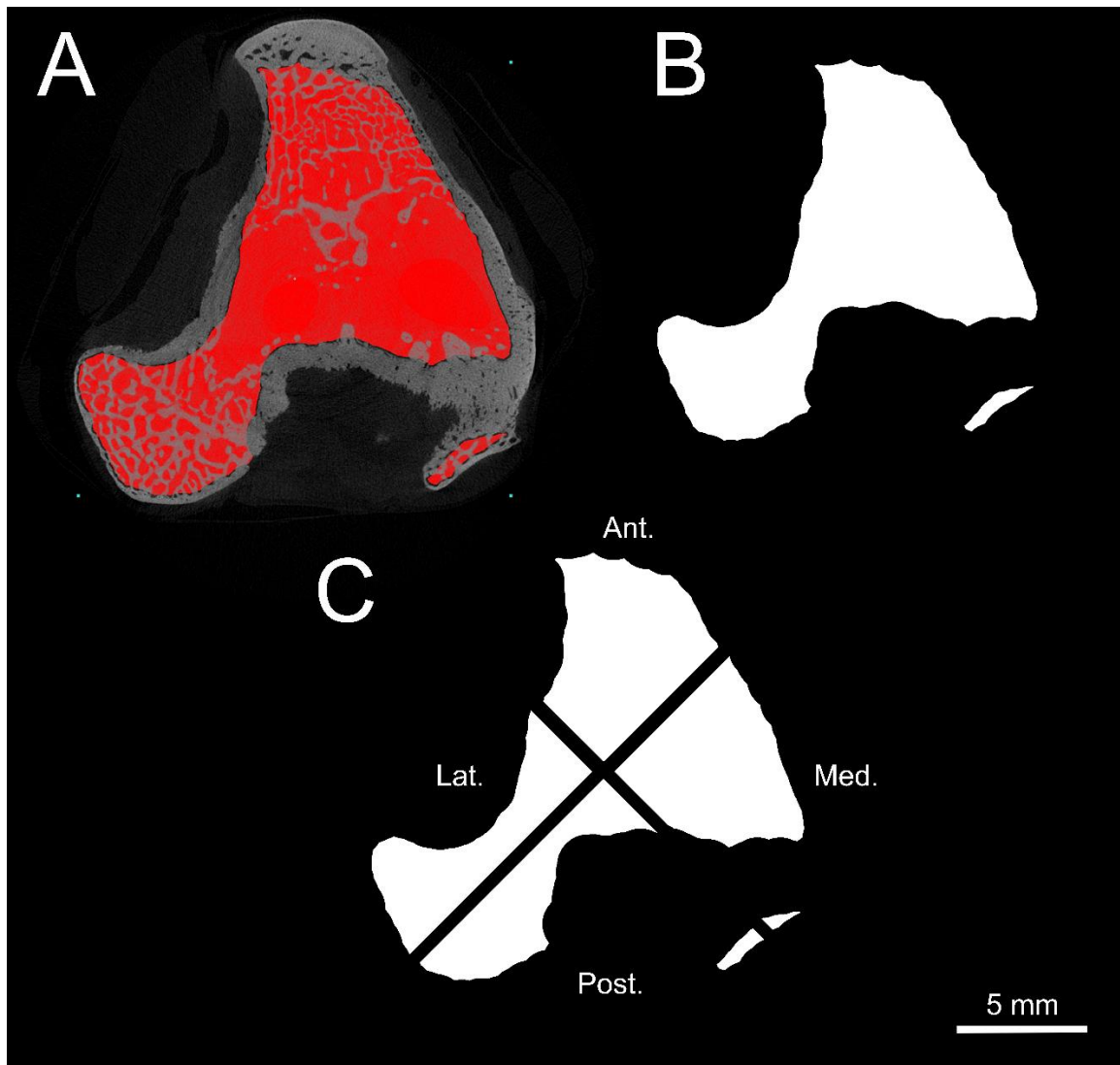


Figure 19. Superior view of the proximal tibia from a fentanyl group rabbit (A) demonstrating isolation of trabecular bone and epiphyseal line (red) from cortical bone (grey) utilizing CTAnalyser, described in Appendix D. Region of Interest (ROI) created from medullary cavity isolation of the proximal tibial epiphysis (B). Individual ROIs created for each anatomical quadrant using a custom macro in FIJI⁸⁰ described in Appendix E (C).

Table 9. Description of morphometric variables.

Variable Name	Abbr.	Description
% Bone Volume	% BV	Bone Volume / Tissue Volume
Bone Surface : Volume	BS/BV	Bone Surface / Bone Volume
Trabecular Thickness	Tb.Th	Diameter of largest sphere fit within a trabecula
Trabecular Separation	Tb.Sp	Diameter of largest sphere fit between trabeculae
Trabecular Number	Tb.N	(Bone Volume / Tissue Volume) / Trabecular Thickness

Statistical Analysis

All statistical analyses were accomplished using SPSS v26 (IBM, Armonk, NY). Individual two-way ANOVAs with step-down Bonferroni corrections (Appendix C) were performed using drug administered (fentanyl vs. sham patch, morphine vs. saline control) and anatomical region (anterior, posterior, medial, lateral) as independent variables. Separate analyses were warranted due to the differing pharmacokinetics of fentanyl and morphine^{128,129}, including opioid receptor binding¹³⁰, and different drug administration routes utilized in the current study. Each ANOVA was followed by a Tukey HSD post-hoc test to determine which anatomical quadrants differed¹³¹. Residuals were tested for normality and homogeneity of variance assumptions using Shapiro-Wilk and Levene's tests, respectively^{84,85}. Any variables that violated these assumptions were log₁₀-transformed and re-analyzed. If the variable continued to violate assumptions, it was re-analyzed using a two-way ANOVA with a bootstrapped^{88,89} sample created from 1000 replicates.

Rabbit weights at Week 0 and Week 8 were analyzed using a Wilcoxon Signed-Rank test as the data violated normality and homogeneity of variance assumptions and could not be corrected with data transformation, preventing the use of a two-tailed paired *t*-test. To determine if there was a difference in weight by drug group, we compared Week 8 weight using two separate Student's *t*-tests (morphine vs. saline, fentanyl vs. sham). Normality and homogeneity of variance were confirmed with Shapiro-Wilk and Levene's test, respectively. If data violated either assumption, they were log₁₀-transformed. If after transformation assumptions remained violated, we utilized a Mann-Whitney U test.

Results

Rabbit Weight

A Wilcoxon Signed-Rank test indicated a significant difference in rabbit weight between the start and end of the experimental period ($Z = -3.841, p < 0.001$), with an average increase of 0.40 kg. A two-tailed Student's t-test indicated no significant difference in Week 8 weight between morphine and saline animals ($t[7] = -1.241, p = 0.250$). A Mann-Whitney U test indicated no significant difference in Week 8 weight between fentanyl and sham animals ($U = 5.500, p = 0.103$). Our previous behavioral study on these animals indicated food consumption was decreased in morphine animals compared to control animals via one-way ANCOVA¹³². Food consumption was further not affected by placing the fentanyl and sham animals in telemetry jackets. Opioid-treated animals showed no significant difference in fecal output compared to controls as measured on a 1-3 scale and compared using one-way ANCOVA. There was further no significant difference in fecal output between jacketed and non-jacketed animals¹³².

Morphine & Saline

Morphine animals had significantly greater % Bone Volume ($F[1,32] = 15.880, p < 0.001$) than saline controls. No other morphometric variables were significantly different between morphine and saline controls resulting from drug group. A summary of these results can be found in Figure 20 and Table 10.

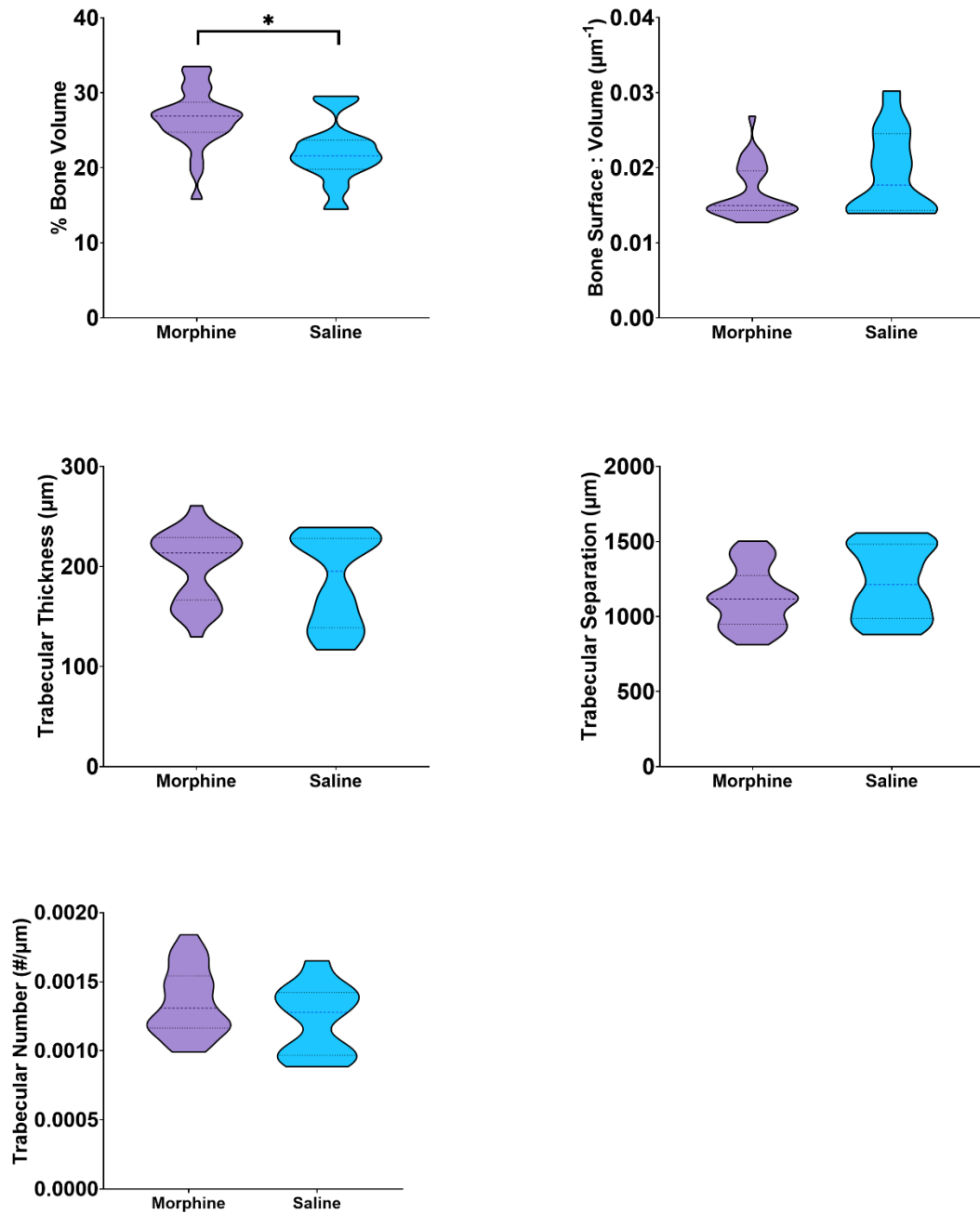


Figure 20. Comparison of histomorphometric variables between morphine and saline animals. Asterisks indicate a significant difference between morphine and saline ($p < 0.005$). Dashed line indicates median, dotted lines indicate 1st and 3rd quartiles. Plots are truncated at the limits of data distribution.

Table 10. Two-Way ANOVA results for histomorphometric variables by drug group (morphine or saline) and anatomical region. Bonferroni-corrected $\alpha = 0.005$.

Morphometric Variable (Data Transformation)	Fixed Factor	F	p-value	ω^2	Effect Size*
% Bone Volume (Bootstrap)	Overall	5.676	< 0.001	0.450	Large
	Drug	15.880	< 0.001	0.205	Large
	Region	6.884	0.001	0.243	Large
	Drug*Region	0.217	0.884	-0.032	-
Bone Surface : Volume (Bootstrap)	Overall	4.231	0.002	-0.112	-
	Drug	4.450	0.041	0.057	-
	Region	6.613	0.001	0.269	Large
	Drug*Region	0.047	0.986	-0.046	-
Trabecular Thickness (Bootstrap)	Overall	3.751	0.004	0.325	Large
	Drug	1.795	0.190	0.013	-
	Region	6.017	0.002	0.254	Large
	Drug*Region	0.167	0.918	-0.042	-
Trabecular Separation (No Transformation)	Overall	12.789	< 0.001	0.674	Large
	Drug	5.682	0.023	0.038	-
	Region	24.012	< 0.001	0.563	Large
	Drug*Region	0.070	0.975	-0.023	-
Trabecular Number (No Transformation)	Overall	10.323	< 0.001	0.620	Large
	Drug	0.980	0.022	0.045	-
	Region	8.895	< 0.001	0.492	Large
	Drug*Region	0.196	0.838	-0.020	-

*Effect size is determined from Cohen's⁹⁴ f modified for ω^2 as Small Effect > 0.0099, Medium Effect > 0.0599, and Large Effect > 0.1499.

All examined variables showed significant differences between anatomical quadrants (Figure 21, Table 11). % Bone Volume ($F[3,32] = 6.884$, $p = 0.001$) revealed significantly more volume in the lateral quadrant relative to the anterior ($p = 0.004$) and posterior ($p = 0.001$) quadrants. Bone Surface : Volume ($F[3,32] = 6.613$, $p = 0.001$) was significantly greater in the anterior quadrant than either lateral ($p = 0.003$) or medial ($p < 0.001$) quadrants. Trabecular Thickness ($F[3,32] = 6.017$, $p = 0.002$) was significantly less in the anterior quadrant than medial ($p < 0.001$) or posterior ($p = 0.004$) quadrants. Trabecular Separation ($F[3,32] = 24.012$, $p < 0.001$) was significantly greater in the posterior quadrant than either the anterior ($p < 0.001$), lateral ($p < 0.001$), or medial ($p =$

0.001) quadrants. The medial quadrant also had significantly greater Trabecular Separation than the lateral quadrant ($p = 0.001$). Trabecular Number ($F[3,32] = 8.895, p = <0.001$) was significantly higher in the anterior quadrant than either medial or posterior quadrants ($p < 0.001$ for each quadrant). The lateral quadrant also had significantly higher Trabecular Number than either the medial or posterior quadrants ($p < 0.001$ for each quadrant). There were no significant differences in the interaction between drug and anatomical quadrant in any examined variable.

Table 11. Tukey HSD post-hoc results for region-significant μ CT variables in morphine and saline animals. Bonferroni-corrected $\alpha = 0.005$.

Morphometric Variable	Anatomical Quadrants	<i>p-value</i>
% Bone Volume	Anterior – Posterior	0.902
	Anterior – Lateral	0.004
	Anterior – Medial	0.952
	Posterior – Lateral	0.001
	Posterior – Medial	0.625
	Medial – Lateral	0.015
Bone Surface : Volume	Anterior – Posterior	0.006
	Anterior – Lateral	0.003
	Anterior – Medial	<0.001
	Posterior – Lateral	0.994
	Posterior – Medial	0.765
	Medial – Lateral	0.888
Trabecular Thickness	Anterior – Posterior	0.004
	Anterior – Lateral	0.012
	Anterior – Medial	<0.001
	Posterior – Lateral	0.972
	Posterior – Medial	0.856
	Medial – Lateral	0.612
Trabecular Separation	Anterior – Posterior	<0.001
	Anterior – Lateral	0.249
	Anterior – Medial	0.102
	Posterior – Lateral	<0.001
	Posterior – Medial	0.001
	Medial – Lateral	0.001
Trabecular Number	Anterior – Posterior	<0.001
	Anterior – Lateral	0.760
	Anterior – Medial	<0.001
	Posterior – Lateral	<0.001
	Posterior – Medial	0.948
	Medial – Lateral	<0.001

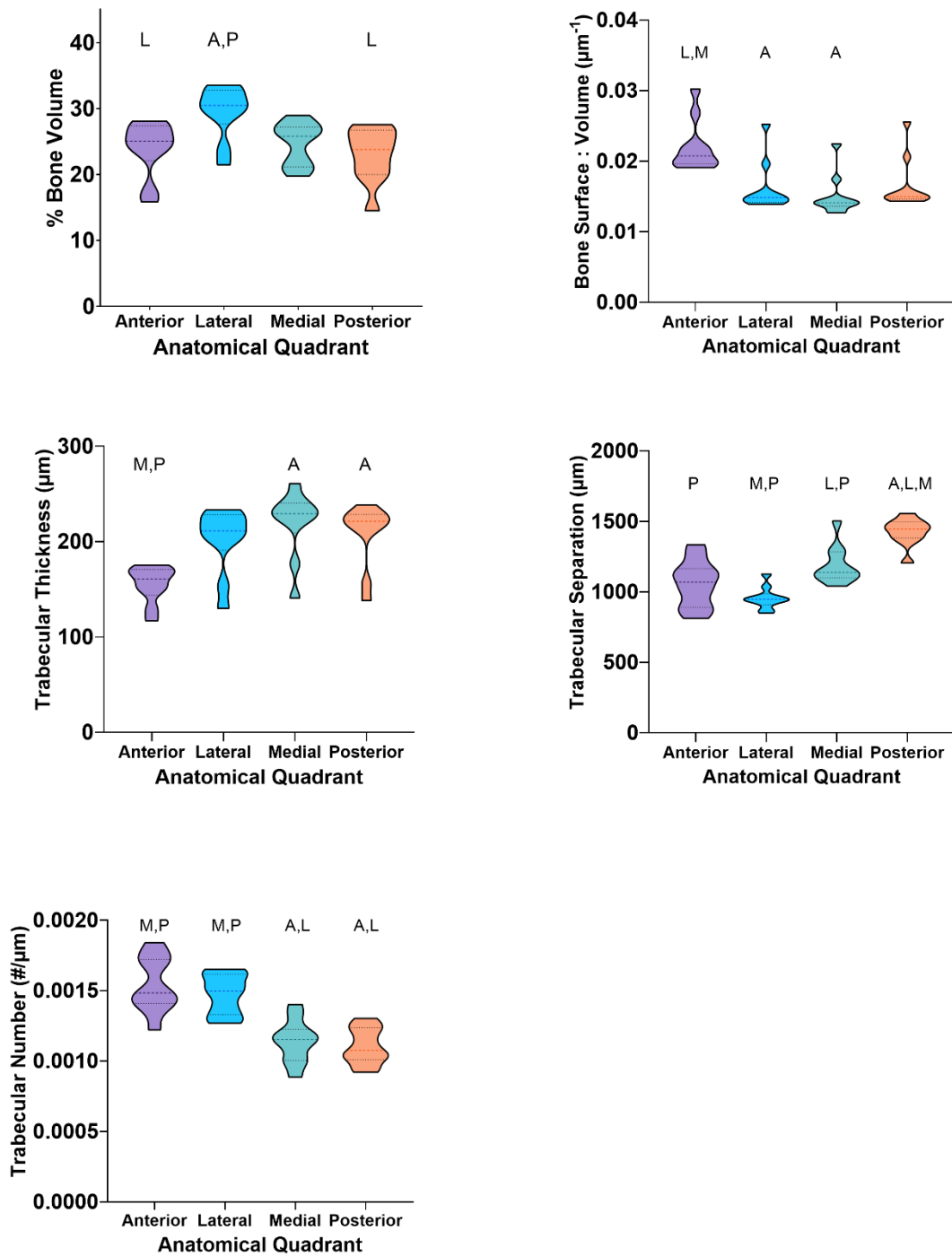


Figure 21. Comparison of histomorphometric variables by anatomical quadrant in morphine and saline animals. Letters above a bar indicate a significant difference ($p < 0.005$) between the anatomical quadrant beneath the letter(s) and the quadrant indicated by the letter(s) where Anterior = A, Lateral = L, Medial = M, and Posterior = P. Dashed line indicates median, dotted lines indicate 1st and 3rd quartiles. Plots are truncated at the limits of data distribution.

Fentanyl & Sham Patch

Fentanyl animals had significantly greater Trabecular Thickness ($F[1,36] = 9.851$, $p = 0.003$) than their control counterparts. In contrast, fentanyl animals had significantly less Trabecular Number ($F[1,36] = 9.878$, $p = 0.003$). Of the measured variables, % Bone Volume ($F[1,36] = 0.557$, $p = 0.460$) Bone Surface : Volume ($F[1,36] = 8.253$, $p = 0.007$), and Trabecular Separation ($F[1,36] = 5.835$, $p = 0.021$) were non-significant between fentanyl and patch animals. A summary of these results can be found in Figure 22 and Table 12.

Table 12. Two-Way ANOVA results for histomorphometric variables by drug group (fentanyl or sham patch) and anatomical region. Bonferroni-corrected $\alpha = 0.005$.

Morphometric Variable (Data Transformation)	Fixed Factor	F	p-value	ω^2	Effect Size*
% Bone Volume (Log ₁₀)	Overall	1.925	0.094	0.128	-
	Drug	0.557	0.460	-0.009	-
	Region	3.972	0.015	0.177	-
	Drug*Region	0.111	0.953	-0.053	-
Bone Surface : Volume (Log ₁₀)	Overall	23.021	< 0.001	0.777	Large
	Drug	8.253	0.007	0.037	-
	Region	44.924	< 0.001	0.665	Large
	Drug*Region	0.354	0.787	-0.010	-
Trabecular Thickness (No Transformation)	Overall	24.022	< 0.001	0.786	Large
	Drug	9.851	0.003	0.043	Small
	Region	46.427	< 0.001	0.664	Large
	Drug*Region	0.354	0.786	-0.009	-
Trabecular Separation (Bootstrap)	Overall	4.257	0.002	0.341	Large
	Drug	5.835	0.021	0.072	-
	Region	7.739	< 0.001	0.303	Large
	Drug*Region	0.294	0.829	-0.032	-
Trabecular Number (No Transformation)	Overall	16.882	< 0.001	0.716	Large
	Drug	9.878	0.003	0.057	Small
	Region	34.550	< 0.001	0.649	Large
	Drug*Region	0.209	0.890	-0.015	-

*Effect size is determined from Cohen's⁹⁴ f modified for ω^2 as Small Effect > 0.0099, Medium Effect > 0.0599, and Large Effect > 0.1499.

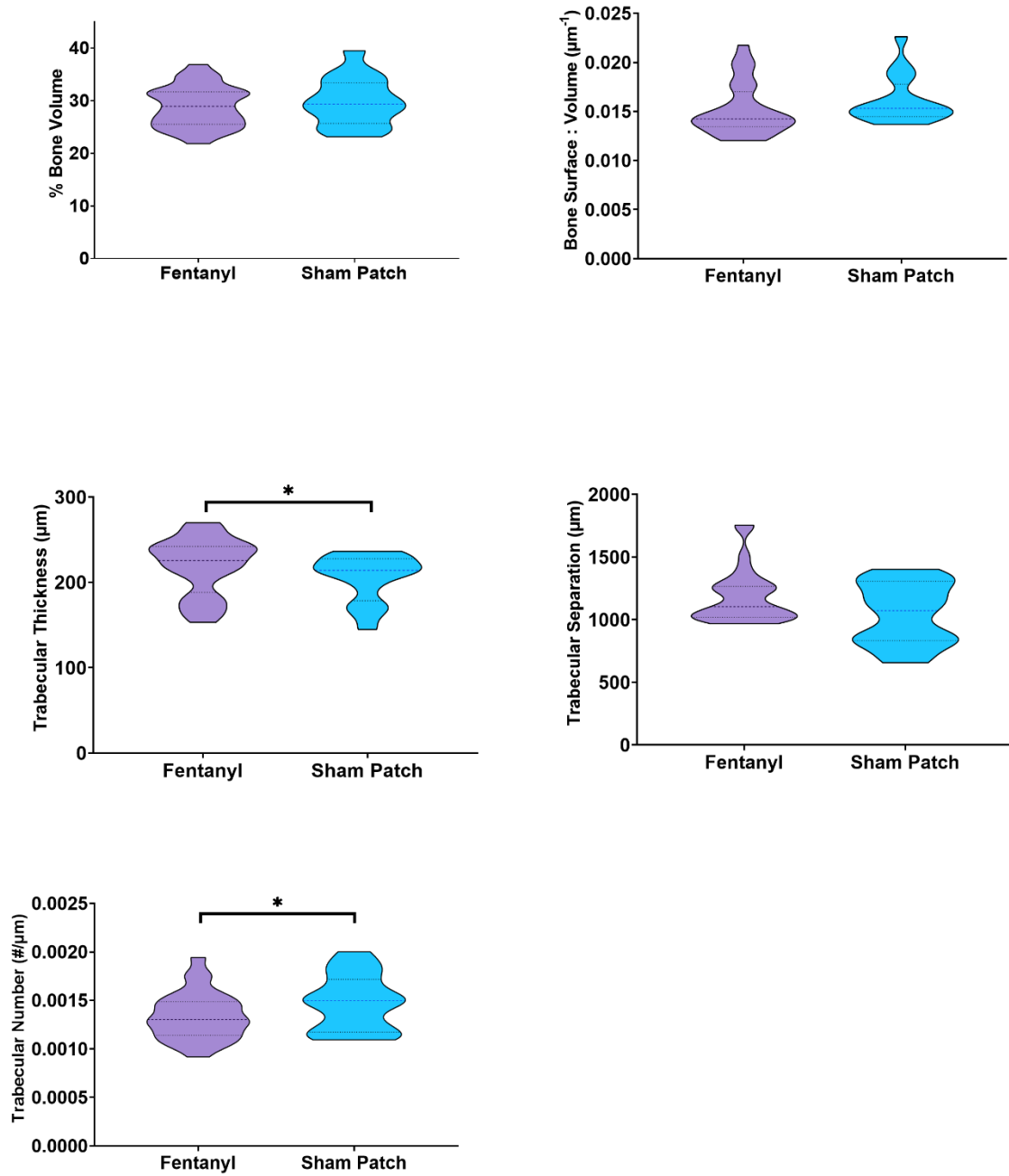


Figure 22. Comparison of histomorphometric variables between fentanyl and sham animals. Asterisks indicate a significant difference between morphine and saline ($p < 0.005$). Dashed line indicates median, dotted lines indicate 1st and 3rd quartiles. Plots are truncated at the limits of data distribution.

All examined variables showed significant differences between anatomical quadrants except % Bone Volume ($F[3,36] = 3.972, p = 0.015$) (Figure 23, Table 13). Bone Surface : Volume ($F[3,36] = 44.924, p < 0.001$) was significantly greater in the anterior quadrant than either lateral, medial, or posterior quadrants ($p < 0.001$ for each). Trabecular Thickness ($F[3,36] = 46.427, p < 0.001$) was consequently significantly less in the anterior quadrant than any of the other three quadrants ($p < 0.001$ for each). Trabecular Separation ($F[3,36] = 26.596, p < 0.001$) was significantly greater in the posterior quadrant than the lateral ($p < 0.001$) quadrant. Trabecular Number ($F[3,36] = 34.550, p < 0.001$) was significantly higher in the anterior quadrant than either lateral ($p = 0.003$), medial ($p < 0.001$), or posterior ($p < 0.001$) quadrants. The lateral quadrant further had significantly greater Trabecular Number than either medial ($p = 0.001$) or posterior ($p < 0.001$) quadrants. There were no significant differences due to the interaction between drug and anatomical quadrant in any examined variable.

Table 13. Tukey HSD post-hoc results for region-significant μ CT variables in fentanyl and sham patch animals. Bonferroni-corrected $\alpha = 0.005$.

Morphometric Variable	Anatomical Quadrants	<i>p-value</i>
Bone Surface : Volume	Anterior – Posterior	<0.001
	Anterior – Lateral	<0.001
	Anterior – Medial	<0.001
	Posterior – Lateral	1.000
	Posterior – Medial	0.359
	Medial – Lateral	0.412
Trabecular Thickness	Anterior – Posterior	<0.001
	Anterior – Lateral	<0.001
	Anterior – Medial	<0.001
	Posterior – Lateral	0.232
	Posterior – Medial	0.927
	Medial – Lateral	0.069
Trabecular Separation	Anterior – Posterior	0.007
	Anterior – Lateral	0.679
	Anterior – Medial	0.716
	Posterior – Lateral	<0.001
	Posterior – Medial	0.092
	Medial – Lateral	0.148
Trabecular Number	Anterior – Posterior	<0.001
	Anterior – Lateral	0.003
	Anterior – Medial	<0.001
	Posterior – Lateral	<0.001
	Posterior – Medial	0.749
	Medial – Lateral	0.001

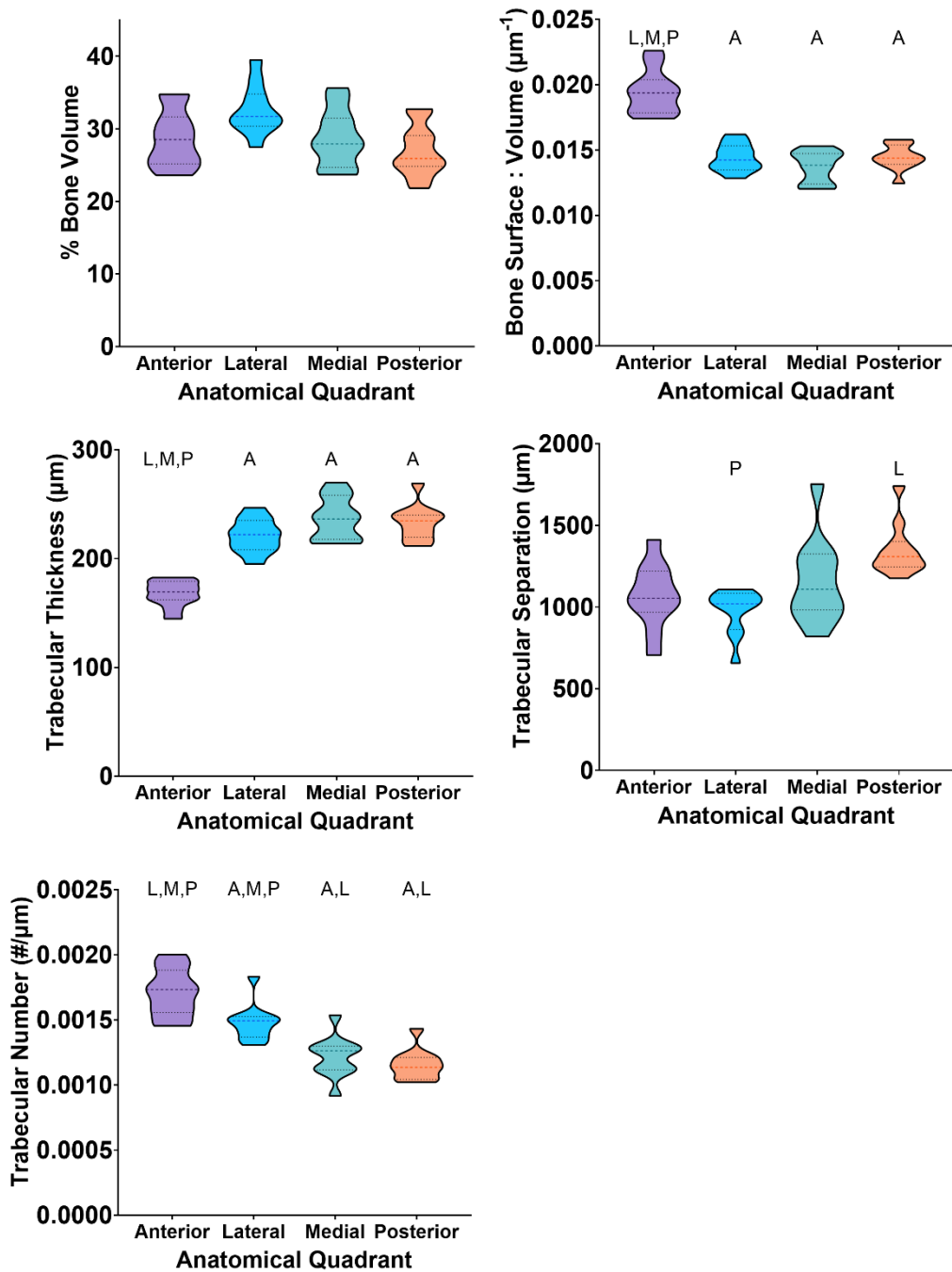


Figure 23. Comparison of histomorphometric variables by anatomical quadrant in fentanyl and sham animals. Letters above a bar indicate a significant difference ($p < 0.005$) between the column beneath the letter(s) and the anatomical quadrant indicated by the letter(s) where Anterior = A, Lateral = L, Medial = M, and Posterior = P. Dashed line indicates median, dotted lines indicate 1st and 3rd quartiles. Plots are truncated at the limits of data distribution.

Discussion

Opioid Variation

Trabecular bone is traditionally viewed as more metabolically active than cortical bone owing to its increased surface area relative to the cortex^{6,56,73}. Similar metabolic differences are shown in multiple species both between skeletal elements and bone tissue envelopes^{133–135} (inter- and intraskeletal variability, respectively). Previous work regarding opioid-induced changes to trabecular bone is limited, but shows increased trabecular separation and decreases in both trabecular thickness and overall bone volume fraction with opioid administration^{43,114}. However, these studies have some key differences which may confound direct comparison with the current work. Boshra⁴³ administered greater opioid doses (8 mg/kg/day morphine, 32 µg/kg/day fentanyl) for a longer exposure period (90 days) than the current study. Jain and colleagues¹¹⁴ only examined transdermal fentanyl, matching our dose at 25 µg/hr, but for a shorter duration (six weeks). Our results from the proximal tibiae did not fully support their findings, potentially implying a more complex network of factors affecting bone architectural changes resulting from opioid use, such as stress. Prolonged exposure to cortisol and other glucocorticoids inhibits osteocalcin production in osteoblasts, limiting bone formation^{136,137} similarly to opioid binding on osteoblasts^{53,112,138}. We routinely observed the fentanyl animals perform “thumping”, a warning signal where rabbits lift their hindlimbs and stamp them down together, creating a “thump” noise, to signal potential danger to other rabbits¹³⁹. The control animals were markedly more skittish after hearing any thumping. It is possible the increased stress from alerting to danger increased related hormones (e.g., cortisol) in the control animals, mimicking some of the opioid-induced

changes in bone¹⁴⁰. Glucocorticoid administration (such as cortisol) is shown to decrease cortical area, trabecular volume, and number of trabeculae in rabbits^{122,126,141}, mice¹⁴²⁻¹⁴⁴, and humans¹⁴⁵⁻¹⁴⁹. We may have seen the expected changes in the fentanyl group due to increased stress resulting from patch site irritation and erythema not present in the morphine animals¹³².

In general, morphine animals had greater trabecular Bone Volume but no change in related variables (e.g., number of trabeculae, trabecular separation) than saline controls. Morphine animals were much more lethargic than saline control animals immediately following opioid administration and for the next hour afterward¹³². Perhaps this daily hour of sedation, coupled with increased stress in the control animals due to thumping, limited bone-related changes observed between morphine and saline animals. The fentanyl animals exhibited fewer and thicker trabeculae than controls, but with no significant change in overall bone volume. These findings contrast with previous work on changes in bone remodeling due to opioid administration which found overall bone volume fraction^{43,114,150} and trabecular thickness decrease^{43,114} with opioid administration; however our other significant result, Trabecular Number, aligns with previous work¹¹⁴. Our conflicting data may result from too short of a drug administration period (eight weeks). For example, Jain and colleagues¹¹⁴ administered transdermal fentanyl to examine bone healing following fusion of the lumbar spine. Animals were treated for 10 weeks. Boshra⁴³ treated rats with either fentanyl, morphine, or tramadol over the course of nearly 13 weeks.

Beyond the administration period of our study, there may be further limitations owing to skeletal maturation. Previous studies have examined the skeletal maturity of

various skeletal elements in the New Zealand White rabbit both histologically and radiographically^{151,152} determining the long bones of the hindlimb to reach skeletal maturity between five and seven months of age as determined by physal (growth plate) fusion. Our rabbits were six months of age at the start of these experiments and eight months old at the end. The proximal tibia of the rabbit reaches skeletal maturity between 5.5 and 8 months of age (average: 6.8 months)¹⁵³. Our rabbits, while in this window of maturity, were on the lower limit and below the average age indicated above, due to supply chain issues and limited availability (see limitations), which suggests there may have still been active growth or modeling events taking place, possibly overshadowing the effects of our opioid administration. Our concurrent work¹⁵⁴ using these same methods to examine the tibial and femoral diaphyses in these same animals showed significant changes in bone porosity and pore size in line with previous work on human femur and rib¹⁵⁰. Results described here appear to counter our hypothesis of opioid-induced osteoporosis as indicated by increased Bone Volume in the morphine animals compared to saline controls and decreased Trabecular Thickness in fentanyl animals compared to sham patch animals, but with no change in overall bone volume. This may be the result of the increased potency of fentanyl relative to morphine⁴⁶, as morphine doses were adjusted for weight while fentanyl doses were constant, or may suggest other factors influencing Bone Volume in these animals in concert with opioid effects.

Regional Variation

All variables showed at least one significant regional variation irrespective of drug or control grouping except Bone Volume in fentanyl/sham patch analysis. Overall

trends, however, appear remarkably similar when comparing results from the fentanyl/sham analysis with the results of the morphine/saline animals. Rabbits are plantigrade animals, similar to humans, meaning in the stance phase of their gait cycle the plantar surface of the foot is in contact with the ground. Reaction forces from the feet striking the ground pass through the anterior and lateral compartments to the knee joint in rabbits¹⁵⁵. Our previous work examining femoral and tibial diaphyses of these animals showed medial and posterior quadrants had larger, more numerous cortical pores than anterior and lateral quadrants¹⁵⁴. A similar trend in porosity was observed in our current results (Figures 21 & 23). In general, more bone was present anterolaterally than posteromedially and Bone Surface : Volume was greater in the anterior quadrant than any other quadrant for both morphine and fentanyl analyses. The stability of these patterns between analyses suggests normal anatomical and perhaps functional biomechanical differences and limited influence from opioid treatment especially with no interaction between drug and anatomical region detected in any variable for either analysis. The limited variation in overall trend between analyses, such as % Bone Volume in the fentanyl/sham animals showing no significant changes between quadrants compared to lateral being significantly different from anterior and posterior quadrants in the morphine/saline animals, suggest biomechanical stress from locomotion may not be the only factor affecting bone porosity. These trends may be the combined result of numerous factors including stress from jacketing and associated cortisol release, changes in gait pattern from jacket irritation, and behavioral changes from fentanyl patch placement.

Patch placement and jacketing caused changes in activity levels and possible changes in gait of our fentanyl and patch control groups. For example, the rabbits' inability to remove the fentanyl patches caused matted fur and erythema¹³², and they appeared stressed as indicated by quick, shallow respirations and higher activity levels than their respective controls. Many of the fentanyl animals chewed through the hindlimb loops of the jackets which would subsequently be replaced. Skin irritation from these loops may have forced the animals to adjust their gait to prevent friction. This change in gait may have led to a difference in ground strike angle of the foot, changing the forces imparted on the bones, not seen in the sham patch animals¹⁵⁵. Increased activity coupled with the relatively young age of the rabbits as described above may have increased bone remodeling events by shifting the strain in the proximal tibia to be greater than the physiological range, indicating a need to deposit more bone tissue^{156,157}. This may explain some of the variation between the fentanyl and sham patch animals (e.g., trabecular thickness), but this is not likely a large cause for the observed variation between fentanyl and sham animals as the morphine and saline animals were not placed in jackets, as there was no risk of them removing a drug-eluting patch. For further details on the behavioral changes in these rabbits, see our previous work¹³².

Limitations and Future Directions

The current study had limitations including differing drug administration routes requiring the splitting of our control group. This limited our statistical power to detect changes between drug groups and control groups. It is possible that with either an increased control group or matching drug administration route to allow for analysis

between drug groups and a single control group our results may differ. Given our initial power analysis for this work suggesting seven animals would be sufficient, future work could include 10-12 animals to address potential complications during the experiment resulting in exclusion from the study. We further do not recommend the use of transdermal drug-eluting patches in a future study examining longitudinal effects of opioids¹³². As stated above, the adhesive in these patches caused fur matting and erythema which led to increased stress in our experimental animals. Those patches are best left to short-term applications.

Fur growth beneath the fentanyl patch application site may have limited drug uptake, potentially restricting the actual dose received by the animals and preventing us from detecting changes in bone microstructure that may otherwise be present. We did not collect routine blood samples as a part of this study, which would have confirmed drug dose, as attending veterinarians suggested the use of restrainers to collect the samples would cause undue stress in the animals. Future work should implement routine bloodwork to ensure proper drug delivery and consistent blood serum drug concentrations to guarantee proper dosing. Due to the relatively young age of the rabbits in this study and the average age of epiphyseal fusion in the proximal tibia, as discussed above, some growth and modeling events may have obstructed the effects of opioid administration. Our study employed rabbits at this relatively young age due to a supply chain issue with our vendor, requiring us to shift vendors with limited notice and availability. Future work should include animals over the maximum age for skeletal maturity in the skeletal element of interest, but young enough for the animal to not be undergoing changes in bone microstructure resulting from advanced age which may

prevent isolation of the potential effects of opioids. As rabbits have an average lifespan of 7-11 years and are considered geriatric at 5-6 years old¹⁵⁸, we recommend utilizing animals between nine months and one year old for similar experiments. Rabbits in this range would be past the maximum age of skeletal maturity for the tibia¹⁵³, but young enough to not have confounding factors from advanced age.

CHAPTER IV
BIOMECHANICAL PROPERTIES OF RABBIT MIDDLE RIBS FOLLOWING
PROLONGED OPIOID EXPOSURE

Introduction

This chapter represents the integrated bioscience component of this dissertation required as part of the University of Akron's Integrated Bioscience program. By incorporating methods from related fields (e.g., engineering), we can answer biological questions in new and unique ways while making our findings more relevant to a broader audience. Here we adapt mechanical testing commonly used in engineering fields to examine bone structural properties. In adapting methods from other fields, we can uncover common pitfalls to avoid.

Bone Material Properties

Bone is a viscoelastic, anisotropic composite material made up of a mineral matrix (hydroxyapatite, 65%), collagen fibers (25%) and water (10%)^{2,25,159}. Due to its anisotropy, the mechanical properties of bone will vary based on how the bone is loaded (e.g., longitudinal, transverse)¹⁶⁰. Nontraumatic (stress/fatigue) fractures are often caused by repetitive loading of bone whereas traumatic fractures are often caused by single large loading events¹⁶¹. Bone is stronger in compression than tension and weakest in shear¹⁶⁰. Bone porosity and number of loading cycles are inversely proportional with increased

porosity decreasing the number of loading cycles before failure. Haversian bone can, therefore, undergo about five times fewer loading cycles than primary bone owing to the increased porosity in Haversian bone¹⁶⁰.

Many bone pathological conditions affect bone mineral density and porosity such as osteoporosis, osteomalacia, and osteopetrosis¹⁶². Bone porosity (e.g., lacunae, Haversian canals) can serve as stress concentrators where microdamage initiates^{67,163}. Previous work focusing on changes in bone strength as a result of microdamage accumulation examine cyclic loading, showing increased microdamage reduces fatigue life¹⁶⁴⁻¹⁶⁶, and few studies exist examining maximum loading¹⁶⁷. Composite materials are typically stronger than a material comprised purely of either component (e.g., a material made strictly of either hydroxyapatite or collagen). Because of the heterogeneous nature of bone, transitions between components disrupt crack propagation. Bone health in terms of fracture risk can be affected by complex interactions between inherent biological factors (e.g., age, hormone concentrations) and lifestyle choices (e.g., smoking, sedentary/active behavior, or excessive alcohol/drug use, such as opioids)¹⁶⁸. In bone, the post-yield behavior is caused by the introduction of small cracks throughout the material¹⁶⁰. As these cracks accumulate and propagate, the stress-strain curve begins to plateau. However, a previous study suggests some of the plastic behavior of bone is caused by shear slipping of the cement lines of secondary osteons¹⁶⁹, though literature remains scarce.

Opioid Effects on Bone Biomechanical Properties

Opioids have been shown to decrease bone mineral density^{32,56} and osteoblast activity via reduction of serum androgen hormone (e.g., estrogen, testosterone) and osteocalcin concentrations, resulting in thinner and fewer trabeculae and increased cortical porosity, mimicking osteoporosis^{32,43,54,114,150}. This increased porosity, coupled with other cofactors (e.g., age, hormones, etc.), decrease the bone's fatigue life and allow bones to fracture more readily¹⁷⁰. Bones can, however, adapt to some of these changes to mitigate fracture risk. Bone can adapt in terms of both material properties and overall geometry¹⁷¹. In some instances, changing only the material properties of bone (e.g., increased mineralization) is not feasible and coupling material changes with geometric changes, such as increased bone diameter, can help limit fracture risk¹⁷¹. To counteract cortical thinning and resorption of endosteal bone tissue, Ruff and Hayes¹⁷² noted subperiosteal apposition helps limit the effects of endosteal resorption by increasing the second moment of area resulting from increased bone diameter. Some bone regions are prone to fracture (e.g., femoral neck, proximal and distal ends of the femur and tibia), perhaps due to undergoing less torsion and bending relative to the diaphyses during locomotion, such that the bone region undergoes less remodeling and the second moments of area decrease, increasing fracture risk at these locations with advancing age¹⁷².

Previous studies have examined the effects of opioids on bone maintenance or fracture healing in clinical settings in weight-bearing bones, including assessing bone mineral density of the spine^{55,56}, biomarkers of bone formation/resorption^{56,138} or medical

record analysis of fractures in the spine and pelvis⁵⁷. Further work has been performed in animal models including μ CT of rabbit spines¹¹⁴ and histology of rat femora^{43,173}. The present study seeks to isolate the effects of prolonged opioid use on bone quality and fracture risk without potentially confounding effects of weight-bearing. To this end, we used compression testing to examine how middle ribs yield after prolonged exposure to opioids. Ribs were chosen for this study as they are under relatively constant stress from respiration and do not bear body weight, limiting external effects from differences in lifestyles (i.e., sedentary or active) between animals. Many studies examining rib fractures and osteoporosis are studies examining the predictive value of various bone histomorphometric variables to assess osteoporosis¹⁷⁴, structural properties of ribs throughout the lifespan¹⁷⁵, large-scale medical record analyses in humans predicting future fracture risk, and measuring biomechanical properties of machined bone tissue specimens¹⁷⁶, but none specifically examining the effects of opioid-induced osteoporosis^{177,178}. As stated in Chapter III, rabbits are the smallest commonly used laboratory animal with cortical bone remodeling similar to that of humans, making them an excellent model for this study. We tested if 1) opioid use causes cortical thinning in non-weight-bearing bones, and if 2) biomechanical properties of opioid groups are lower compared to controls through examining stress-strain curves gathered from compression tests. Bone loss has been associated with opioid administration for analgesia^{32,54,179}. We hypothesized that opioid-treated animals would exhibit decreased cortical area and larger medullary area in rib cross-sections compared to controls. We further hypothesized ribs from the opioid groups would have worse performance across several biomechanical

parameters including reduced ultimate strength, strain, and toughness, and reduced peak stiffness.

Materials & Methods

Ribs were chosen as they are consistently loaded between individuals during respiration¹⁸⁰ and has become a common site for histologic assessment using the middle third of the sixth rib¹⁸¹. Due to our use of bilateral thoracotomy as a secondary means of euthanasia, some rabbits exhibited fractured right sixth ribs. We were further reserving the left sixth rib for a future study. For consistency among samples, we therefore excised the right fifth rib from each of the rabbits described in Chapter III. A previous study indicated that the middle ribs (ribs 4-7) have no significant morphometric differences in humans¹⁸². The fifth and sixth ribs of the rabbits appeared superficially similar with regard to overall morphology (e.g., curvature, diameter), but, to our knowledge, no comparative quantification of rabbit rib morphometry exists. We therefore presume any morphological differences between the fifth and sixth ribs are negligible, however further work is necessary to confirm this. In preparation for experiments, adhering soft tissues were removed from each rib using dental tools following standard maceration protocols⁷⁶. Ribs were wrapped in saline-soaked gauze, stored individually in petri dishes sealed with parafilm, and kept at -20°C until testing. As stated in Chapter III, our sample sizes of seven animals per drug group are consistent with previous studies examining induced osteoporosis in rabbit cortical and trabecular bone¹²⁰⁻¹²².

Gross Geometry & Compression Testing

Gross geometric measurements were gathered (Figure 24, Table 14) from each rib including span length, curve length, total cross-sectional area, and cortical area, as reported previously by Agnew and colleagues⁹⁰ which used similar engineering techniques to examine pediatric and adult human ribs. As stated previously, opioids limit bone formation, disrupting the balance between bone resorption and formation found in remodeling. Cross-sectional area measurements serve as a macroscopic proxy to compare bone resorption between groups. Span and curve lengths were measured to examine potential changes in bone modeling between groups. Following measurements, three serial sections ($n = 63$) were collected from the ventral end of each rib after removing a ~2 mm section of bone which formed the costochondral joint (Figure 25) using a handheld rotary tool equipped with a diamond cutting wheel and hand-filed with 150-grit sandpaper to produce parallel edges in preparation for testing. Specimens measured 5.05 ± 0.53 mm in length as confirmed with digital calipers. After sectioning, the medullary cavity of each specimen was cleared using a water flosser. Using a Leica S8AP0 (Leica, Wetzlar, Germany) microscope equipped with a MicroPublisher 5.0 RTV camera (Teledyne Photometrics, Tuscon, AZ), cross-sectional images were collected for each section at 1.6x magnification with a scale bar in view. A comparable technique using a DSLR camera was previously validated against other histologic techniques for measuring cortical area¹⁸³. These images were used to gather both cortical and endosteal area measurements (Table 14) using FIJI⁸⁰ after calibrating images according to a scale bar in the same photograph. Rib sections were placed on an Instron 5567 Universal Testing

Frame (Instron, Norwood, MA) equipped with a 1 kN load cell and compression test plates housed at Akron Polymer Training Services operated by The University of Akron's School of Polymer Science and Polymer Engineering. Bending tests were not employed in this study as bending a curved beam is complex and adds extra variation to analysis¹⁸⁴. Our structural properties (Table 15) were gathered from the force-displacement curves produced by longitudinal compression testing and variables were modified from a previous study by Agnew and colleagues examining human ribs using impact testing⁹⁰. Ribs were placed on the test platform and compressed at a strain rate of 0.01 mm/min until either fracture or, if distinct fracture could not be achieved, until the force plateaued post-failure (~30% of tests). Due to technical issues between the test frame software and the computer, seven specimen tests were unable to be collected, limiting the final sample size ($n = 56$).

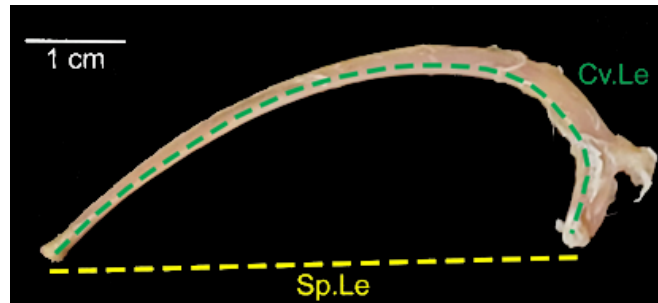


Figure 24. Representative image showing certain geometric properties collected for each rib. Curve Length (Cv.Le, green) is measured from sternal end to vertebral end along the inferior margin of the rib. Span Length (Sp.Le, yellow) is measured in a straight line from sternal end to vertebral end.

Table 14. Geometric properties gathered from bone area and rib measurements. These variables are taken from Agnew and colleagues⁹⁰.

Variable	Abbr. (unit)	Description	Equation
Span Length	Sp.Le (mm)	Length of rib from vertebral to sternal end	-
Curve Length	Cv.Le (mm)	Length of the rib measured along the curve of the inferior aspect of the rib	-
Total Area	Tt.Ar (mm ²)	Total cross-sectional area	-
Endosteal Area	Es.Ar (mm ²)	Endosteal area (area of medullary cavity) (Used for Cortical Area equation only)	-
Cortical Area	Ct.Ar (mm ²)	Cortical bone area	Tt.Ar – Es.Ar
% Cortical Area	% Ct.Ar (%)	Cortical bone area normalized by total cross-sectional area	Ct.Ar/Tt.Ar

Table 15. Structural properties gathered from the stress-strain curve. These variables are modified from Agnew and colleagues⁹⁰.

Variable	Abbr. (unit)	Description
Peak Stress	F _P (MPa)	Maximum force in Z direction normalized by cortical area
Peak Strain	ε _P (mm/mm)	Maximum displacement in Z direction normalized by specimen length
Maximum Young's Modulus	K _{Max} (N/mm)	Maximum slope of linear portion of stress-strain curve
Toughness	U _T (J/m ³)	Total area under the stress-strain curve to peak stress



Figure 25. Representative image of serial sections procured from each rib, Ventral (V), Intermediate (I), and Lateral (L), in preparation for compression testing. Apparent differences in shape are due to resting orientation of sections in the image.

Data Analysis

Analysis of stress-strain curves was completed using custom code developed in MATLAB R2021b (Mathworks, Natick, MA; Appendix F). Briefly, raw data output from the compression tests are imported and each datapoint was converted from force and displacement to stress and strain, respectively, by consulting a data file loaded with cortical bone area and original sample length. Samples displayed complex loading behavior as seen in the highly variable force-displacement curves relative to other tested samples (Figure 26) compared to that of isotropic materials such as metals and plastics. Specimens were observed throughout testing and specimens that exhibited small dips in stress (Figure 26, 13sI) corresponded with longitudinal fractures in the specimen. Many of the specimens did not produce a distinct ultimate fracture and instead produced a “crumbling” failure. In tests that did not produce an ultimate fracture, specimens

exhibited a post-peak loading curve similar to a standard curve of rock, including crack linkage and faulting¹⁸⁵ (Figure 27). This behavior could be the result of incomplete ossification (see Limitations) and limited the information we could glean from analyzing the post-yield region requiring us to crop the data at peak stress. Further, due to this complex loading behavior, we were unable to collect a consistently reliable yield point for analysis in many of our compression tests after attempting three different coding methods including 1) user selection of automatically detected inflection points, 2) finding longest span of negative inflection, and 3) finding the point after the maximum slope at which slope reaches 95% the maximum. As we were not confident the yield point we determined from any of the above methods was reliable, and fully manual selection of yield point is relatively arbitrary, we exclude reporting yield stress/strain here. Stress-strain curves were splined to remove noise. During splining, the first and last datapoint were weighted to anchor them as true points. To ensure stiffness captured slope in the linear region and not in the spline near the anchored points, we cropped the first and last 25 data points from the stiffness calculation (Appendix F). The number of data points cropped was determined through extensive trial and error with 25 giving the most consistent result among all compression tests. Biomechanical variables (Table 15) were collected from these splined curves and saved to an output file for statistical analysis. Elastic (Young's) modulus appeared to vary irregularly and unpredictably with strain, therefore, the maximum elastic modulus is reported as a substitute as has been done in previous work on bovine long bones and human lumbar vertebrae¹⁸⁶.

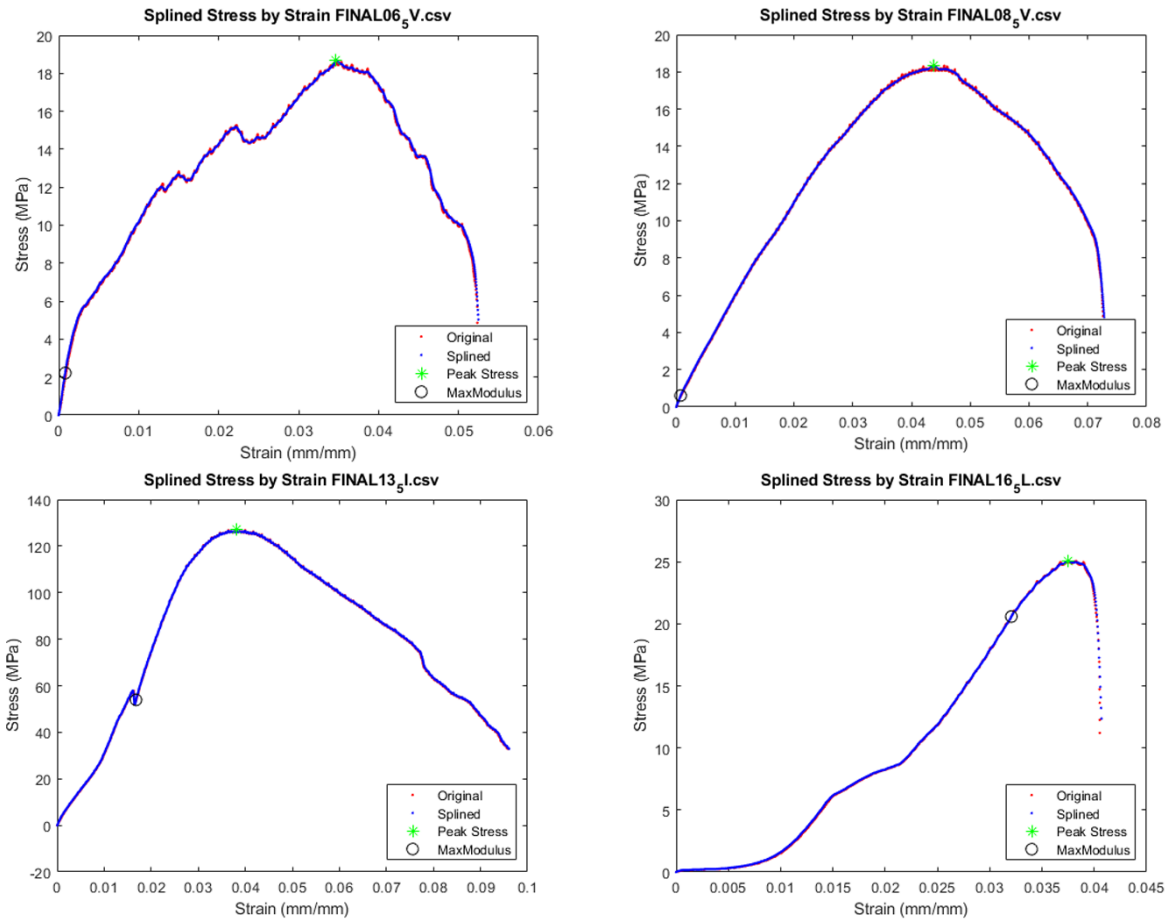


Figure 26. Representative stress-strain curves showing the highly variable loading patterns seen in our sample. Note 08₅V appears to be in the yield region at the beginning of the test and 13₅I has smaller, longitudinal fractures (sudden drop in stress) but no complete failure occurred. Red lines are the raw data collected from the test frame. Blue lines are a spline of the original data superimposed. The open black circle indicates the maximum Young's modulus for that curve and green star indicates peak stress/strain.

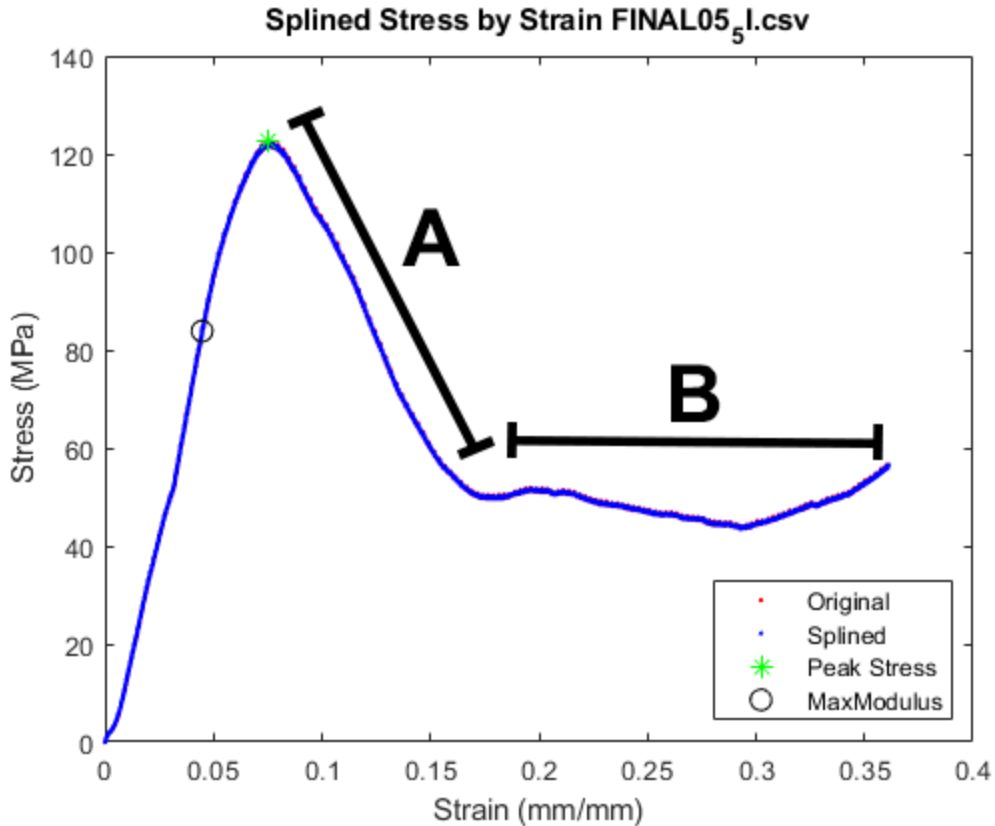


Figure 27. Representative stress-strain curve exhibiting post-peak behavior similar to the loading of rock. Strain softening occurs at Region A and is caused by linkage of microcracks into macrocracks. Region B indicates faulting caused by sliding of crack surfaces against each other. Details of these regions are explained in depth by Schultz¹⁸⁵.

Statistical Analysis

All statistical analyses were completed using SPSS v26 (IBM, Armonk, NY). Due to the differing pharmacokinetics of fentanyl and morphine^{128,129,187} and difference in administration route, separate analyses were warranted examining only the differences between each opioid group and their respective control. We utilized two separate one-way ANOVAs with step-down Bonferroni corrections (Appendix C) using drug group (morphine vs. saline, fentanyl vs. sham patch) as the independent variable. Residuals

from each ANOVA were tested to ensure normality and variance assumptions were met utilizing Shapiro-Wilk and Levene's tests, respectively^{84,85}. Any variable that violated assumptions was log₁₀-transformed and re-analyzed. If the variable continued to violate assumptions, it was re-analyzed using a step-down Bonferroni-corrected one-way ANOVA with a bootstrapped^{88,89} sample created from 1000 replicates.

Results

As there were no significant differences between morphine and saline animals nor between fentanyl and sham patch animals in any biomechanical variable (Figure 28, Table 16) we reject our hypotheses that bone exposed to prolonged opioid use performs worse biomechanically than controls and that cortical area is significantly decreased in bones of opioid-dosed animals. Morphine and saline animals further showed no significant differences in any geometric variables. Fentanyl animals had significantly shorter span length (mean = 3.11 mm shorter) than the sham patch animals ($F[1,28] = 15.271, p = 0.001$), but no other geometric variables were significantly different between fentanyl and sham patch animals (Figure 29, Table 17).

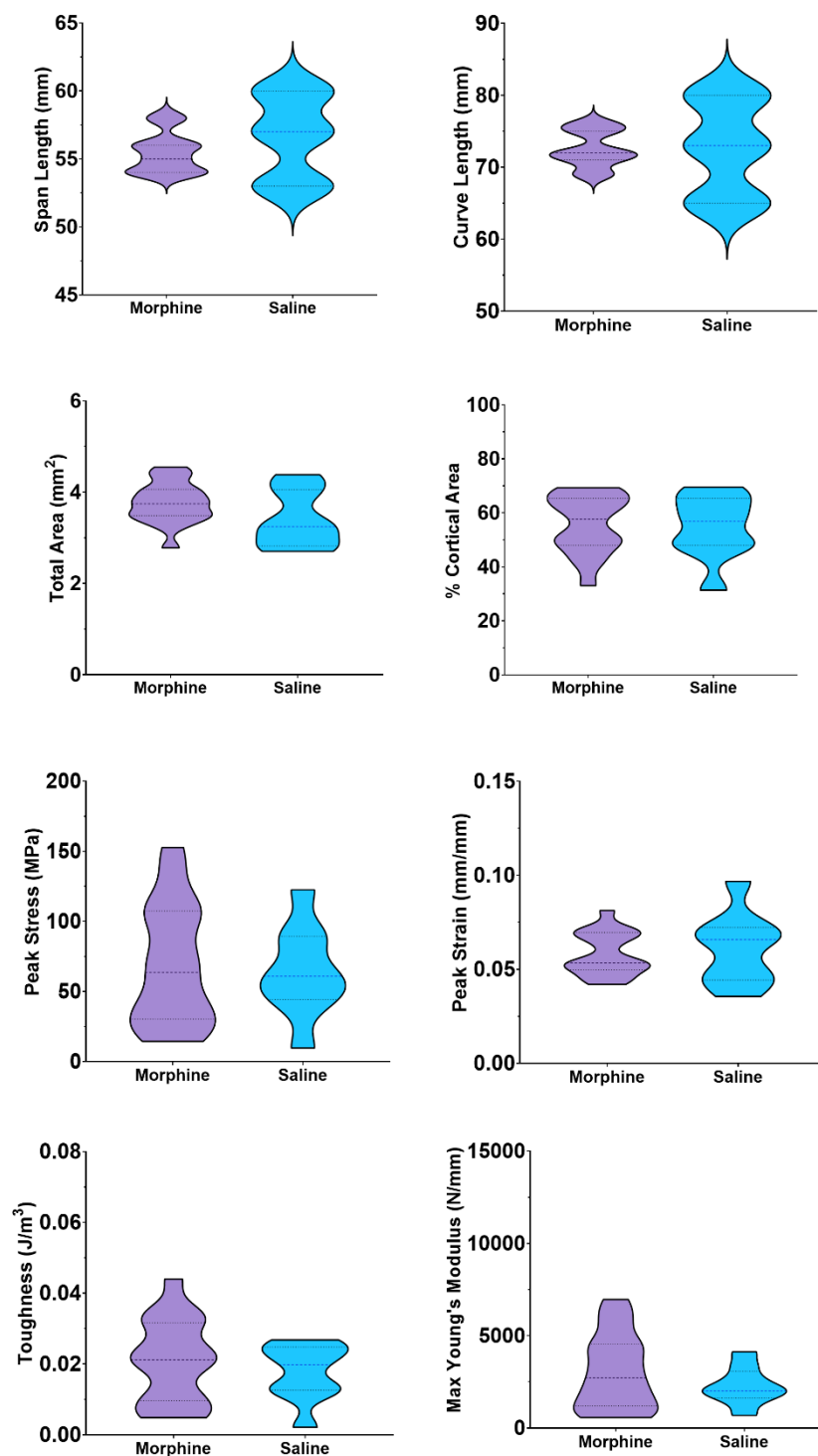


Figure 28. Comparison of geometric and biomechanical variables between morphine and saline animals. Dashed line indicates median, dotted lines indicate 1st and 3rd quartiles. Plots are truncated at the limits of data distribution unless doing so obscured quartile lines.

Table 16. One-Way ANOVA results for drug group (morphine vs. saline).

Variable (Data Transformation)	F	p-value	ω^2
Span Length (Bootstrap)	1.867	0.185	0.032
Curve Length (Bootstrap)	0.006	0.939	-0.040
Total Area (No Transformation)	2.925	0.100	0.069
% Cortical Area (No Transformation)	0.054	0.819	-0.038
Peak Stress (No Transformation)	0.089	0.768	-0.036
Peak Strain (No Transformation)	0.229	0.637	-0.031
Toughness (No Transformation)	0.490	0.491	-0.020
Max Modulus (Log ₁₀)	0.170	0.684	-0.033

Table 17. One-Way ANOVA results for drug group (fentanyl vs. sham patch).

Variable (Data Transformation)	F	p-value	ω^2
Span Length (Bootstrap)	15.271	0.001	0.324
Curve Length (Bootstrap)	2.984	0.095	0.062
Total Area (Log ₁₀)	0.512	0.468	-0.017
% Cortical Area (No Transformation)	2.244	0.145	0.040
Peak Stress (Log ₁₀)	0.796	0.534	-0.020
Peak Strain (No Transformation)	0.380	0.543	-0.021
Toughness (No Transformation)	0.086	0.772	-0.031
Max Modulus (Log ₁₀)	0.207	0.653	-0.027

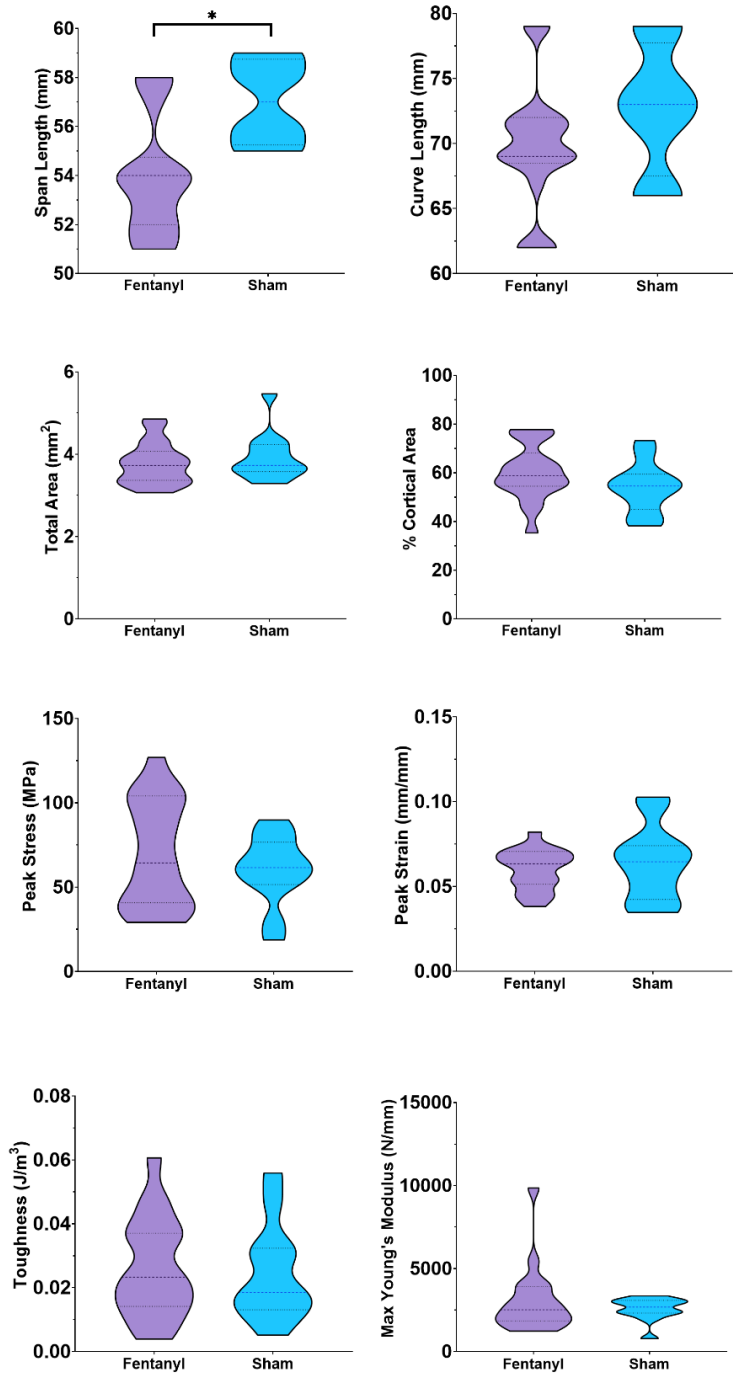


Figure 29. Comparison of geometric and biomechanical variables between fentanyl and sham animals. Asterisks indicate a significant difference between fentanyl and sham patch ($p < 0.003$). Dashed line indicates median, dotted lines indicate 1st and 3rd quartiles. Plots are truncated at the limits of data distribution.

Discussion

Contrary to our hypotheses, there were no significant differences between morphine and saline animals and the only significant difference between fentanyl and sham patch animals was found in span length. Fentanyl animals actively attempted to remove the fentanyl patch from their interscapular region and were routinely observed balancing on their hindlegs and twisting in attempts to remove the patches with their mouths even when fitted with mesh jackets. This behavior was not seen in the sham patch animals. As stated in Chapter III, the fentanyl patches caused fur matting and erythema which the sham patches did not.

Previous work calculated BMU longitudinal erosion rate (LER) in the rabbit tibial diaphysis to be $23.80 \mu\text{m}/\text{day}^{188}$. If this rate is consistent in both cortical and trabecular remodeling, at this velocity BMUs could resorb ~ 1.33 mm of bone during our experimental timeframe (8 weeks). While this 1.33 mm is less than half the 3.11 mm decrease in span length we report here, it is likely BMU LER varies between skeletal elements as remodeling rate and BMU activation frequency vary between skeletal elements¹⁸⁹ and is known to be greater in ribs than in weight-bearing bones in both animal models and humans²¹. Given the above relevant literature, it is possible the routine twisting of the body by the fentanyl animals introduced an increased number of loading events in the ribs, inducing modeling changes to shorten the span length of the ribs. It is also possible this could simply be normal biological variation. One of these rabbits, for example, had substantially longer limb bones (e.g., femur, tibia) than the other 20 rabbits when measured for concurrent experiments. It is possible through

random assignment to groups, the animals in the fentanyl group simply had shorter ribs than the other groups.

Previous work on rib stress fractures in rowers¹⁹⁰ suggests increased strain from repetitive muscle loading leads to fracture. This could also potentially explain why span length differed significantly only in the fentanyl animals compared to the sham patch animals, whose sham patches did not cause nearly the same skin irritation as the transdermal fentanyl patches, and not between morphine and saline animals who had no drug-eluting patch to attempt to remove. A previous study by Tommerup and colleagues¹⁹¹, however, determined pig forelimb loading through exercise did not affect loading in the middle ribs as evidenced by bone apposition observed in the humerus, but not in the ribs. A similar phenomenon may be possible in rabbits as both animals are quadrupeds, however, there are numerous differences between pigs and rabbits, including body size, gait (unguligrade vs. plantigrade), and locomotion (walking vs. saltatory), that make extrapolation to rabbits difficult. Further work is necessary to determine if there are effects on middle ribs through forelimb loading in rabbits. As stated in Chapter III, while the overall weight of rabbits was significantly different between Week 0 and Week 8, there were no significant differences between drug groups. Therefore, overall weight differences between drug groups do not explain the variation in span length seen here. Natural variation between the rabbits may be a more likely explanation for this change. Due to our random assignment of animals into experimental groups, it is possible the fentanyl group animals had longer ribs than the other groups by chance.

Our use of bilateral thoracotomy as a secondary means of euthanasia introduced a large amount of force as indicated by the fracturing of the right sixth rib in a number of animals. It is possible this large force imparted on the thorax introduced enough force on the ribs to deform plastically, as indicated by the few stress-strain curves that appeared to be post-yield at the start of compression testing (Figure 26, 08₅V). However, a previous study¹⁷⁶ examining impact testing of human ribs, after loading the whole rib to failure in bending, contrasts this, showing the only mechanical properties that were different between ribs previously injured and the contralateral uninjured ribs were yield stress and strain. It should be noted the authors¹⁷⁶ report the strain rate for these tests was 0.5 strain/s which is much faster than the current study (3.3×10^{-5} strain/s). As bone is viscoelastic, this change in strain rate can have a large effect on the response of bone and thus make comparing these studies difficult. These findings may help to explain our inability to isolate a reliable yield point in the current study. Future work should employ a different secondary means of euthanasia that does not potentially impact the mechanical properties of the ribs (e.g., potassium chloride injection¹⁹²) to prevent confounding loading events that may limit observable differences.

As stated in Chapter III, multiple drug administration routes required splitting our control group, thus limiting our statistical power. Future work should incorporate the same drug administration route¹³² and larger sample sizes (e.g., 10-12 animals per group), as discussed in Chapter III, past the age of skeletal maturity. While the age of skeletal maturity varies by skeletal element, previous work¹⁹³ has shown rabbit ribs to begin ossifying at 15 days postnatal in the head and tubercle, and the rib is fully ossified by 90

days postnatal. Our rabbits, at 6 months old at the beginning of the experiments, were well past this timepoint and therefore our results are likely not due to incomplete ossification of the ribs.

Our samples further exhibited complex loading behavior (Figure 26), likely due in part to a combination of inherent biological variation, flaws in sample geometry from preparation (e.g., non-parallel machined edges), or genuine material property differences. The resulting stress-strain curves differed from standard curves seen in both isotropic and anisotropic materials (e.g., manufactured metals, plastics, and composites). Elastic modulus and toughness appeared to vary irregularly and unpredictably with strain, suggesting micro-failures or other, more complex, loading responses. This precluded reliable identification of yield stress and may have overshadowed changes in toughness caused by opioid administration. Previous work testing compression of tibiae¹⁹⁴, femora¹⁹⁵, and lumbar vertebrae^{196,197} sections in sheep¹⁹⁶, rabbits^{195,197}, and humans¹⁹⁴ show more standard-looking loading curves, however all these studies used machined samples from weight-bearing bones and some used substantially higher strain rates^{194,195} than the current study. More recent work from Albert and colleagues¹⁵⁹ found human rib core specimens loaded in compression at 0.005 strain/s to have an ultimate stress of ~150 MPa, somewhat higher than our reported values, but with a greater strain rate than our current study. Although, rabbits have thicker osteon walls and increased osteon density in the femur compared to humans and non-human primates¹⁹⁸. This is purported to equate to stronger cortical bone for large forces introduced by rabbit locomotion¹⁹⁸. If true, we

should expect greater ultimate stress in rabbits compared to humans, but further direct comparative work is required.

Our variable curves may further have been the result of end-effects in the compression testing. These effects are the result of compressive shear at the ends of the specimen from direct contact with the platens of the test frame¹⁹⁹. Any variability in the ends of the specimen could cause toe slip and non-linear regions of the stress-strain curve which affects determination of elastic modulus. A previous study examining end-effects in trabecular bone sections of long limb bones in cows and lumbar vertebrae of humans during compression testing found average elastic modulus is underestimated 22-38% which may be related to anatomic location of the specimen and variability of bone architecture at machined ends¹⁸⁶. Our rib specimens may therefore have had small imperfections in the parallel ends from cutting which caused artifacts during testing. This same study determined a more accurate method of measuring elastic modulus with two extensometers attached to endcaps holding the specimen¹⁸⁶. This technique was not feasible in our current study as specimens with lengths four times the diameter were required, which would introduce some gross bone curvature into our sample, increasing the chance of buckling failure. Our variable stress-strain curves may have further limited the power of our relatively simple analysis program and further tuning is required. Future studies should incorporate histologic analysis to confirm material property differences (e.g., bone mineral density and microstructural changes) in the rib following exposure to opioids, as previous studies suggest^{150,200}. Methods utilizing 3D histomorphometric methods such as μ CT may serve especially well as confirmation of mechanical

testing^{201,202}. A previous study showed bone volume fraction explained 87% of the variation seen in elastic modulus from compression testing of human lumbar vertebrae²⁰¹.

Further difficulty in mechanical testing of bone is found in a lack of consistent testing parameters and terminology used between studies. A previous study examining the effects of bisphosphonates on bone mechanical properties in dog rib determined toughness to be variably defined in numerous other mechanical studies, sometimes defined as total area under the stress-strain curve, and in other studies defined as the energy underneath the curve only until peak stress, without any notation indicating a change from standard terminology²⁰³. This same study notes >85% of the change in toughness in their experiments was in the post-yield curve and cropping the curve at peak stress likely limits the use of toughness as a meaningful variable²⁰³. This is likely why toughness in our current study showed no significant differences between groups as we cropped our stress-strain curves at peak stress due to the highly variable post-peak region. There is further no standard protocol for mechanical testing of bone, which makes drawing comparisons between studies difficult and fraught with potential error due to variability in sample preparation and testing setup. A review by Zhao and colleagues²⁰⁴ calls for standardization of mechanical testing in bone similar to the standards set by the former American Society for Testing and Materials (currently, ASTM International) for engineered materials and gives some specific recommendations, detailed below.

Recommendations for standardized bone mechanical testing proposed by Zhao and colleagues²⁰⁴ include ensuring loading along the material axis instead of the anatomic axis as bones may not be loaded in purely anatomical directions (e.g., anterior-posterior,

medial-lateral) and instead may be loaded obliquely to these axes. Testing along anatomical axes will likely provide differing mechanical properties due to bone's anisotropic nature. Our samples were not ideal for this recommendation as ribs are curved bones and there may be microscopic curvature within our small sections which would indicate we loaded the ribs along an anatomical axis, not the material axis. To correct this, future studies could use μ CT or similar imaging techniques to determine the material axis prior to sectioning to ensure samples are cut along these axes. For machined (e.g., cored) specimens, a minimum of 5 mm is recommended with a 2:1 height : width ratio to prevent buckling failure²⁰⁴. Our rib specimens were ~3 mm along the widest axis and averaged 5.05 mm in height which was above these recommendations. We further did not identify buckle failure in any of our tests.

Sample preparation and storage varies widely between studies including whether samples were stored frozen prior to testing, if samples were kept dry, wet, or rehydrated prior to testing which all give somewhat different mechanical properties²⁰⁴. The current recommendation is that samples be kept frozen in saline until testing as was done in this and previous studies^{90,175,204}. Future work should implement these recommendations to make comparisons across studies and between research groups more feasible. Further recommendations include retention of bone marrow during testing. Previous studies have performed mechanical tests both with and without marrow included^{205,206} and the concern of marrow inclusion is rooted in maintaining the hydration of the tissue prior to and during testing. This could reasonably be mediated through storage in saline-soaked gauze as was done in our study. Our current study did not include marrow which may limit the

actuality of our compression tests as marrow would be present *in vivo*. However, including the marrow in our testing would require confinement of the specimen during testing to prevent leakage of the marrow on the test frame which was not feasible for our setup. Confinement of specimens produces its own set of obstacles during testing such as limiting lateral deformation²⁰⁴ and artificially increased stiffness²⁰⁷.

Our results show limited significant differences between drug groups and their respective controls. Much of this is possibly due to complex loading behavior from compression of naturally curved structures leading us to loading the specimens along an axis to which it is not conformed. Further confounding may be due to imperfections in the parallel edges from specimen procurement, or perhaps there is truly no difference in rib structural properties with opioid use. It is difficult to interpret our results in relation to the existing literature as no standards exist for such testing and ribs are scarcely used. Commonly tested elements include long bones such as the humerus, femur, and tibia²⁰⁴. Until such a time as standards of mechanical testing on bone are agreed upon and used consistently it will remain difficult to elucidate how bone structural properties vary between species, skeletal elements, and even between regions of the same skeletal element.

CHAPTER V

CONCLUSIONS

The research described here aimed to identify changes to bone microstructure and biomechanics resulting from prolonged opioid exposure. The bone remodeling process in the BMU can become dysregulated through changes in hormones or introduction of other factors (e.g., alcohol, drugs, lifestyle, age, etc.). To better isolate the effects of opioids on bone we first examined how healthy bone microstructure changes with advancing age and between sexes. We then examined the effects of opioids on trabecular bone morphometry and rib strength.

Chapter II examined the changes of the lacuno-canalicular network between males and females across the lifespan using both SR μ CT and CLSM. Previous work has utilized either SR μ CT or CLSM separately to examine similar variables, but none have incorporated both imaging methods nor the influence of both age and sex on bone microstructure. Utilizing both imaging methods, we sought to determine how vascular pores and the LCN change throughout the lifespan and between sexes in the anterior femur. We hypothesized that pore size and connectivity would increase with advancing age while lacunar and canalicular diameters would decrease. We further hypothesized that these changes would be exacerbated in females owing to the shift in estrogen concentration with the onset of menopause. Our results, in general, supported these

hypotheses with pore volume increasing while pore density decreased, suggesting pore convergence. Lacunar volume also decreased with advancing age. Females further had significantly increased canaliculi diameter and separation than males supporting our hypothesis that females would have more marked changes than males. While our study was limited in the bone envelopes and anatomical regions imaged, this work serves as a foundation for the combined effects of age and sex on bone microstructure, providing a more holistic understanding. To expand this work, future studies should examine these effects between anatomical region, bone envelopes, and skeletal elements, including both weight-bearing and non-weight-bearing bones.

Once we determined how bone microstructure changes with age and sex, we sought to examine the similarities to aging in bone caused by prolonged opioid administration in a model organism in Chapters III and IV. We examined both trabecular bone microstructural changes in the proximal tibia (Chapter III) and overall bone strength in the rib (Chapter IV). In Chapter III, we investigated whether opioid exposure caused decreased bone volume and/or trabecular thinning. We hypothesized opioid groups would exhibit decreased bone volume and thinner trabeculae than control animals. Fentanyl animals had increased trabecular thickness and separation than controls in the proximal tibia, but no overall change in bone volume whereas morphine animals exhibited increased bone volume compared to controls, contradicting our hypotheses. The exhibited differences by anatomical quadrants showed similar patterns of change between drug groups and controls, suggesting biomechanical and anatomical constraints, possibly limiting effects caused by opioid administration. These results are supported by our

concurrent work on the tibial and femoral diaphyses. These regional and opioid differences may be confounded by the relatively young age of our animals due to supply chain issues and stress caused by the transdermal fentanyl patches and subsequent jacketing of animals to prevent patch removal. Despite these limitations, this work does indicate opioids (i.e., fentanyl) decreases trabecular number. Future work should refrain from transdermal patch use and ensure the experimental animals are above the age of skeletal maturity for the skeletal element of interest.

To determine how microstructural changes from opioids affect overall bone mechanics, we performed compression tests on a middle rib, a bone under relatively constant stress from respiration and does not bear body weight. This relatively constant loading pattern should limit the effects of lifestyle on the observed differences. This chapter comprised the integrated bioscience portion of this dissertation, answering biological questions with engineering techniques. This integrated approach allowed us to produce a more comprehensive and cohesive understanding of biological mechanisms involved in changes to bone strength by examining data from 2D imaging and mechanical testing to determine macro- and microstructural changes resulting from opioid exposure. We hypothesized opioid groups would exhibit decreased cortical area and reduced ultimate strength, toughness, and reduced peak stiffness compared to controls. Contrary to our hypotheses, there were no significant differences in biomechanical parameters between either opioid group and controls. Neither did morphine animals exhibit decreased geometric properties compared to controls. Fentanyl animals, however, did exhibit decreased span length of the rib compared to controls

which may be a result of increased loading events in the rib from routine attempts at transdermal fentanyl patch removal, or normal biological variation. Our results are potentially confounded by forces imparted during bilateral thoracotomy. Future studies should utilize a different means of euthanasia and incorporate histological analysis to confirm microstructural differences near the sample site for mechanical testing. This study represented proof-of-principle of changes in bone strength caused by opioid use examined with mechanical testing.

Through the combined results of these projects, we have elucidated some of the effects to bone microstructure resulting from prolonged opioid use. While our work had limitations stemming from different opioid administration routes and supply chain issues, this work serves as foundation for further examination. Our lab is already preparing for follow-up studies with larger sample sizes, utilizing subcutaneous injections for all drug administration and incorporating both male and female rabbits to examine differences between sexes.

REFERENCES

1. National Institutes of Health. Overdose Death Rates. National Institute on Drug Abuse. 2022 Jan 20 [accessed 2022 Feb 11]. <https://www.drugabuse.gov/drug-topics/trends-statistics/overdose-death-rates>
2. Currey JD. The Structure of Bone Tissue. In: *Bones: Structure and Mechanics*. Princeton, NJ: Princeton University Press; 2002. p. 3–26.
3. Frost HM. Tetracycline-Based Histological Analysis of Bone Remodeling. *Calcified Tissue Research*. 1969;3(1):211–237. doi:10.1007/BF02058664
4. Maggiano CM. Making the Mold: A Microstructural Perspective on Bone Modeling during Growth and Mechanical Adaptation. In: Stout SD, Crowder CM, editors. *Bone Histology: An Anthropological Perspective*. 1st ed. Boca Raton, FL: Taylor & Francis; 2011. p. 45–90. doi:10.1201/b11393-7
5. Rodríguez JI, Palacios J, García-Alix A, Pastor I, Paniagua R. Effects of Immobilization on Fetal Bone Development. A Morphometric Study in Newborns with Congenital Neuromuscular Diseases with Intrauterine Onset. *Calcified Tissue International*. 1988;43(6):335–339. doi:10.1007/BF02553275
6. Parra-Torres AY, Valdés-Flores M, Velázquez-Cruz LO and R. Molecular Aspects of Bone Remodeling. *Topics in Osteoporosis*. 2013. <https://www.intechopen.com/books/topics-in-osteoporosis/molecular-aspects-of-bone-remodeling>. doi:10.5772/54905
7. Martin RB. Is All Cortical Bone Remodeling Initiated by Microdamage? *Bone*. 2002;30(1):8–13. doi:10.1016/S8756-3282(01)00620-2
8. Burr D. Targeted and Nontargeted Remodeling. *Bone*. 2002;30(1):2–4. doi:10.1016/S8756-3282(01)00619-6
9. Stout S, Crowder C. Bone Remodeling, Histomorphology, and Histomorphometry. In: Stout S, Crowder C, editors. *Bone Histology: An Anthropological Perspective*. Boca Raton, FL: CRC Press; 2012. p. 1–21.
10. Martin RB. Targeted Bone Remodeling Involves BMU Steering as well as Activation. *Bone*. 2007;40(6):1574–1580. doi:10.1016/j.bone.2007.02.023

11. Parfitt AM. New Concepts of Bone Remodeling: A Unified Spatial and Temporal Model with Physiologic and Pathophysiologic Implications. In: Agarwal SC, Stout SD, editors. *Bone Loss and Osteoporosis: An Anthropological Perspective*. Boston, MA: Springer US; 2003. p. 3–17.
12. Martin RB. Toward a Unifying Theory of Bone Remodeling. *Bone*. 2000;26(1):1–6. doi:10.1016/S8756-3282(99)00241-0
13. Robling AG, Castillo AB, Turner CH. Biomechanical and Molecular Regulation of Bone Remodeling. *Annual Review of Biomedical Engineering*. 2006;8(1):455–498. doi:10.1146/annurev.bioeng.8.061505.095721
14. Parfitt AM, Drezner MK, Glorieux FH, Kanis JA, Malluche H, Meunier PJ, Ott SM, Recker RR. Bone Histomorphometry: Standardization of Nomenclature, Symbols, and Units. Report of the ASBMR Histomorphometry Nomenclature Committee. *Journal of Bone and Mineral Research*. 1987;2(6):595–610. doi:10.1002/jbmr.5650020617
15. Robling AG, Turner CH. Mechanical Signaling for Bone Modeling and Remodeling. *Critical reviews in eukaryotic gene expression*. 2009;19(4):319–338.
16. Rubinacci A, Villa I, Dondi Benelli F, Borgo E, Ferretti M, Palumbo C, Marotti G. Osteocyte-Bone Lining Cell System at the Origin of Steady Ionic Current in Damaged Amphibian Bone. *Calcified Tissue International*. 1998;63(4):331–339. doi:10.1007/s002239900536
17. Miller S, Saint-Georges L de, Bowman B, Jee W. Bone Lining Cells: Structure and Function. *Scanning Microscopy*. 1989;3(3). <https://digitalcommons.usu.edu/microscopy/vol3/iss3/27>
18. Frost HM. The skeletal intermediary organization. *Metabolic Bone Disease and Related Research*. 1983;4(5):281–290. doi:10.1016/S0221-8747(83)80001-0
19. Martin RB, Burr DB, Sharkey NA, Fyhrie DP. *Skeletal Tissue Mechanics*. 2nd ed. New York: Springer-Verlag; 2015. www.springer.com/us/book/9781493930012
20. Delaisse J-M, Andersen TL, Kristensen HB, Jensen PR, Andreasen CM, Sørensen K. Rethinking the bone remodeling cycle mechanism and the origin of bone loss. *Bone*. 2020;141:115628. doi:10.1016/j.bone.2020.115628
21. Andronowski JM, Cole ME. Current and emerging histomorphometric and imaging techniques for assessing age-at-death and cortical bone quality. *WIREs Forensic Science*. 2021;3(2):e1399. doi:<https://doi.org/10.1002/wfs2.1399>

22. Cooper DML, Thomas CDL, Clement JG, Hallgrímsson B. Three-Dimensional Microcomputed Tomography Imaging of Basic Multicellular Unit-Related Resorption Spaces in Human Cortical Bone. *The Anatomical Record Part A: Discoveries in Molecular, Cellular, and Evolutionary Biology*. 2006;288(7):806–816. doi:10.1002/ar.a.20344
23. Borggaard XG, Pirapaharan DC, Delaissé J-M, Søre K. Osteoclasts' Ability to Generate Trenches Rather Than Pits Depends on High Levels of Active Cathepsin K and Efficient Clearance of Resorption Products. *International Journal of Molecular Sciences*. 2020;21(16):5924. doi:10.3390/ijms21165924
24. Merrild DM, Pirapaharan DC, Andreasen CM, Kjærsgaard-Andersen P, Møller AM, Ding M, Delaissé J-M, Søre K. Pit- and Trench-Forming Osteoclasts: A Distinction that Matters. *Bone Research*. 2015;3(1):1–11. doi:10.1038/boneres.2015.32
25. Martin RB, Burr DB, Sharkey NA, Fyhrie DP. *Skeletal Biology*. In: *Skeletal Tissue Mechanics*. 2nd ed. New York: Springer-Verlag; 2015. p. 35–93. www.springer.com/us/book/9781493930012
26. Harrison KD, Cooper DML. Modalities for Visualization of Cortical Bone Remodeling: The Past, Present, and Future. *Frontiers in Endocrinology*. 2015;6:Article 122. doi:10.3389/fendo.2015.00122
27. Bonewald LF, Johnson ML. Osteocytes, Mechanosensing and Wnt Signaling. *Bone*. 2008;42(4):606–615. doi:10.1016/j.bone.2007.12.224
28. Klein-Nulend J, Bakker AD, Bacabac RG, Vatsa A, Weinbaum S. Mechanosensation and Transduction in Osteocytes. *Bone*. 2013;54(2):182–190. (The Osteocyte). doi:10.1016/j.bone.2012.10.013
29. Klein-Nulend J, Nijweide PJ, Burger EH. Osteocyte and Bone Structure. *Current Osteoporosis Reports*. 2003;1(1):5–10. doi:10.1007/s11914-003-0002-y
30. Burger EH, Klein-Nulend J, Smit TH. Strain-Derived Canalicular Fluid Flow Regulates Osteoclast Activity in a Remodelling Osteon—A Proposal. *Journal of Biomechanics*. 2003;36(10):1453–1459. (Bone Cell and Tissue Mechanics). doi:10.1016/S0021-9290(03)00126-X
31. Atkins A, Dean MN, Habegger ML, Motta PJ, Ofer L, Repp F, Shipov A, Weiner S, Currey JD, Shahar R. Remodeling in Bone Without Osteocytes: Billfish Challenge Bone Structure–Function Paradigms. *Proceedings of the National Academy of Sciences*. 2014;111(45):16047–16052. doi:10.1073/pnas.1412372111

32. Mattia C, Di Bussolo E, Coluzzi F. Non-Analgesic Effects of Opioids: The Interaction of Opioids with Bone and Joints. *Current Pharmaceutical Design*. 2012;18(37):6005–6009. doi:10.2174/138161212803582487
33. Roux W. Beiträge zur morphologie der funktionellen anpassung. 3. Beschreibung und erläuterung einer knoekernen kneigelenksankylose. *Archiv für Anatomie, Physiologie und Wissenschaftliche Medicin*. 1885;ch 6:120–158.
34. Wolff J. *The Law of Bone Remodelling*. 1st ed. Heidelberg, Germany: Springer Berlin, Heidelberg; 1986. <https://link.springer.com/book/10.1007/978-3-642-71031-5>
35. Frost HM. The Mechanostat - A Proposed Pathogenic Mechanism of Osteoporoses and the Bone Mass Effects of Mechanical and Nonmechanical Agents. *Bone and Mineral*. 1987;2(2):73–85.
36. Frost HM. Changing Concepts in Skeletal Physiology: Wolff’s Law, The Mechanostat, and The “Utah Paradigm.” *American Journal of Human Biology*. 1998;10(5):599–605. doi:10.1002/(SICI)1520-6300(1998)10:5<599::AID-AJHB6>3.0.CO;2-9
37. Ruff C, Holt B, Trinkaus E. Who’s Afraid of the Big Bad Wolff?: “Wolff’s Law” and Bone Functional Adaptation. *American Journal of Physical Anthropology*. 2006;129(4):484–498. doi:10.1002/ajpa.20371
38. Frost HM. A 2003 Update of Bone Physiology and Wolff’s Law for Clinicians. *The Angle Orthodontist*. 2004;74(1):3–15. doi:10.1043/0003-3219(2004)074<0003:AUOBPA>2.0.CO;2
39. Turner CH. Toward a Mathematical Description of Bone Biology: The Principle of Cellular Accommodation. *Calcified Tissue International*. 1999;65(6):466–471. doi:10.1007/s002239900734
40. Crowder CM, Pinto DC, Andronowski JM, Dominguez VM. Theory and Histological Methods. In: Boyd Jr. CC, Boyd DC, editors. *Forensic Anthropology Theoretical Framework and Scientific Basis*. 1st ed. Hoboken, NJ: John Wiley & Sons, Ltd; 2018. p. 113–126.
41. Martin RB. Functional Adaptation and Fragility of the Skeleton. In: Agarwal SC, Stout SD, editors. *Bone Loss and Osteoporosis: An Anthropological Perspective*. Boston, MA: Springer US; 2003. p. 121–138. https://doi.org/10.1007/978-1-4419-8891-1_8. doi:10.1007/978-1-4419-8891-1_8
42. Raisz LG. Physiology and Pathophysiology of Bone Remodeling. *Clinical Chemistry*. 1999;45(8):1353–1358.

43. Boshra V. Evaluation of Osteoporosis Risk Associated with Chronic Use of Morphine, Fentanyl and Tramadol in Adult Female Rats. *Current Drug Safety*. 2011;6(3):159–163. doi:info:doi/10.2174/157488611797579267
44. Silva BC, Bilezikian JP. Parathyroid Hormone: Anabolic and Catabolic Actions on the Skeleton. *Current Opinion in Pharmacology*. 2015;22:41–50. (Respiratory • Musculoskeletal). doi:10.1016/j.coph.2015.03.005
45. Carter PH, Schipani E. The Roles of Parathyroid Hormone and Calcitonin in Bone Remodeling: Prospects for Novel Therapeutics. *Endocrine, Metabolic & Immune Disorders - Drug Targets(Formerly Current Drug Targets - Immune, Endocrine & Metabolic Disorders)*. 2006;6(1):59–76. doi:10.2174/187153006776056666
46. Advokat CD, Comaty JE, Julien RM. Opioid Analgesics. In: Julien’s Primer of Drug Action. 13th ed. New York, NY: Worth Publishers; 2014. p. 297–334.
47. Hall JE. Guyton and Hall Textbook of Medical Physiology. 12th edition. Philadelphia, Pa: Saunders; 2010.
48. National Institute on Drug. Misuse of Prescription Drugs Research Report. National Institutes of Health; 2020. <https://www.drugabuse.gov/publications/research-reports/misuse-prescription-drugs/overview>
49. Thakur NA, DeBoyace SD, Margulies BS. Antagonism of the Met5-enkephalin-opioid growth factor receptor-signaling axis promotes MSC to differentiate into osteoblasts. *Journal of Orthopaedic Research: Official Publication of the Orthopaedic Research Society*. 2015;34(7):1195–1205. doi:10.1002/jor.23135
50. Tanaka K, Kondo H, Hamamura K, Togari A. Systemic Administration of Low-Dose Naltrexone Increases Bone Mass due to Blockade of Opioid Growth Factor Receptor Signaling in Mice Osteoblasts. *Life Sciences*. 2019;224:232–240. doi:10.1016/j.lfs.2019.03.069
51. Benyamin R, Trescot AM, Datta S, Buenaventura R, Adlaka R, Sehgal N, Glaser SE, Vallejo R. Opioid Complications and Side Effects. *Pain Physician*. 2008;11(2S):S105–S120.
52. Brennan MJ. The Effect of Opioid Therapy on Endocrine Function. *The American Journal of Medicine*. 2013;126(3, Supplement 1):S12–S18. (Opioids in Chronic Pain: Evolving Best Practice Strategies). doi:10.1016/j.amjmed.2012.12.001
53. Coluzzi F, Scerpa MS, Centanni M. The Effect of Opiates on Bone Formation and Bone Healing. *Current Osteoporosis Reports*. 2020;18:325–335. doi:10.1007/s11914-020-00585-4

54. Coluzzi F, Pergolizzi J, Raffa RB, Mattia C. The Unsolved Case of “Bone-Impairing Analgesics”: The Endocrine Effects of Opioids on Bone Metabolism. *Therapeutics and Clinical Risk Management*. 2015;11:515–523. doi:10.2147/TCRM.S79409
55. Yoshida K, Yu Z, Greendale GA, Ruppert K, Lian Y, Tedeschi SK, Lin T-C, Haneuse S, Glynn RJ, Hernández-Díaz S, et al. Effects of Analgesics on Bone Mineral Density: A Longitudinal Analysis of the Prospective SWAN Cohort with Three-Group Matching Weights. *Pharmacoepidemiology and Drug Safety*. 2017;27(2):182–190. doi:10.1002/pds.4362
56. Pedrazzoni M, Vescovi PP, Maninetti L, Michelini M, Zaniboni G, Pioli G, Costi D, Alfano FS, Passeri M. Effects of Chronic Heroin Abuse on Bone and Mineral Metabolism. *European Journal of Endocrinology*. 1993;129(1):42–45. doi:10.1530/acta.0.1290042
57. Vestergaard P, Rejnmark L, Mosekilde L. Fracture Risk Associated with the Use of Morphine and Opiates. *Journal of Internal Medicine*. 2006;260(1):76–87. doi:10.1111/j.1365-2796.2006.01667.x
58. Florencio-Silva R, Sasso GR da S, Sasso-Cerri E, Simões MJ, Cerri PS. Biology of Bone Tissue: Structure, Function, and Factors That Influence Bone Cells. *BioMed Research International*. 2015;2015:e421746. doi:10.1155/2015/421746
59. Robling A. Mechanical adaptation. In: Burr D, Allen M, editors. *Basic and Applied Bone Biology*. London, UK: Academic Press; 2014. p. 175–203.
60. Komori T. Functions of the osteocyte network in the regulation of bone mass. *Cell and Tissue Research*. 2013;352(2):191–198. doi:10.1007/s00441-012-1546-x
61. Robling AG, Niziolek PJ, Baldrige LA, Condon KW, Allen MR, Alam I, Mantila SM, Gluhak-Heinrich J, Bellido TM, Harris SE, et al. Mechanical stimulation of bone in vivo reduces osteocyte expression of Sost/sclerostin. *The Journal of Biological Chemistry*. 2008;283(9):5866–5875. doi:10.1074/jbc.M705092200
62. Demontiero O, Vidal C, Duque G. Aging and bone loss: new insights for the clinician. *Therapeutic Advances in Musculoskeletal Disease*. 2012;4(2):61–76. doi:10.1177/1759720X11430858
63. Zebaze R, Seeman E. Cortical Bone: A Challenging Geography. *Journal of Bone and Mineral Research*. 2015;30(1):24–29. doi:10.1002/jbmr.2419
64. Ashique AM, Hart LS, Thomas CDL, Clement JG, Pivonka P, Carter Y, Mousseau DD, Cooper DML. Lacunar-Canalicular Network in Femoral Cortical Bone is Reduced in Aged Women and is Predominantly Due to a Loss of Canalicular Porosity. *Bone Reports*. 2017;7:9–16. doi:10.1016/j.bonr.2017.06.002

65. Bach-Gansmo FL, Brüel A, Jensen MV, Ebbesen EN, Birkedal H, Thomsen JS. Osteocyte Lacunar Properties and Cortical Microstructure in Human Iliac Crest as a Function of Age and Sex. *Bone*. 2016;91:11–19. doi:10.1016/j.bone.2016.07.003
66. Hunter RL, Agnew AM. Intrasketal variation in human cortical osteocyte lacunar density: Implications for bone quality assessment. *Bone Reports*. 2016;5:252–261. doi:10.1016/j.bonr.2016.09.002
67. Carter Y, Thomas CDL, Clement JG, Cooper DML. Femoral Osteocyte Lacunar Density, Volume and Morphology in Women Across the Lifespan. *Journal of Structural Biology*. 2013;183(3):519–526. doi:10.1016/j.jsb.2013.07.004
68. Carter Y, Suchorab JL, Thomas CDL, Clement JG, Cooper DML. Normal Variation in Cortical Osteocyte Lacunar Parameters in Healthy Young Males. *Journal of Anatomy*. 2014;225(3):328–336. doi:10.1111/joa.12213
69. Torres-Lagares D, Tulasne J-F, Pouget C, Llorens A, Saffar J-L, Lesclous P. Structure and remodelling of the human parietal bone: an age and gender histomorphometric study. *Journal of Cranio-Maxillo-Facial Surgery*. 2010;38(5):325–330. doi:10.1016/j.jcms.2009.07.012
70. Vashishth D, Verborgt O, Divine G, Schaffler MB, Fyhrie DP. Decline in osteocyte lacunar density in human cortical bone is associated with accumulation of microcracks with age. *Bone*. 2000;26(4):375–380. doi:10.1016/S8756-3282(00)00236-2
71. Milovanovic P, Zimmermann EA, Hahn M, Djonic D, Püschel K, Djuric M, Amling M, Busse B. Osteocytic Canalicular Networks: Morphological Implications for Altered Mechanosensitivity. *ACS Nano*. 2013;7(9):7542–7551. doi:10.1021/nn401360u
72. Andronowski JM, Crowder C, Soto Martinez M. Recent Advancements in the Analysis of Bone Microstructure: New Dimensions in Forensic Anthropology. *Forensic Sciences Research*. 2018;3(4):278–293. doi:10.1080/20961790.2018.1483294
73. Cooper DML, Kawalilak CE, Harrison K, Johnston BD, Johnston JD. Cortical Bone Porosity: What Is It, Why Is It Important, and How Can We Detect It? *Current Osteoporosis Reports*. 2016;14(5):187–198. doi:10.1007/s11914-016-0319-y
74. Ciani C, Doty SB, Fritton SP. An Effective Histological Staining Process to Visualize Bone Interstitial Fluid Space Using Confocal Microscopy. *Bone*. 2009;44(5):1015–1017. doi:10.1016/j.bone.2009.01.376

75. Dong P, Hauptert S, Hesse B, Langer M, Gouttenoire P-J, Bousson V, Peyrin F. 3D Osteocyte Lacunar Morphometric Properties and Distributions in Human Femoral Cortical Bone Using Synchrotron Radiation Micro-CT Images. *Bone*. 2014;60:172–185. doi:10.1016/j.bone.2013.12.008
76. Crowder C, Heinrich J, Stout SD. Rib Histomorphometry for Adult Age Estimation. In: Bell LS, editor. *Forensic Microscopy for Skeletal Tissues: Methods and Protocols*. New York: Humana Press; Springer; 2012. p. 109–127. (Methods in Molecular Biology).
77. Andronowski JM, Davis RA, Holyoke CW. A Sectioning, Coring, and Image Processing Guide for High-Throughput Cortical Bone Sample Procurement and Analysis for Synchrotron Micro-CT. *Journal of Visualized Experiments*. 2020:e61081. doi:http://dx.doi.org/10.3791/61081
78. Wysokinski TW, Chapman D, Adams G, Renier M, Suortti P, Thomlinson W. Beamlines of the Biomedical Imaging and Therapy Facility at the Canadian Light Source - Part 3. *Nuclear Instruments and Methods in Physics Research Section A: Accelerators, Spectrometers, Detectors and Associated Equipment*. 2015;775:1–4. doi:10.1016/j.nima.2014.11.088
79. Faragó T, Gasilov S, Emslie I, Zuber M, Helfen L, Vogelgesang M, Baumbach T. Tofu: A Fast, Versatile and User-Friendly Image Processing Toolkit for Computed Tomography. *Journal of Synchrotron Radiation*. 2022 [accessed 2022 Apr 13];29(3). <https://journals.iucr.org/s/issues/2022/03/00/tv5034/>. doi:10.1107/S160057752200282X
80. Schindelin J, Arganda-Carreras I, Frise E, Kaynig V, Longair M, Pietzsch T, Preibisch S, Rueden C, Saalfeld S, Schmid B, et al. Fiji: An Open-Source Platform for Biological-Image Analysis. *Nature Methods*. 2012;9(7):676–682. doi:10.1038/nmeth.2019
81. Sokal RR, Rohlf FJ. *Linear Regression*. In: *Biometry: The Principles and Practices of Statistics in Biological Research*. 3rd edition. New York: W. H. Freeman; 1994. p. 451–554.
82. Zar JH. *Multiple Regression and Correlation*. In: *Biostatistical Analysis*. 5th ed. Upper Saddle River, NJ: Pearson Education; 2010. p. 419–457.
83. Fox J. *Dummy-Variable Regression*. In: *Applied Regression Analysis and Generalized Linear Models*. 3rd ed. London, UK: SAGE Publications; 2016. p. 128–152.

84. Knief U, Forstmeier W. Violating the Normality Assumption may be the Lesser of Two Evils. *Behavior Research Methods*. 2021;53(6):2576–2590. doi:10.3758/s13428-021-01587-5
85. Rochon J, Gondan M, Kieser M. To Test or Not to Test: Preliminary Assessment of Normality When Comparing Two Independent Samples. *BMC Medical Research Methodology*. 2012;12:81. doi:10.1186/1471-2288-12-81
86. Zar JH. Simple Linear Regression. In: *Biostatistical Analysis*. 5th ed. Upper Saddle River, NJ: Pearson Education; 2010. p. 328–362.
87. Lumley T, Diehr P, Emerson S, Chen L. The Importance of the Normality Assumption in Large Public Health Data Sets. *Annual Review of Public Health*. 2002;23(1):151–169. doi:10.1146/annurev.publhealth.23.100901.140546
88. Sokal RR, Rohlf FJ. *Miscellaneous Methods*. In: *Biometry: The Principles and Practices of Statistics in Biological Research*. 3rd edition. New York: W. H. Freeman; 1994. p. 794–832.
89. Fox J. Bootstrapping Regression Models. In: *Applied Regression Analysis and Generalized Linear Models*. 3rd ed. London, UK: SAGE Publications; 2016. p. 647–668.
90. Agnew AM, Murach MM, Dominguez VM, Sreedhar A, Misicka E, Harden A, Bolte JH, Kang Y-S, Stammen J, Moorhouse K. Sources of Variability in Structural Bending Response of Pediatric and Adult Human Ribs in Dynamic Frontal Impacts. *Stapp Car Crash Journal*. 2018;62:119–192.
91. Bousson V, Meunier A, Bergot C, Vicaut É, Rocha MA, Morais MH, Laval-Jeantet A-M, Laredo J-D. Distribution of Intracortical Porosity in Human Midfemoral Cortex by Age and Gender. *Journal of Bone and Mineral Research*. 2001;16(7):1308–1317. doi:10.1359/jbmr.2001.16.7.1308
92. Cooper DML, Thomas CDL, Clement JG, Turinsky AL, Sensen CW, Hallgrímsson B. Age-Dependent Change in the 3D Structure of Cortical Porosity at the Human Femoral Midshaft. *Bone*. 2007;40(4):957–965. doi:10.1016/j.bone.2006.11.011
93. Stein MS, Feik SA, Thomas CDL, Clement JG, Wark JD. An Automated Analysis of Intracortical Porosity in Human Femoral Bone Across Age. *Journal of Bone and Mineral Research*. 1999;14(4):624–632. doi:10.1359/jbmr.1999.14.4.624
94. Cohen J. *Statistical Power Analysis for the Behavioral Sciences*. 2nd ed. New York: Routledge; 1988. doi:10.4324/9780203771587

95. Thomas CDL, Feik SA, Clement JG. Increase in Pore Area, and Not Pore Density, is the Main Determinant in the Development of Porosity in Human Cortical Bone. *Journal of Anatomy*. 2006;209(2):219–230. doi:10.1111/j.1469-7580.2006.00589.x
96. Thomas CDL, Feik SA, Clement JG. Regional variation of intracortical porosity in the midshaft of the human femur: age and sex differences. *Journal of Anatomy*. 2005;206(2):115–125. doi:10.1111/j.1469-7580.2005.00384.x
97. Mullender MG, Huiskes R, Versleyen H, Buma P. Osteocyte Density and Histomorphometric Parameters in Cancellous Bone of the Proximal Femur in Five Mammalian Species. *Journal of Orthopaedic Research*. 1996;14(6):972–9. doi:10.1002/jor.1100140618
98. Busse B, Djonic D, Milovanovic P, Hahn M, Püschel K, Ritchie RO, Djuric M, Amling M. Decrease in the osteocyte lacunar density accompanied by hypermineralized lacunar occlusion reveals failure and delay of remodeling in aged human bone. *Aging Cell*. 2010;9(6):1065–1075. doi:10.1111/j.1474-9726.2010.00633.x
99. Vashishth D, Gibson G, Kimura J, Schaffler MB, Fyhrie DP. Determination of Bone Volume by Osteocyte Population. *The Anatomical Record*. 2002;267(4):292–295. doi:10.1002/ar.10114
100. Tomkinson A, Reeve J, Shaw RW, Noble BS. The Death of Osteocytes via Apoptosis Accompanies Estrogen Withdrawal in Human Bone. *The Journal of Clinical Endocrinology & Metabolism*. 1997;82(9):3128–3135. doi:10.1210/jcem.82.9.4200
101. Tomkinson A, Gevers EF, Wit JM, Reeve J, Noble BS. The Role of Estrogen in the Control of Rat Osteocyte Apoptosis. *Journal of Bone and Mineral Research: The Official Journal of the American Society for Bone and Mineral Research*. 1998;13(8):1243–1250. doi:10.1359/jbmr.1998.13.8.1243
102. Almeida M, Han L, Martin-Millan M, Plotkin LI, Stewart SA, Roberson PK, Kousteni S, O'Brien CA, Bellido T, Parfitt AM, et al. Skeletal Involution by Age-associated Oxidative Stress and Its Acceleration by Loss of Sex Steroids*. *Journal of Biological Chemistry*. 2007;282(37):27285–27297. doi:10.1074/jbc.M702810200
103. Qiu S, Rao DS, Palnitkar S, Parfitt AM. Age and Distance from the Surface but not Menopause Reduce Osteocyte density in Human Cancellous Bone. *Bone*. 2002;31(2):313–318. doi:10.1016/S8756-3282(02)00819-0

104. Cordey J, Gautier E. Strain Gauges Used in the Mechanical Testing of Bones Part III: Strain Analysis, Graphic Determination of the Neutral Axis. *Injury*. 1999;30:SA21–SA25. doi:10.1016/S0020-1383(99)00122-9
105. Schurman CA, Verbruggen SW, Alliston T. Disrupted Osteocyte Connectivity and Pericellular Fluid Flow in Bone with Aging and Defective TGF- β Signaling. *Proceedings of the National Academy of Sciences*. 2021;118(25):e2023999118. doi:10.1073/pnas.2023999118
106. Maggiano IS, Maggiano CM, Clement JG, Thomas CDL, Carter Y, Cooper DML. Three-Dimensional Reconstruction of Haversian Systems in Human Cortical Bone Using Synchrotron Radiation-Based Micro-CT: Morphology and Quantification of Branching and Transverse Connections Across Age. *Journal of Anatomy*. 2016;228(5):719–732. doi:10.1111/joa.12430
107. Stout SD, Brunsden BS, Hildebolt CF, Commean PK, Smith KE, Tappen NC. Computer-Assisted 3D Reconstruction of Serial Sections of Cortical Bone to Determine the 3D Structure of Osteons. *Calcified Tissue International*. 1999;65(4):280–284. doi:10.1007/s002239900699
108. Cooper DML, Turinsky A, Sensen C, Hallgrímsson B. Effect of Voxel Size on 3D micro-CT Analysis of Cortical Bone Porosity. *Calcified Tissue International*. 2007;80(3):211–219. doi:10.1007/s00223-005-0274-6
109. National Institutes of Health. Opioid Overdose Crisis. National Institute on Drug Abuse. 2021 Mar 11 [accessed 2021 Mar 16]. <https://www.drugabuse.gov/drug-topics/opioids/opioid-overdose-crisis>
110. National Institutes of Health. Opioid Summaries by State. National Institute on Drug Abuse. 2020 Apr 16 [accessed 2021 Mar 16]. <https://www.drugabuse.gov/drug-topics/opioids/opioid-summaries-by-state>
111. Kanis JA. Diagnosis of Osteoporosis and Assessment of Fracture Risk. *The Lancet*. 2002;359(9321):1929–1936. doi:10.1016/S0140-6736(02)08761-5
112. Pérez-Castrillón JL, Olmos JM, Gómez JJ, Barrallo A, Riancho JA, Perera L, Valero C, Amado JA, González-Macías J. Expression of Opioid Receptors in Osteoblast-Like MG-63 Cells, and Effects of Different Opioid Agonists on Alkaline Phosphatase and Osteocalcin Secretion by These Cells. *Neuroendocrinology*. 2000;72(3):187–194. doi:10.1159/000054586
113. Ding Z, Chen Y, Wang X, Zhou X, Xu Y, Ma Z, Sun Y, Jiang M. A Comparison of Bone Quality and its Determinants in Young Opioid-Dependent Women with Healthy Control Group. *Drug and Alcohol Dependence*. 2017;175:232–236. doi:10.1016/j.drugalcdep.2017.02.010

114. Jain N, Himed K, Toth JM, Briley KC, Phillips FM, Khan SN. Opioids Delay Healing of Spinal Fusion: A Rabbit Posterolateral Lumbar Fusion Model. *The Spine Journal*. 2018;18(9):1659–1668. doi:10.1016/j.spinee.2018.04.012
115. Jee WSS, Yao W. Overview: Animal Models of Osteopenia and Osteoporosis. *Journal of Musculoskeletal and Neuronal Interactions*. 2001;1(3):193–207.
116. Reinwald S, Burr D. Review of Nonprimate, Large Animal Models for Osteoporosis Research. *Journal of Bone and Mineral Research*. 2008;23(9):1353–1368. doi:10.1359/jbmr.080516
117. Pearce A, Richards R, Milz S, Schneider E, Pearce S. Animal Models for Implant Biomaterial Research in Bone: A Review. *European Cells and Materials*. 2007;13:1–10. doi:10.22203/eCM.v013a01
118. Turner AS. Animal Models of Osteoporosis--Necessity and Limitations. *European Cells and Materials*. 2001;1:66–81. doi:10.22203/eCM.v001a08
119. Recker RR, Kimmel DB, Dempster D, Weinstein RS, Wronski TJ, Burr DB. Issues in Modern Bone Histomorphometry. *Bone*. 2011;49(5):955–964. doi:10.1016/j.bone.2011.07.017
120. Castañeda S, Largo R, Calvo E, Rodríguez-Salvanés F, Marcos ME, Díaz-Curiel M, Herrero-Beaumont G. Bone Mineral Measurements of Subchondral and Trabecular Bone in Healthy and Osteoporotic Rabbits. *Skeletal Radiology*. 2006;35(1):34–41. doi:10.1007/s00256-005-0022-z
121. Baofeng L, Zhi Y, Bei C, Guolin M, Qingshui Y, Jian L. Characterization of a Rabbit Osteoporosis Model Induced by Ovariectomy and Glucocorticoid. *Acta Orthopaedica*. 2010;81(3):396–401. doi:10.3109/17453674.2010.483986
122. Castañeda S, Calvo E, Largo R, González-González R, de la Piedra C, Díaz-Curiel M, Herrero-Beaumont G. Characterization of a New Experimental Model of Osteoporosis in Rabbits. *Journal of Bone and Mineral Metabolism*. 2008;26(1):53–59. doi:10.1007/s00774-007-0797-1
123. United States Department of Agriculture. Animal Welfare Act and Animal Welfare Regulations. 2020 [accessed 2021 Feb 15]. https://www.aphis.usda.gov/animal_welfare/downloads/AC_BlueBook_AWA_508_comp_version.pdf
124. Moore J. Final Report on the Safety Assessment of Myristyl Myristate and Isopropyl Myristate. *Journal of the American College of Toxicology*. 1982;1(4):55–80. doi:10.3109/10915818209021261

125. Foley PL, Henderson AL, Bissonette EA, Wimer GR, Feldman SH. Evaluation of Fentanyl Transdermal Patches in Rabbits: Blood Concentrations and Physiologic Response. *Comparative Medicine*. 2001;51(3):239–244.
126. Harrison KD, Hiebert BD, Panahifar A, Andronowski JM, Ashique AM, King GA, Arnason T, Swekla KJ, Pivonka P, Cooper DM. Cortical Bone Porosity in Rabbit Models of Osteoporosis. *Journal of Bone and Mineral Research*. 2020;35(11):2211–2228. doi:<https://doi.org/10.1002/jbmr.4124>
127. Bruker microCT. Method Note MCT-124: Auto Separation of Metaphyseal Trabecular from Cortical Bone Using a Morphological Escalator. 2019 [accessed 2019 Jul 23].
<https://s3.amazonaws.com/BrukerDocuments/Files/Uploading/c0795ad1-46b4-4deb-b8fc-5e41f643ebd1/mn124%20trab-cort%20bone%20auto-separation%20with%20the%20morphological%20escalator.pdf?AWSAccessKeyId=AKIAJ6LSNGMJIL4S5VCQ&Expires=1617997121&Signature=d2%2FaiEqilPJyvOJ3JXh11PrfVA0%3D>
128. Andersen HB, Christensen B, Findlay JWA, Jansen JA. Pharmacokinetics of Intravenous, Intrathecal and Epidural Morphine and Fentanyl in the Goat. *Acta Anaesthesiologica Scandinavica*. 1986;30(5):393–399. doi:10.1111/j.1399-6576.1986.tb02437.x
129. Hess R, Stiebler G, Herz A. Pharmacokinetics of Fentanyl in Man and the Rabbit. *European Journal of Clinical Pharmacology*. 1972;4(3):137–141. doi:10.1007/BF00561135
130. Drewes AM, Jensen RD, Nielsen LM, Droney J, Christrup LL, Arendt-Nielsen L, Riley J, Dahan A. Differences Between Opioids: Pharmacological, Experimental, Clinical and Economical Perspectives. *British Journal of Clinical Pharmacology*. 2013;75(1):60–78. doi:10.1111/j.1365-2125.2012.04317.x
131. Cote LR, Gordon RG, Randell CE, Schmitt J, Marvin H. Analysis of Variance. In: *Statistics LibreTexts*. 1st ed. St. Louis, MO: Open Educational Resources Collection; 2021. p. 156–174.
<https://irl.umsl.edu/cgi/viewcontent.cgi?article=1024&context=oer>
132. Andronowski JM, Schuller AJ, Cole ME, LaMarca AR, Davis RA, Tubo GR. Rabbits (*Oryctolagus cuniculus*) as a Model System for Longitudinal Experimental Opioid Treatments: Implications for Orthopedic and Biomedical Research. *Osteology*. 2021;1(4):225–237. doi:10.3390/osteology1040021

133. Bataille C, Mauprivez C, Hay E, Baroukh B, Brun A, Chaussain C, Marie PJ, Saffar J-L, Cherruau M. Different Sympathetic Pathways Control the Metabolism of Distinct Bone Envelopes. *Bone*. 2012;50(5):1162–1172. doi:10.1016/j.bone.2012.01.023
134. Uthoff H, Jaworski Z. Bone Loss in Response to Long-Term Immobilisation. *The Journal of Bone and Joint Surgery. British volume*. 1978;60-B(3):420–429. doi:10.1302/0301-620X.60B3.681422
135. Frost HM. Bone Mass and the Mechanostat - A Proposal. *Anatomical Record*. 1987;219(1):1–9. doi:DOI 10.1002/ar.1092190104
136. Cooper MS, Seibel MJ, Zhou H. Glucocorticoids, Bone and Energy Metabolism. *Bone*. 2016;82:64–68. (Metabolism and Diabetes Mellitus - From Basic Science to Clinical Translation). doi:10.1016/j.bone.2015.05.038
137. Zhou H, Cooper MS, Seibel MJ. Endogenous Glucocorticoids and Bone. *Bone Research*. 2013;1(1):107–119. doi:10.4248/BR201302001
138. Balodimos S, Nikolaou K, Njau S, Karamouzis M, Kovatsi L. The Effect of Opioid Dependence on Conventional and Novel Biochemical Parameters of Bone Metabolism. *The American Journal of Drug and Alcohol Abuse*. 2015;41(6):535–540. doi:10.3109/00952990.2015.1068321
139. Black SL, Vanderwolf CH. Thumping Behavior in the Rabbit. *Physiology & Behavior*. 1969;4(4):445–449. doi:10.1016/0031-9384(69)90134-6
140. Reynolds RM, Dennison EM, Walker BR, Syddall HE, Wood PJ, Andrew R, Phillips DI, Cooper C. Cortisol Secretion and Rate of Bone Loss in a Population-Based Cohort of Elderly Men and Women. *Calcified Tissue International*. 2005;77(3):134–138. doi:10.1007/s00223-004-0270-2
141. Takahashi M, Wehrli FW, Hilaire L, Zemel BS, Hwang SN. In vivo NMR Microscopy Allows Short-Term Serial Assessment of Multiple Skeletal Implications of Corticosteroid Exposure. *Proceedings of the National Academy of Sciences*. 2002;99(7):4574–4579. doi:10.1073/pnas.062037499
142. Yao W, Cheng Z, Pham A, Busse C, Zimmermann EA, Ritchie RO, Lane NE. Glucocorticoid-Induced Bone Loss in Mice can be Reversed by the Actions of Parathyroid Hormone and Risedronate on Different Pathways for Bone Formation and Mineralization. *Arthritis & Rheumatism*. 2008;58(11):3485–3497. doi:10.1002/art.23954

143. Bouvard B, Gallois Y, Legrand E, Audran M, Chappard D. Glucocorticoids Reduce Alveolar and Trabecular Bone in Mice. *Joint Bone Spine*. 2013;80(1):77–81. doi:10.1016/j.jbspin.2012.01.009
144. Lane NE, Yao W, Balooch M, Nalla RK, Balooch G, Habelitz S, Kinney JH, Bonewald LF. Glucocorticoid-Treated Mice Have Localized Changes in Trabecular Bone Material Properties and Osteocyte Lacunar Size That Are Not Observed in Placebo-Treated or Estrogen-Deficient Mice. *Journal of Bone and Mineral Research*. 2006;21(3):466–476. doi:10.1359/JBMR.051103
145. LoCascio V, Bonucci E, Imbimbo B, Ballanti P, Adami S, Milani S, Tartarotti D, DellaRocca C. Bone Loss in Response to Long-Term Glucocorticoid Therapy. *Bone and Mineral*. 1990;8(1):39–51. doi:10.1016/0169-6009(91)90139-Q
146. Hahn TJ, Boisseau VC, Avioli LV. Effect of Chronic Corticosteroid Administration on Diaphyseal and Metaphyseal Bone Mass. *The Journal of Clinical Endocrinology & Metabolism*. 1974;39(2):274–282. doi:10.1210/jcem-39-2-274
147. Nelson RE, Nebeker JR, Sauer BC, LaFleur J. Factors Associated with Screening or Treatment Initiation Among Male United States Veterans at Risk for Osteoporosis Fracture. *Bone*. 2012;50(4):983–988. doi:10.1016/j.bone.2011.11.014
148. Canalis E, Delany AM. Mechanisms of Glucocorticoid Action in Bone. *Annals of the New York Academy of Sciences*. 2002;966(1):73–81. doi:10.1111/j.1749-6632.2002.tb04204.x
149. Lane NE, Lukert B. The Science and Therapy of Glucocorticoid-Induced Bone Loss. *Endocrinology and Metabolism Clinics of North America*. 1998;27(2):465–483. doi:10.1016/S0889-8529(05)70017-7
150. Andronowski JM, Davis RA, Cole ME. Investigating the Impact of Opioid Abuse on Intracortical Porosity and Bone Cellular Density: A Synchrotron-Radiation Micro-Computed Tomography (SR μ CT) Approach. In: *Proceedings of the American Academy of Forensic Sciences*. Anaheim, CA; 2020. p. 102. https://aafs.org/common/Uploaded%20files/Resources/Proceedings/2020_Proceedings.pdf
151. Kaweblum M, Aguilar MDC, Blancas E, Kaweblum J, Lehman WB, Grant AD, Strongwater AM. Histological and Radiographic Determination of the Age of Physeal Closure of the Distal Femur, Proximal Tibia, and Proximal Fibula of the New Zealand White Rabbit. *Journal of Orthopaedic Research*. 1994;12(5):747–749. doi:10.1002/jor.1100120519

152. Cacchioli A, Ravanetti F, Soliani L, Borghetti P. Preliminary Study on the Mineral Apposition Rate in distal femoral epiphysis of New Zealand White Rabbit at Skeletal Maturity. *Anatomia, Histologia, Embryologia*. 2012;41(3):163–169. doi:10.1111/j.1439-0264.2011.01119.x
153. Kilborn SH, Trudel G, Uhthoff H. Review of Growth Plate Closure Compared with Age at Sexual Maturity and Lifespan in Laboratory Animals. *Journal of the American Association for Laboratory Animal Science*. 2002;41(5):21–26.
154. Andronowski JM, Cole ME, Davis RA, Schuller AJ, LaMarca AR, Tubo GR. The Longitudinal Effects of Prolonged Opioid Use on Cortical Bone Remodeling in a Rabbit Model: Part I—Intraskelatal Variability and Regional Differences Detected Via Micro-Computed Tomography (Micro-CT). In: *Proceedings of the American Academy of Forensic Sciences*. Virtual; 2021. p. 62. https://aafs.org/common/Uploaded%20files/Meetings/2021%20Meeting/21Proceedings_Complete.pdf
155. Gushue DL, Houck J, Lerner AL. Rabbit Knee Joint Biomechanics: Motion Analysis and Modeling of Forces During Hopping. *Journal of Orthopaedic Research*. 2005;23(4):735–742. doi:10.1016/j.orthres.2005.01.005
156. Lanyon LE. Functional Strain as a Determinant for Bone Remodeling. *Calcified Tissue International*. 1984;36(1):S56–S61. doi:10.1007/BF02406134
157. Rubin CT, Lanyon LE. Regulation of Bone Mass by Mechanical Strain Magnitude. *Calcified Tissue International*. 1985;37(4):411–417. doi:10.1007/BF02553711
158. Bays TB. Geriatric Care of Rabbits, Guinea Pigs, and Chinchillas. *Veterinary Clinics: Exotic Animal Practice*. 2020;23(3):567–593. doi:10.1016/j.cvex.2020.05.006
159. Albert DL, Katzenberger MJ, Agnew AM, Kemper AR. A Comparison of Rib Cortical Bone Compressive and Tensile Material Properties: Trends with Age, Sex, and Loading Rate. *Journal of the Mechanical Behavior of Biomedical Materials*. 2021;122:104668. doi:10.1016/j.jmbbm.2021.104668
160. Currey JD. *The Mechanical Properties of Bone*. In: *Bones: Structure and Mechanics*. Princeton, NJ: Princeton University Press; 2002. p. 54–123.
161. Martin AD, McCulloch RG. Bone Dynamics: Stress, Strain and Fracture. *Journal of Sports Sciences*. 1987;5(2):155–163. doi:10.1080/02640418708729773
162. Boskey AL, Imbert L. Bone Quality Changes Associated with Aging and Disease: A Review. *Annals of the New York Academy of Sciences*. 2017;1410(1):93–106. doi:10.1111/nyas.13572

163. Skedros JG. Interpreting Load History in Limb-Bone Diaphyses: Important Considerations and Their Biomechanical Foundations. In: Stout SD, Crowder CM, editors. *Bone Histology: An Anthropological Perspective*. Boca Raton, FL; 2011. p. 153–221.
164. Reilly GC, Currey JD. The Effects of Damage and Microcracking on the Impact Strength of Bone. *Journal of Biomechanics*. 2000;33(3):337–343. doi:10.1016/s0021-9290(99)00167-0
165. Danova NA, Colopy SA, Radtke CL, Kalscheur VL, Markel MD, Vanderby R, McCabe RP, Escarcega AJ, Muir P. Degradation of Bone Structural Properties by Accumulation and Coalescence of Microcracks. *Bone*. 2003;33(2):197–205. doi:10.1016/S8756-3282(03)00155-8
166. Lambers FM, Bouman AR, Rinnac CM, Hernandez CJ. Microdamage Caused by Fatigue Loading in Human Cancellous Bone: Relationship to Reductions in Bone Biomechanical Performance. *PLOS ONE*. 2013;8(12):e83662. doi:10.1371/journal.pone.0083662
167. Zioupos P, Hansen U, Currey JD. Microcracking Damage and the Fracture Process in Relation to Strain Rate in Human Cortical Bone Tensile Failure. *Journal of Biomechanics*. 2008;41(14):2932–2939. doi:10.1016/j.jbiomech.2008.07.025
168. Unnanuntana A, Gladnick BP, Donnelly E, Lane JM. The Assessment of Fracture Risk. *The Journal of Bone and Joint Surgery. American volume*. 2010;92(3):743–753. doi:10.2106/JBJS.I.00919
169. Martin RB, Burr DB, Sharkey NA, Fyhrie DP. Fatigue and Fracture Resistance of Bone. In: *Skeletal Tissue Mechanics*. 2nd ed. New York: Springer-Verlag; 2015. p. 423–477. //www.springer.com/us/book/9781493930012
170. Alswat KA. Gender Disparities in Osteoporosis. *Journal of Clinical Medicine Research*. 2017;9(5):382–387. doi:10.14740/jocmr2970w
171. Currey JD. The Many Adaptations of Bone. *Journal of Biomechanics*. 2003;36(10):1487–1495. doi:10.1016/S0021-9290(03)00124-6
172. Ruff CB, Hayes WC. Subperiosteal Expansion and Cortical Remodeling of the Human Femur and Tibia with Aging. *Science*. 1982;217(4563):945–948. doi:10.1126/science.7112107
173. Chrastil J, Sampson C, Jones KB, Higgins TF. Postoperative Opioid Administration Inhibits Bone Healing in an Animal Model. *Clinical Orthopaedics and Related Research*. 2013;471(12):4076–4081. doi:10.1007/s11999-013-3232-z

174. Agnew AM, Stout SD. Brief communication: Reevaluating osteoporosis in human ribs: The role of intracortical porosity. *American Journal of Physical Anthropology*. 2012;148(3):462–466. doi:10.1002/ajpa.22048
175. Agnew AM, Schafman M, Moorhouse K, White SE, Kang Y-S. The Effect of Age on the Structural Properties of Human Ribs. *Journal of the Mechanical Behavior of Biomedical Materials*. 2015;41:302–314. doi:10.1016/j.jmbbm.2014.09.002
176. Albert DL, Kang Y-S, Agnew AM, Kemper AR. The Effect of Injurious Whole Rib Loading on Rib Cortical Bone Material Properties. In: 2018 IRCOBI Conference Proceedings. Athens, Greece: International Research Council on Biomechanics of Injury; 2018. p. 680–687. <http://www.ircobi.org/wordpress/downloads/irc18/pdf-files/96.pdf>
177. Sajjan SG, Barrett-Connor E, McHorney CA, Miller PD, Sen SS, Siris E. Rib Fracture as a Predictor of Future Fractures in Young and Older Postmenopausal Women: National Osteoporosis Risk Assessment (NORA). *Osteoporosis International*. 2012;23(3):821–828. doi:10.1007/s00198-011-1757-0
178. Adachi JD, Ioannidis G, Pickard L, Berger C, Prior JC, Joseph L, Hanley DA, Olszynski WP, Murray TM, Anastassiades T, et al. The Association Between Osteoporotic Fractures and Health-Related Quality of Life as Measured by the Health Utilities Index in the Canadian Multicentre Osteoporosis Study (CaMos). *Osteoporosis International*. 2003;14(11):895–904. doi:10.1007/s00198-003-1483-3
179. King T, Vardanyan A, Majuta L, Melemedjian O, Nagle R, Cress AE, Vanderah TW, Lai J, Porreca F. Morphine Treatment Accelerates Sarcoma-Induced Bone Pain, Bone Loss, and Spontaneous Fracture in a Murine Model of Bone Cancer. *Pain*. 2007;132(1):154–168. doi:10.1016/j.pain.2007.06.026
180. McCool FD, Loring SH, Mead J. Rib Cage Distortion During Voluntary and Involuntary Breathing Acts. *Journal of Applied Physiology*. 1985 May 1 [accessed 2022 Jun 10]. <https://journals.physiology.org/doi/10.1152/jappl.1985.58.5.1703>. doi:10.1152/jappl.1985.58.5.1703
181. Stout SD. The Use of Bone Histomorphometry in Skeletal Identification: The Case of Francisco Pizarro. *Journal of Forensic Science*. 1986;31(1):296–300. doi:10.1520/JFS11886J
182. Crowder C, Rosella L. Assessment of Intra- and Intercostal Variation in Rib Histomorphometry: Its Impact on Evidentiary Examination. *Journal of Forensic Sciences*. 2007;52(2):271–276. doi:10.1111/j.1556-4029.2007.00388.x

183. Stewart MC, McCormick LE, Goliath JR, Sciulli PW, Stout SD. A Comparison of Histomorphometric Data Collection Methods. *Journal of Forensic Sciences*. 2013;58(1):109–113. doi:<https://doi.org/10.1111/j.1556-4029.2012.02195.x>
184. Bertram JE, Biewener AA. Bone Curvature: Sacrificing Strength for Load Predictability? *Journal of Theoretical Biology*. 1988;131(1):75–92. doi:10.1016/s0022-5193(88)80122-x
185. Schultz RA, editor. Elastic Rock Rheology and Stress Concentration. In: *Geologic Fracture Mechanics*. Cambridge: Cambridge University Press; 2019. p. 27–74. <https://www.cambridge.org/core/books/geologic-fracture-mechanics/elastic-rock-rheology-and-stress-concentration/0CBA05A68EDEEEE4CCE34A56C9FF20C8>. doi:10.1017/9781316996737.002
186. Keaveny TM, Pinilla TP, Crawford RP, Kopperdahl DL, Lou A. Systematic and Random Errors in Compression Testing of Trabecular Bone. *Journal of Orthopaedic Research*. 1997;15(1):101–110. doi:10.1002/jor.1100150115
187. Lötsch J. Pharmacokinetic–Pharmacodynamic Modeling of Opioids. *Journal of Pain and Symptom Management*. 2005;29(5S):90–103. doi:10.1016/j.jpainsymman.2005.01.012
188. Harrison KD. A Novel In Vivo Synchrotron Radiation Micro-CT Imaging Platform For The Direct Tracking Of Remodeling Events In Cortical Bone [Thesis]. University of Saskatchewan; 2022. <https://harvest.usask.ca/handle/10388/13811>
189. Pearson OM, Lieberman DE. The Aging of Wolff’s “Law”: Ontogeny and Responses to Mechanical Loading in Cortical Bone. *American Journal of Physical Anthropology*. 2004;125(S39):63–99. doi:10.1002/ajpa.20155
190. Warden SJ, Gutschlag FR, Wajswelner H, Crossley KM. Aetiology of Rib Stress Fractures in Rowers. *Sports Medicine*. 2002;32(13):819–836. doi:10.2165/00007256-200232130-00002
191. Tommerup LJ, Raab DM, Crenshaw TD, Smith EL. Does Weight-Bearing Exercise Affect Non-Weight-Bearing Bone? *Journal of Bone and Mineral Research*. 1993;8(9):1053–1058. doi:10.1002/jbmr.5650080905
192. Leary S, Underwood W, Anthony R, Cartner S, Grandin T, Greenacre C, McCrackin MA, Meyer R, Miller D, Shearer J, et al. *AVMA Guidelines for the Euthanasia of Animals: 2020 Edition*. 2020.0.1. Schaumburg, IL: American Veterinary Medical Association; 2020. <https://www.avma.org/sites/default/files/2020-02/Guidelines-on-Euthanasia-2020.pdf>

193. Kamal B, Rashed R, Erasha A. Development of Sternum and Ribs in White New Zealand Rabbit (*Oryctolagus cuniculus*). *World's Veterinary Journal*. 2016;6(3):143–150. doi:10.5455/wvj.20160880
194. Kemper A, McNally C, Kennedy E, Manoogian S, Duma S. The Material Properties of Human Tibia Cortical Bone in Tension and Compression: Implications for the Tibia Index. Lyons, France: National Highway Traffic Safety Administration; 2007. <https://www-esv.nhtsa.dot.gov/Proceedings/20/07-0470-O.pdf>
195. Shunmugasamy VC, Gupta N, Coelho PG. High Strain Rate Response of Rabbit Femur Bones. *Journal of Biomechanics*. 2010;43(15):3044–3050. doi:10.1016/j.jbiomech.2010.06.034
196. Mitton D, Rumelhart C, Hans D, Meunier PJ. The Effects of Density and Test Conditions on Measured Compression and Shear Strength of Cancellous Bone from the Lumbar Vertebrae of Ewes. *Medical Engineering & Physics*. 1997;19(5):464–474. doi:10.1016/S1350-4533(97)00001-5
197. Grardel B, Sutter B, Flautre B, Viguiet E, Lavaste F, Hardouin P. Effects of Glucocorticoids on Skeletal Growth in Rabbits Evaluated by Dual-Photon Absorptiometry, Microscopic Connectivity and Vertebral Compressive Strength. *Osteoporosis International*. 1994;4(4):204–210. doi:10.1007/BF01623240
198. Cvetković VJ, Najman SJ, Rajković J, Žabar A, Vasiljević PJ, Djordjević LB, Trajanović M. A Comparison of the Microarchitecture of Lower Limb Long Bones Between Some Animal Models and Humans: A Review. *Veterinari Medicina*. 2013;58(7):339–351. doi:10.17221/6914-vetmed
199. Painting AL. A Study of the End Effects in Specimen Cores Under Compression Tests, with a View to the Elimination of These Effects. *Journal of the Southern African Institute of Mining and Metallurgy*. 1974;74(9):333–339. doi:10.10520/AJA0038223X_394
200. Kinjo M, Setoguchi S, Schneeweiss S, Solomon DH. Bone Mineral Density in Subjects Using Central Nervous System-Active Medications. *The American Journal of Medicine*. 2005;118(12):1414.e7-1414.e12. doi:10.1016/j.amjmed.2005.07.033
201. Stauber M, Rapillard L, van Lenthe GH, Zysset P, Müller R. Importance of Individual Rods and Plates in the Assessment of Bone Quality and Their Contribution to Bone Stiffness. *Journal of Bone and Mineral Research*. 2006;21(4):586–595. doi:10.1359/jbmr.060102

202. Wachter NJ, Krischak GD, Mentzel M, Sarkar MR, Ebinger T, Kinzl L, Claes L, Augat P. Correlation of Bone Mineral Density with Strength and Microstructural Parameters of Cortical Bone in vitro. *Bone*. 2002;31(1):90–95. doi:10.1016/S8756-3282(02)00779-2
203. Allen MR, Reinwald S, Burr DB. Alendronate Reduces Bone Toughness of Ribs without Significantly Increasing Microdamage Accumulation in Dogs Following 3 Years of Daily Treatment. *Calcified Tissue International*. 2008;82(5):354–360. doi:10.1007/s00223-008-9131-8
204. Zhao S, Arnold M, Ma S, Abel RL, Cobb JP, Hansen U, Boughton O. Standardizing Compression Testing for Measuring the Stiffness of Human Bone. *Bone & Joint Research*. 2018;7(8):524–538.
205. Carter DR, Hayes WC. The Compressive Behavior of Bone as a Two-Phase Porous Structure. *The Journal of Bone and Joint Surgery. American Volume*. 1977;59(7):954–962.
206. Linde F, Sørensen HCF. The Effect of Different Storage Methods on the Mechanical Properties of Trabecular Bone. *Journal of Biomechanics*. 1993;26(10):1249–1252. doi:10.1016/0021-9290(93)90072-M
207. Linde F, Hvid I. The Effect of Constraint on the Mechanical Behaviour of Trabecular Bone Specimens. *Journal of Biomechanics*. 1989;22(5):485–490. doi:10.1016/0021-9290(89)90209-1
208. Doube M, Kłosowski MM, Arganda-Carreras I, Cordelières FP, Dougherty RP, Jackson JS, Schmid B, Hutchinson JR, Shefelbine SJ. BoneJ: Free and Extensible Bone Image Analysis in ImageJ. *Bone*. 2010;47(6):1076–1079. doi:10.1016/j.bone.2010.08.023

APPENDICES

APPENDIX A

IMAGEJ MACRO FOR SR μ CT PORE EXTRACTION

Developed by Dr. Mary E. Cole

1. 32-bit reconstructed TIFF images are converted to 8-bit in FIJI.
2. Reconstructed datasets are loaded into DataViewer and aligned longitudinally, exported as BMP images.
3. Custom FIJI macro is run to isolate cortical spaces (lacunae and cortical pores) from reconstructed images:
 - a. User places a 1.2 mm ROI on a virtual stack of the dataset
 - i. After confirming ROI placement, macro performs the following steps automatically for each tomographic slice.
 - b. Contrast is enhanced by normalizing and equalizing the histogram with a pixel saturation of 0.3%
 - c. Brightness and contrast are auto-adjusted from the standard 0-255 pixel brightness values to the minimum and maximum pixel brightness in the reconstructed image.
 - d. The image is despeckled once to remove noise.

- e. An Intermodes threshold is applied to isolate spaces (lacunae and cortical pores) as white and bone as black.
 - f. Open spaces connected to the ROI edge are closed and filled.
 - g. The dataset, which now is a binarized stack of white spaces on black bone, is saved. The ROI is also saved as a filled white circle.
4. A custom macro in CTAnalyser is used to isolate cortical pores from lacunae, producing two separate datasets.
- a. Any space >2000 voxels (deemed a cortical pore) is isolated, sealed, and connections to adjacent lacunae are removed.
 - b. Any gap in the cortical pore smaller than 5 voxels is closed to produce a continuous pore.
 - c. Black specks in the 2D slices of each cortical pore ($<10,000$ pixels) are deemed mottled from soft tissue remnants and are filled in.
 - d. Lacunae are isolated by taken any space <2000 voxels.
 - e. Noise (objects <10 voxels) is removed from the lacunae.
 - f. Any inclusions on the 2D slices >100 pixels near the edge of the ROI were determined to be artifacts from ROI isolation and were removed, leaving only lacunae.
 - g. These voxel/pixel values for this macro were determined through trial and error, comparing the binarized output with the original reconstructed dataset.

5. A final rim correction is used to seal any remaining open pores connected to the edge of the ROI and removes ring artifacts from the binarized cortical pore and lacunae datasets.
 - a. The binarized pore and lacunae datasets are loaded separately and step 3f is repeated to seal any remaining open pores at the edge of the ROI
 - b. Ring artifacts (semi-circular defects from the scintillator of the SR μ CT system that persisted after ring correction during reconstruction) are removed.
 - i. For the cortical pore dataset, any particle with a size between 0-1000 pixels and more oblong (circularity value 0.0-0.2) is removed.
 - ii. For the lacunar dataset, the original grayscale dataset is copied, smoothed, and enhances the ring artifacts with auto MinError thresholding.
 - iii. Segments of the ring artifacts are connected through dilation/closing commands and isolated by circularity (0.0-0.3).
 - iv. Any lacunae trapped in this ring artifact are extracted with automatic Intermodos thresholding as in Step 3e, filtered by size to remove noise (>10 pixels) and high circularity (0.3-1.0).
 - v. Ring artifacts are removed from the lacunar dataset and any lacunae that were hidden in the ring artifact are added back in

- c. This macro saves refined datasets for both cortical pores and lacunae as well as datasets of artifacts removed from cortical pore and lacunar datasets to ensure what was removed was truly an artifact.
6. Refined datasets are automatically isolated in FIJI using Analyze Particles function and superimposed on the original grayscale reconstruction to ensure true pores or lacunae were not removed by mistake and that the refined datasets only include pores/lacunae.
7. Cortical pore and lacunae datasets are loaded into CTAnalyser separately and 3D analysis is processed for morphometric variables regarding size, connectivity, volume, and orientation. The ROI dataset saved in Step 3g is loaded to limit the bounds of analysis and correct for volume differences between specimens.

APPENDIX B

IMAGEJ/CTANALYSER MACRO FOR CLSM LCN EXTRACTION

Developed by: Dr. Mary E. Cole

ImageJ

1. Stitched dataset has contrast enhanced by normalizing and equalizing the histogram with a pixel saturation of 0.3%.
2. Background is subtracted from the dataset using a rolling ball radius of 50.
3. Bright and dark outlier speckles are removed to enhance object borders.
 - a. Outliers: radius = 2, threshold = 50
 - b. Unsharp mask: radius = 1, mask = 0.6
4. Auto-threshold using Phansalkar filter, ideal for low contrast images (radius = 15)
5. Despeckle function three times.

CTAnalyser

6. Isolated white speckles >100 voxels were determined to be noise and subsequently removed.
7. Morphological closing of gaps smaller than 3 voxels between adjacent 2D images.

APPENDIX C

STEP-DOWN BONFERRONI CORRECTIONS

1. Collect number of statistical tests run in the chapter (e.g., for Chapter III, there were 10 variables examined using ANOVAs)
2. Arrange original p -values from smallest to largest
3. Beginning with the lowest original p -value indicate the number of tests left to correct (e.g., for Chapter III, the smallest p -value is given the number 10, the second smallest is given the number 9. This continues until the final test [largest p -value] is given the number 1.)
4. Divide the original alpha ($\alpha = 0.05$, throughout this dissertation) by the number assigned to that test in Step 3 (e.g., the smallest p -value which was assigned 10, now has an alpha of 0.005 [0.05/10]).
5. Compare original p -value against this adjusted alpha determined for each test in Step 4. If the original p -value is less than this adjusted alpha, the test result remains significant.

Original p-value	# of Tests Remaining	Adjusted Alpha	Significant?
0.0000	10	0.0050	Yes
0.0000	9	0.0056	Yes
0.0000	8	0.0063	Yes
0.0000	7	0.0071	Yes
0.0000	6	0.0083	Yes
0.0003	5	0.0100	Yes
0.0016	4	0.0125	Yes
0.0021	3	0.0167	Yes
0.0045	2	0.0250	Yes
0.0940	1	0.0500	No

APPENDIX D

TRABECULAR ISOLATION TASKLIST IN CTANALYSER

Step	CTAnalyser Function	Settings Applied	Description
1	Thresholding	Automatic (Otsu), 2D space, dark background, apply to image	Applies a threshold to each 2D image in the dataset using Otsu method
2	Morphological Operations	Erosion in 2D space, round kernel, 1-pixel radius, apply to image	Diminishes the edge of each surface by 1 pixel in each 2D image. Severs any soft tissue remnant connections between fibula and tibia
3	Despeckle	Sweep in 3D space, remove all except the largest object, apply to image	Removes any objects that are not connected to the largest object (tibia). Removes the fibula from the dataset
4	Morphological Operations	Dilation in 2D space, round kernel, 2-pixel radius, apply to image	Expands the edge of each surface by 2 pixels in each 2D image. This undoes the erosion in Step 2 and adds one more pixel
5	Morphological Operations	Closing, in 2D space, round kernel, 1-pixel radius, apply to image	Connects any surfaces within 1 pixel of each other to fill in gaps between 2D slices
6	Morphological Operations	Erosion in 2D space, round kernel, 1-pixel radius, apply to image	Diminishes the edge of each surface by 1 pixel in each 2D image. Undoes the dilation from Step 4.

Step	CTAnalyser Function	Settings Applied	Description
7	Despeckle	Sweep in 3D space, remove all except the largest object, apply to image	Removes any objects that are not connected to the largest object (tibia). Removes noise amplified with the morphological operations in Steps 4-6
8	ROI Shrink-wrap	Shrink-wrap in 2D space, stretch over holes of 30 pixels or less.	Creates an ROI of the outer surface of the entire bone in each 2D image, ignoring holes less than 30 pixels
9	Bitwise Operations	Image = Image XOR Region of Interest	Inverts the image within the ROI, making medullary cavity an object and bone is viewed as background
10	Morphological Operations	Erosion in 2D space, round kernel, 2-pixel radius, apply to image	Removes portions of cortical shell that were within the bounds of the ROI
11	Despeckle	Sweep in 3D Space, remove all except the largest object, apply to image	Removes any remaining cortical shell, leaving only medullary cavity
12	Despeckle	Remove white speckles in 3D space <40 voxels, apply to image	Removes any holes within the epiphyseal line to make it easier to segment the epiphyseal line from the medullary cavity
13	Morphological Operations	Closing in 2D space, round kernel, 19-pixel radius, apply to image	Closes the ROI over any trabeculae while excluding the epiphyseal line
14	Morphological Operations	Erosion in 2D space, round kernel, 3-pixel radius, apply to image	Brings ROI in 3 pixels to sever any remaining connections to the endocortical surface
15	Bitwise Operations	Region of Interest = COPY Image	Changes the ROI from the entire bone to only the medullary cavity.

Step	CTAnalyser Function	Settings Applied	Description
16	Reload	Reload image	Resets the 2D images to be the original grayscale image within the ROI.
17	Save Bitmaps	Saves image inside ROI as a bitmap	Saves each 2D image of the trabeculae for analysis
18	Save Bitmaps	Save ROI as a monochrome (1 bit) bitmap	Saves each 2D ROI image of the medullary cavity as a 1-bit bitmap

APPENDIX E

IMAGEJ MACRO FOR MEDULLARY CAVITY QUADRANTS

Developed by: Dr. Mary E. Cole

1. Ensures background color is set to black.
2. Image is converted to 8-bit.
3. Auto-thresholds image from pixel value 1 to 255, ensures the background is set to black again.
4. Converts threshold selection to a mask.
5. Runs “Slice Geometry” function from BoneJ²⁰⁸.
6. Saves centroid X value.
7. Draws a vertical line through the centroid.
8. Rotates line counterclockwise 45°, 135°, 225°, then 315° from original to create quadrant borders.
9. Changes foreground color to black.
10. Duplicates original image.
11. Draws quadrant border lines in black.
12. Revert foreground color to white.
13. Duplicates image with borders drawn.
14. Makes a polygon selection with the borders for the anterior quadrant.

15. Clears outside.
16. Saves image as anterior quadrant.
17. Repeats Steps 14-16 for medial, lateral, and posterior quadrants.
18. Repeats Steps 1-17 for each image in the dataset.

APPENDIX F

MATLAB CODE ANALYZING STRESS-STRAIN CURVE

Developed by: Reed Davis and Hope Zimmerman

% Modified by Hope Zimmerman

clc %HZ

close all %HZ

clear all %Clears workspace variables from previous run. (Peace of mind)

Imports

%Opt A: Import from a folder

testfiledir = 'C:\Pythonprogs\RabbitRibs'; %Add File directory here

matfiles = dir(fullfile(testfiledir, '*.csv'));% get list of files

%Opt B: GUI pick folder

%[fname,path] = uigetdir();%or enable a folder search

%matfiles = dir(fullfile(path, '*.csv'));%get list files

nfiles = length(matfiles);%number of files

load('Sample_Length_and_Area')%a table

%splitting the table

sample_name = table2array(SampleLengthandArea(:,1));

sample_area = table2array(SampleLengthandArea(:,2));%m²

sample_length = table2array(SampleLengthandArea(:,3));%mm

```

%Algorithms
%M manually select yield point
%A1 find inflection points and manually pick
%A2 find longest run of negative dSlope
%A3 find max slope and find when slope = .95Max AFTER max

%TO collate data
sample_name_col=[];%see below
peak_stress_col=zeros(nfiles,1);
peak_strain_col=zeros(nfiles,1);
peak_modulus=zeros(nfiles,1);
peak_modulus_stress=zeros(nfiles,1);
peak_modulus_strain=zeros(nfiles,1);
total_energy_col=zeros(nfiles,1);

%make a list of sample names, not numerical so collated here
for i = 1 : nfiles
    sample_name_col=[sample_name_col(:);...
        convertCharsToStrings(matfiles(i).name)];
    %the convertCharsToStrings lets us make an array
end

for i = 1 :nfiles
DataCopy=readmatrix(fullfile(testfiledir, matfiles(i).name)); %read csv to a matrix
    %convert
    Disp=DataCopy(:,1); %Column 1 is displacement (mm)
    Force=DataCopy(:,2); %Column 2 is force (kN)
    Force=Force.*1000; % to N
    Disp=Disp./1000; % to m

```

```

Ostrain=Disp./(sample_length(i)/1000);%m/m
Ostress=Force./sample_area(i);%N/m^2 = Pa
Ostress=Ostress./(10^6); %to MPa

Nancount=sum(sum(isnan(DataCopy))); %Should be 0. Error checking, counts how
many "Not a Numbers" (NaNs) exist in dataset
Dlen=size(DataCopy,1); %returns length of strain column (1) (how many data points
in column, used for weighting below)

[MaxStress,psInd]=max(Ostress);%hz add psInd PeakStrainIndex

%PEAK Collation
peak_stress_col(i)=MaxStress;
peak_strain_col(i)=Ostrain(psInd);

%trimming
Disp=Disp(1:psInd);
Force=Force(1:psInd);
Ostrain=Ostrain(1:psInd);
Ostress=Ostress(1:psInd);

```

Smooth Force Disp

```
time=[1:length(Disp)];
```

```
Dlen=length(time); %returns length of time (how many data points in column, used for  
weighting below)
```

```
weights=ones(Dlen,1); %Assigns weight of 1 to all data points
```

```
weights(1)=10000; %Sets first data point weight to 10K to anchor
```

```
weights(end)=10000; %Sets last data point weight to 10K to anchor
```

```
%Spline below will spline between the first and last point because weighted
```

```
%so low. First and last point are locked. Ensures start and end are true
```

```
%data points
```

```
%Splining variables
```

```
[~,Sdisp]=spaps(time,Disp,40,weights); %Splined strain
```

```
[~,Sforce]=spaps(time,Force,40,weights); %Splined stress
```

```
Sdisp=Sdisp'; % transpose
```

```
Sforce=Sforce';
```

```
%Total Energy
```

```
%Total area under the curve
```

```
TotEnergy=trapz(Sdisp,Sforce); %Integral of FD curve, trapezoid rule (N*m)
```

```
total_energy_col(i)=TotEnergy;
```

```
Sstrain=Sdisp./(sample_length(i)/1000);% m/m
```

```
Sstress=Sforce./sample_area(i);% N/m2 = Pa
```

```
Sstress=Sstress./(106); %to MPa
```

```

% Save Spline
T = table(Disp, Force,...
    Sdisp, Sforce,...
    Ostrain, Ostress,...
    Sstrain,Sstress);%Buid a csv
T.Properties.VariableNames = {'Displacement_m','Force_N',...
    'Splined_Displacement_m','Splined_Force_N',...
    'Strain_m/m','Stress_MPa',...
    'Splined_Stress_MPa', 'Splined_Strain_mm/mm'};
splinefilename =[matfiles(i).name(1:end-4),'_Splines_and_trims.csv'];
splinefolderdir=strcat(testfiledir, '\Splined_Data');
saveto_title=fullfile(splinefolderdir, splinefilename);

writetable(T,saveto_title,'Delimiter',';', 'QuoteStrings',true);

```

Differentiating

```
Modulus=zeros(length(Sstress)-1,1);
for j=1:(length(Sstress)-1)
    Modulus(j)=(Sstress(j+1)-Sstress(j))/(Sstrain(j+1)-Sstrain(j));
end

%find Max Modulus
trim=25;%To avoid the splining weights at ends
[ModM,ModI]=max(Modulus(trim:end-trim));
ModI=ModI+trim;

peak_modulus(i)=Modulus(ModI);
peak_modulus_stress(i)=Sstress(ModI);
peak_modulus_strain(i)=Sstrain(ModI);
```

Display Results

```
%Plots splined force against displacement
figure()
plot(Ostrain,Ostress,'.','Color',[255,0,0]/255, 'MarkerSize',5); %red original data
hold on

plot(Sstrain,Sstress,'.','Color',[0,0,255]/255, 'MarkerSize',5); %blue splined data

%plot manual yield points of interest
po=plot(peak_modulus_strain(i),peak_modulus_stress(i),'ko');
po.MarkerSize = 8;

%labelling
title(strcat('Splined Stress by Strain FINAL',matfiles(i).name))
```